INFORMATION TO USERS

The most advanced technology has been used to photograph and reproduce this manuscript from the microfilm master. UMI films the original text directly from the copy submitted. Thus, some dissertation copies are in typewriter face, while others may be from a computer printer.

In the unlikely event that the author did not send UMI a complete manuscript and there are missing pages, these will be noted. Also, if unauthorized copyrighted material had to be removed, a note will indicate the deletion.

Oversize materials (e.g., maps, drawings, charts) are reproduced by sectioning the original, beginning at the upper left-hand corner and continuing from left to right in equal sections with small overlaps. Each oversize page is available as one exposure on a standard 35 mm slide or as a 17" × 23" black and white photographic print for an additional charge.

Photographs included in the original manuscript have been reproduced xerographically in this copy. 35 mm slides or 6" × 9" black and white photographic prints are available for any photographs or illustrations appearing in this copy for an additional charge. Contact UMI directly to order.

UMI
Accessing the World's Information since 1938

300 North Zeeb Road, Ann Arbor, MI 48106-1346 USA

Order Number 8801762

Photogenerated carrier dynamics in semiconductor quantum wells

Shum, Kai, Ph.D.

City University of New York, 1987

U·M·I
300 N. Zeeb Rd.
Ann Arbor, MI 48106

PLEASE NOTE:

In all cases this material has been filmed in the best possible way from the available copy. Problems encountered with this document have been identified here with a check mark __✓__.

1. Glossy photographs or pages _____
2. Colored illustrations, paper or print _____
3. Photographs with dark background _____
4. Illustrations are poor copy _____
5. Pages with black marks, not original copy __✓__
6. Print shows through as there is text on both sides of page _____
7. Indistinct, broken or small print on several pages __✓__
8. Print exceeds margin requirements _____
9. Tightly bound copy with print lost in spine _____
10. Computer printout pages with indistinct print _____
11. Page(s) _____ lacking when material received, and not available from school or author.
12. Page(s) _____ seem to be missing in numbering only as text follows.
13. Two pages numbered _____. Text follows.
14. Curling and wrinkled pages _____
15. Dissertation contains pages with print at a slant, filmed as received __✓__
16. Other _____

_____

_____

PHOTOGENERATED CARRIER DYNAMICS IN SEMICONDUCTOR QUANTUM WELLS

by

KAI SHUM

A dissertation submitted to the Graduate Faculty in Engineering in partial fulfillment of the requirements for the degree of Doctor of Philosophy, The City University of New York.

1987

This manuscript has been read and accepted for the Graduate Faculty in Engineering in satisfaction of the dissertation requirement for the degree of Doctor of Philosophy.

9-18-87
Date

R. R. Alfano
Chairman of Examining Committee

9-21-87
Date

Se Jeung Oh
Executive Officer

S. Ahmed

P. P. Ho

R. Dorsinville

J. C. Tsang

Supervisory Committee

The City University of New York

Photogenerated Carrier Dynamics in Semiconductor Quantum Wells

Kai Shum

Advisor: Professor R. R. Alfano

ABSTRACT

Subpicosecond laser and streak camera technologies and steady state photoluminescence spectroscopy were used to investigate the ultrafast dynamics of photogenerated carriers and hot-phonons in III-V undoped GaInAs and GaAs quantum well structures fabricated by state-of-art MBE technique as well as in II-VI CdS_xSe_{1-x} spherical quantum wells.

We have demonstrated what experimental data from optical transitions should be used in order to determine the band offsets in the sensitive zone of well thickness ranging from 15 to 80Å. A critical discussion on the creditability of our model is given.

A theoretical study on the electron scattering rate by LO phonon was carried out by treating phonon momentum in the confined z-direction as a ramdon varible. The calculated results show that the emission rate at the onset of phonon emission is 3 times smaller than previously reported and has a weak well width dependence. The experimentally observed variation of carrier temperature with well thickness using photoluminescence indicates that the phonon scattering rate

for carriers confined in quantum wells does not strongly depend on the well width within our experimental accuracy.

Time-resolved photoluminescence from an undoped GaAs multiple symmetric and a single asymmetric quantum well structures at 4K excited by 500fs laser pulse were measured by a streak camera detection system with 2ps time resolution. The hot-phonon effect on energy relaxation of hot carriers is experimentally verified. We have found that hot-phonons are responsible for the ultrafast carrier density decay within the first 30ps after the end of 500fs laser pulse excitation. The diffusivity D of photoexcited carriers in the asymmetric well has been directly determined to be $10^6 cm^2/s$ at 4K, which is about four orders magnitude larger than the thermodynamic value in bulk GaAs.

The recombination lifetimes for the radial and angular quantum number conserved $1S \rightarrow 1S$ and $1P \rightarrow 1P$ transitions in CdS_xSe_{1-x} spherical quantum wells (quasi-0D) were measured by time-resolved and steady-state photoluminescence spectroscopy and compared with theory.

Acknowledgment

It is a great pleasure to acknowledge my deep indebtedness to Dr. Robert R. Alfano, Distinguished Professor of Science and Engineering, for his continued support, encouragement, instruction, and patient guidance during the course of this research.

I am grateful to the faculty of the Electrical Engineering Department for their instruction and help, especially to Professors G. Eichmann, S. Ahmed, P. P. Ho, and R. Dorsinville. I wish to express my sincere thanks to my colleagues at The Institute for Ultrafast Spectroscopy and Lasers particularly Dr. M. Junnarkar, Dr. A. Doukas, Dr. N. Ockman, Dr. S. Gayen, Dr. C. Zhang, Mr. Y. Budansky, Mr. S. Chao, Mr. J. Zheng, and Mrs. M. Gibbs for their help in course of this work. I thank Dr. K. Bajaj of Air Force Wright Aeronautical Laboratories for many helpful discussions. I also thank Professor H. Morkoc and L. Eastman for quantum well samples used in this thesis.

I would like to take this opportunity to express my sincere thanks to my parents and grand parents for their traditional family training. I heartily thank my uncle and aunt who made it possible for me to continue graduate study in the United States. Special thanks goes to my wife, Lina, for her love, encouragement, and understanding.

Finally, I would like to thank Dr. Gerald Witt of Air Force Office of Scientific Research for providing the support to carry out this research.

Table of Contents

List of Tables

List of Figures

Chapter 1

Introduction

In this chapter, the basic properties of photogenerated carriers in semiconductor quantum well structures are discussed. Semiconductor quantum well structures will be introduced first; followed by a description of the quantized electronic states and subbands in these structures. A background on three major dynamic processes of photogenerated carriers in semiconductor quantum well structures which are (1) the loss of average kinetic energy of carrier system to host lattice through electron-phonon interaction, (2) the carrier diffusion due to carrier density gradient, and (3) the electron-hole recombination through both radiative and nonradiative mechanisms is reviewed. The development of generating an ultrashort laser pulse which affects the time-resolution to study the above three dynamic processes is discussed. Finally, the thesis work is outlined.

1.1 Semiconductor Quantum Well Structures

The advent of molecular beam epitaxy (MBE)[1-3] made it possible to grow structures composed of alternate ultrathin layers of two different semiconductors (For example, III-V elements: GaAs/AlGaAs). The interface of two different semiconductors can be atomically abrupt and planar resulting in one-dimensional well-defined electronic potential barriers and wells in wider and narrower band-

gap regions, respectively. Structures consisting thin barrier layers (typically < 40Å) in which the electronic wave coupling between adjacent wells is strong are called a superlattice; while consisting of thick barrier layers (typically > 40Å) in which the coupling can be neglected are called multiple-quantum-well structures. By controlling compositional and doping profiles over distances as well as layer thicknesses, it is allowed to tailer nearly arbitrarily the energy band-gap diagram of a desirable structure. A new generation of devices with unique capabilities, ranging from photomultipliers to optical gate is emerging from this approach.

In Fig.1-1-1a, a transmission electron microscopic (TEM) image of a cross section of a GaAs multiple-quantum-well (MQW) structure is shown. As can be seen the alternate white and black lines correspond two different semiconductor materials which have similar lattice constant and different energy band gaps. A schematic energy diagram of the MQW structure is depicted in Fig.1-1-1b. The E_{gb} and E_{gw} are energy gaps for barrier and well, respectively. The L_z and L_b are the thickness of the well and barrier, respectively. Because of the energy band gap difference, $\Delta E_g = E_{gb} - E_{gw}$, electrons in conduction band and holes in valence band experience potential wells. The electronic states will be strongly modified by the potential wells. Such a modification results in discrete bound states as indicated by narrow lines inside the wells in Fig.1-1-1b. This aspect is reviewed in next section.

The band discontinuities (offsets) at semiconductor hetero-interface give rise the well depths of quantum wells in the conduction and valence bands, ΔE_c and ΔE_v, respectively. The intrinsic asymmetric associated with ΔE_c for electrons in the conduction band and ΔE_v for holes in the valence band has produced

spectacular effects for photonic and electronic devices such as quantum-well lasers, photodetectors, and high-speed logic elements. Consequently, tremendous efforts have been dedicated to the accurate determination of band offsets. However, most of the experimental probes carry their own sources of uncertainties. The electrical measurements are often plagued by residual doping whereas the interband optical transitions may prove to be too weakly dependent upon the band offsets. In spite of many techniques utilized, the magnitudes of ΔE_c and ΔE_v, even for the well-studied GaAs/AlGaAs system remain a controversial subject.[4]

The two-dimensional quantum wells (quantum wires) and three-dimensional quantum wells (quantum dots) have been also fabricated[5] based on the MBE and electron beam lithography techniques. As an alternative to the quantum dots fabricated by the MBE, a collection of tiny semiconductor Cd(S, Se) crystallites embedded in glass filters also possess the quantum confinement effects.[6,7] However, our understanding of these crystallites is primitive.[8]

A typical TEM image of a group of semiconductor crystallites embedded in transparency matrix is shown in Fig.1-1-2a. The size of crystallite can be prepared in range of 70Å to 130Å. The variance of size distribution of crystallites can be reduced to as small as $25Å^2$. The simplest way to describe the motion of conduction electrons and valence holes in each individual crystallite is the model of a particle in an infinite spherical quantum well as shown in Fig.1-1-2b.

1.2 Quantized Electronic States and Subbands

The key difference of electronic states in semiconductor quantum wells from that in bulk semiconductor is the appearance of bound states due to additional confining potential profile experienced by electrons as well as holes. There are many theoretical approaches[9] involving various approximations to predict the eigen energy states and the energy-momentum dispersion relations. In this review section, we will adopt the envelope function approximation approach developed by G. Bastard[9] to describe the electronic states and subbands in quantum well structures. This approach has the merit of often leading to analytical results. Since the quantum well materials we studied in this thesis are GaAs, $Ga_{0.47}In_{0.53}As$, and CdS_xSe_{1-x}, the carrier confinement energies are smaller than both the band gaps. Moreover, for the study of photogenerated carrier dynamics, we always deal with the carriers in vicinity of the center of the Brillouin zone, i.e. $\vec{K}=0$. The following further simplifications will be made: (i) to neglect the coupling between each allowed energy bands, and (ii) to neglect the nonparabolicity of energy bands. Using these approximations the motion of electrons or holes in the well direction (growth direction) can be separated from the motion in the lateral plane of well. Therefore, a complicated problem of obtaining the eigen energy states and dispersion relations in quantum well is reduce to a simple one-dimensional quantum well for electrons in conduction band and heavy-holes and light-holes in valence band with their corresponding effective masses.

We consider the case of one quantum well for electrons in conduction band or for holes in valence band as shown in Fig.1-2-1a. The growth direction will be taken as the z axis. The Hamiltonian of carrier (either electron or heavy-hole or light-hole) is given by:

$$\hat{H} = -\frac{\hbar^2}{2m_j(z)}\frac{\partial^2}{\partial z^2} + \hat{V}(z) \quad , \tag{1-2-1}$$

where $j = e, hh, lh$ represents electron, heavy-hole(hh), and light-hole(lh), respectively; $\hat{V}(z)$ is the potential operator is z-direction; and $m_j(z)$ is the effective mass which depends on the position z. In order to obtain eigen energies we have to solve a Schrodiger equation, which is of form

$$\hat{H}\ \phi_{jn} = E_{jn}\ \phi_{jn} \quad . \tag{1-2-2}$$

where ϕ_{jn} is the envelop wave function in z-direction describing the n th bound state. This wave function can be written as

$$\phi_{jn} = \begin{cases} C_1 e^{-ik_{wn}z} + C_2 e^{ik_{wn}z}, & 0 \leqslant z \leqslant L_z \\ C_3 e^{\kappa_{bn}z}, & z < 0 \\ C_3 e^{-\kappa_{bn}(z-L_z)}, & z > L_z \end{cases} \tag{1-2-3}$$

where

$$k_{wn} = \sqrt{\frac{2m_{wj}E_n}{\hbar^2}} \quad ; \tag{1-2-4}$$

and

$$\kappa_{bn} = \sqrt{\frac{2m_{bj}(V_j - E_n)}{\hbar^2}} \quad , \quad [V_e = \Delta E_c, \quad V_{hh,lh} = \Delta E_v] \quad , \tag{1-2-5}$$

are the two parameters that related to the n th eigen-value of eigen-equation (1-2-2), and C_1, C_2, and C_3 are the constants to be determined using boundary and normalization conditions. In an "infinite potential well" approximation, the carrier wave function can be written in a simple form which is

$$\phi_{jn} = \sin\frac{n\pi}{L_z}z \qquad n = 1,2,3. \tag{1-2-6}$$

The allowed energy levels in a finite potential well are obtained by imposing certain boundary conditions at interfaces ($z=0$, and $z=L_z$). The mismatch of carrier effective mass in well and barrier material is responsible for appearance of various types of boundary conditions. In general, using different set of boundary conditions will result in different eigen energy levels.

Using the conventional boundary conditions which are

$$\phi(z=0^-) = \phi(z=0^+); \qquad \phi(z=L_z^-) = \phi(z=L_z^+) \tag{1-2-7}$$

and

$$\frac{\partial\phi(z=0^-)}{\partial z} = \frac{\partial\phi(z=0^+)}{\partial z}; \qquad \frac{\partial\phi(z=L_z^-)}{\partial z} = \frac{\partial\phi(z=L_z^+)}{\partial z}\ , \tag{1-2-8}$$

as well as so-called χ-normality boundary condition[10] that $\frac{\phi(z)}{\sqrt{m_j(z)}}$ and $\frac{\partial\phi(z)}{\partial z}\ \frac{1}{\sqrt{m_j(z)}}$ being continuous at interfaces, we obtain the following equation for n th eigen energy level E_n:

$$\tan k_{wn} L_z = \frac{2k_{bn}\,k_{wn}}{k_{wn}^2 - k_{bn}^2}\ . \tag{1-2-9}$$

When Bastard's boundary conditions[9] that $\phi(z)$ and $\frac{1}{m_j(z)}\ \frac{\partial\phi(z)}{\partial z}$ are both continuous at the interfaces are used, the equations that determine the n th eigen energy E_n are given by:

$$\tan\left(\frac{k_{wn} L_z}{2}\right) = \frac{\kappa_{bn} m_{wj}}{k_{wn} m_{bj}} \quad ; \tag{1-2-10}$$

and

$$cotan\left(\frac{k_{wn} L_z}{2}\right) = -\frac{\kappa_{bn} m_{wj}}{k_{wj} m_{bj}} \quad . \tag{1-2-11}$$

For the infinite potential well the eigen-value E_n is given by:

$$E_n = \frac{\hbar^2}{2m_j}\left(\frac{n\pi}{L_z}\right)^2 \quad , n = 1, 2, 3. \tag{1-2-12}$$

Although the potential well is finite in reality, the above equation can be used to estimate the eigen energies of low lying bound states. For example, suppose carriers are confined in a 100Å-GaAs infinite potential well the eigen energies for the lowest two states are given by:

$E_1 = 56meV$, $E_2 = 225meV$, for *electrons* ;

$E_1 = 9meV$, $E_2 = 36meV$, for *heavy −holes* ;

$E_1 = 42meV$, $E_2 = 168meV$, for *light −holes*

where effective masses $m_e = 0.067m_0$, $m_{hh} = 0.403m_0$ and $m_{lh} = 0.087m_0$ are used.

Based on the simplification we made above, the lateral in-plane (x-y plane) motion of carriers is decoupled from the motion of carrier in z-direction. Therefore, the in-plane dispersion relation which relates the n th bound state are given by:

$$\varepsilon_j(\vec{k}) = E_n + \frac{\hbar^2 \vec{k}^2}{2m_{wj}} \quad , \tag{1-2-12}$$

where ϵ_j is the carrier energy respect to the conduction band edge of well material for electron or to the valence band edge for holes. The fact that the ϵ_j quadratically varies with in-plane momentum $\vec{k}$, gives rise the n th subband of electronic states which corresponds n th bound state in z-direction. A schematic diagram of the first and second subbands for carriers in quantum well is shown in Fig.1-2-1b.

The well-known staircase-like density of states follows from the bidimensional quadratic dispersion relation given in Eq.(1-2-12). Let $D(\epsilon)$ denote this density of states. then one obtains:

$$D(\epsilon) = \sum_n D_n(\epsilon) ; \quad D_n(\epsilon) = \frac{m_{wj} A}{\pi h^2} S(\epsilon - E_n) . \tag{1-2-13}$$

In above equation, n runs over the bound states of the quantum well, A is the sample area, and $S(x)$ is a step function ($S(x) = 1$ if $x > 0$, $S(x) = 0$ if $x < 0$). The density of states for the first two subbands is schematically depicted in Fig.1-2-1c for either electron or heavy-hole or light-hole.

In case of the quantum dot described in section 1.1, the electronic motion in such a system no longer follow a well-defined energy-momentum relation because the Hamiltonian of carrier does not commute with the momentum operator due to potential discontinuity at the crystallite surface. The envelope wave functions in spherical coordinates $[r, \theta, \phi]$ and eigen energies of conduction electrons and valence holes localized in an infinite-spherical-well within the effective mass approximation are given by:[8]

$$|nLm> = C_{nL} \; j_L(\chi_{nL} r) Y_{Lm}(\theta,\phi) , \qquad (1\text{-}2\text{-}14)$$

and

$$E_n = \frac{\hbar^2 \chi_n^2}{2m_{e,h} a^2} , \qquad (1\text{-}2\text{-}15)$$

respectively, where the subscripts n, L, and m are radial, angular and magnetic quantum numbers, respectively; the j and Y are the spherical Bessel and spherical Harmonic functions, respectively; a is the radius of crystallite; and $m_{e,h}$ is the effective mass of electron or the isotropic hole mass.[8] The value of χ_n for the lowest two states of either conduction electron or valence hole $1S$ and $1P$ are π and 4.49, respectively. S stands for $L=0$ and P for $L=1$. The allowed transitions which conserve angular and radial quantum numbers are $1S \rightarrow 1S$, $1P \rightarrow 1P$, and higher transitions. As an example, the eigen energies of confined carriers in a 100Å-$CdS_{0.27}Se_{0.53}$ infinite-spherical-well are given by:

$$E_1 = 187meV , \qquad E_2 = 382meV , \qquad \text{for } electrons ;$$

$$E_1 = 39meV , \qquad E_2 = 80meV , \qquad \text{for } holes ,$$

where $m_e = 0.15m_0$ and $m_h = 0.60m_0$ are used. The density of states of carriers in quantum dots is expressed as

$$D(\epsilon) = \sum_{n,L} \delta(\epsilon - E_{nL}) . \qquad (1\text{-}2\text{-}16)$$

A schematic recollection of the properties of quantum dot bound states is shown in Fig.1-2-2.

1.3 Background on Carrier Dynamics in Quantum Wells

A key factor that affects photogenerated carrier dynamics in a quantum well structures is the electron-phonon scattering rate in quasi-two-dimensional electron system. Previous theoretical studies using various approximations[11-13] predict a larger electron-phonon scattering rate in quantum well structures than in bulk counterpart. However, the experimental results by many groups have shown either similar[14,15] or much slower[16,17] hot-electron cooling rate. The explanation for this contradiction is not yet clear. This thesis shows some light in the subject.

Historically, the first comparison[14] of the hot-electron cooling rates in undoped multiple quantum well (MQW) structures and in the bulk GaAs was achieved using time-resolved optical absorption and gain. The cooling rates were approximately same for the bulk and the MQW at a carrier density of 2.5×10^{17} cm^{-3}. This is expected from a simple theory[18] where the lattice is treated as a heat bath for the nonequilibrium carrers. The quasi-steady-state experiments have been carried out from two groups[15,16] to investigate the interaction of electrons and holes with phonons in modulation-doped MQW structures. These experiments have generated conflicting results regarding the presence[16] or the absence[15] of nonequilibrium phonon (hot-phonons). The measurements of time-resolved photoluminescence (PL) from modulation doped semiconductor MQW with more than 20ps time resolution were reported by Ryan *et al.*[17] who found that the cooling of hot carriers was anomalously slow by 60 times after 40ps.

After reviewing the literature, three points which motivate the major part of this thesis are as follows. First, to assess the importance of hot-phonon effect

on the energy relaxation of hot carriers one has been using theoretical approaches to match the experimental carrier temperature cooling curve or the logarithm of power loss as function of the inverse carrier temperature. There have been no reports on the direct evidence for the existence of the hot-phonons in quantum well structures and on how the hot-phonons affect the energy relaxation at various time periods and the carrier lifetime. Second, Because of large number of the doped-in carrier density in modulation-doped MQW structures, which is comparable to the photoexcited carrier density one can not easily obtain information on photo-generated carrier lifetime although the energy loss rates of the photoinjected majority carriers can be studied. In these modulation-doped MQW structures the carrier lifetime is essentially close to the lifetime in bulk about 1ns.[17] Therefore, it is necessary to study photoinjected carrier dynamics in undoped quantum well structures in order to obtain information both on the energy loss rates and on the carrier lifetime. Third, the subject of photoexcited electron-hole plasma expansion at high density in various quantum well structures has not been experimentally investigated on a picosecond time scale. Only one indirect measurement of the expansion of electron-hole plasma in GaAs MQW structures at low carrier density was reported[19] where they found the drift velocity of the plasma was comparable to its Fermi-velocity, and therefore the transport of the photoexcited carrier in GaAs quantum wells was thermodiffusive.

1.4 Short Laser Pulse Development

Parallel to the development of the epitaxial growth technique, dramatic advances have taken place in the generation and application of ultrashort laser

pulses[20] and streak camera technology. Ultrafast dynamic processes in semiconductor structures can be probed[21] to the extent that depends on the time resolution available. The increase in time resolution can make a difference between qualitative and quantitative observations and is important for better understanding of the fundamental interactions of confined electrons and holes with phonons in quantum well structures. This understanding is crucial for the operation of ultrahigh speed devices based on the principles of ultrafast carrier dynamics in semiconductor quantum well structures.

A major breakthrough in clocking fast events in time domain occurred in 1966 with the discovery of mode-locked glass lasers which produce light pulses of several picoseconds in duration. The advent of high power picosecond laser pulses in turn revolutionized the field of nonlinear laser spectroscopy which in turn helped the generation of even shorter laser pulses. Methods of mode-locking developed rapidly, and by 1972 a continuously mode-locked dye laser was producing pulses on the order of a picosecond. The dye lasers were improved further leading to the generation of pulses shorter than one picosecond in 1974. The development of the colliding-pulse passive mode-locking technique in 1981 pushed the limit of attainable pulse width even shorter to less than 100 femtoseconds. Novel shaping and pulse compression techniques have led to the shortest reported optical pulse width of 8-fs most recently in 1985. A history of the progress achieved in the capability of measuring faster events with increasing temporal resolution is presented in Fig.1-4-1. Streak camera technology allows luminescence measures with 2ps time resolution.

1.5 Thesis Thrust

In chapter 2, we demonstrated what experimental data from optical transition should be used and how it is sensitive to the band offsets. The band offsets of AlInAs/GaInAs and GaAs/AlGaAs systems were determined using the optical method, namely, by comparing the measured energy separations between heavy-hole and light-hole subbands in narrow quantum wells (well thickness ranging from 15Å to 80Å) to the theoretically calculated values taking into account the various boundary conditions, nonparabolicity, heavy- and light-hole coupling, and exciton binding energy.

In chapter 3, An investigation on the carrier confinement effects and the reduced dimensionality effects on the electron-phonon scattering rate is carried out both theoretically and experimentally.

In chapter 4, we study the initial dynamics of photogenerated carriers in 55Å-MQW structure from 0 to 50ps using a subpicosecond laser source and a 2ps time resolution streak camera. This study was used to assess the importance of hot-phonon effects on both the energy relaxation of hot carriers and the carrier lifetime.

In chapter 5, the dynamic lateral carrier diffusion process in a 50Å- asymmetric quantum well in picosecond time scale at high carrier density is investigated experimentally and theoretically.

In chapter 6, a study on the electron-hole recombination dynamics in quasi-zero-dimensional electron systems in Cd(S, Se) microcrystallites as functions of

diameter of crystallite, temperature, and excitation power density is presented.

The time-resolved experimental method used in this thesis work is described as follows. The high density of electron-hole pairs in quantum well structures are generated by the photoexcitation by a 500fs laser pulse. These photogenerated carriers thermalize via carrier-carrier interaction to reach a quasi-equilibrium state in less than 1ps. Simultaneously three other processes take place. The first one is the loss of energy of the electron-hole system through the electron-phonon interaction. The second process is the carrier diffusion process due to the gradient of carrier density between photoexcited and non-excited area. The third process is recombination of electron-hole pair through both nonradiative and radiative mechanism. The latter gives rise the luminescence. This thesis make use of the luminescence signal both in the spectral and time domain to monitor the photogenerated carrier dynamics as well as nonequilibrium phonon dynamics.

The steady-state photoluminescence method was used to characterize the quality of quantum well structures and extract information about the electronic states in quantum well structures.

Reference

(1) A. Y. Cho, and J. A. Arthur, *Progress in Solid-State Chemistry*, J. O. McCaldin and G. Somorjai, Eds. (Pergamon, New York, 1975), vol.10, p.157; L. Esaki and R. Tus, IBM J. Res. Dev. 14, 61(1971).

(2) A. C. Gossard, IEEE J. Quantum Electronics QE-22, 1649(1986).

(3) L. A. Kolodziejski, R. L. Gunshor, N. Otsuka, S. Datta, W. M. Becher, and A. V. Nurmikko, IEEE J. of Quantum Electronics, QE-22, 1666(1986).

(4) G. Duggan, J. Vac. Sci. Technol. B3(4), 1224(1985).

(5) K. Kash, A. Scherer, J. M. Worlock, H. G. Craighead, and M. C. Tamargo, Appl. Phys. Lett. 49, 1043(1986).

(6) J. Warnock, and D. D. Awschalom, Appl. Phys. Lett. 48, 425(1986).

(7) N. F. Borrelli, D. W. Hall, H. J. Holland, and D. W. Smith, J. Appl. Appl., 61, 5400(1987).

(8) L. Brus, IEEE J. of Quantum Electronics, QE-22, 1909(1986).

(9) G. Bastard and J. A. Brum, IEEE J. of Quantum Electronic, QE-22, 1625(1986).

(10) H. Kromer and Q. G. Zhu, J. Vac. Sci. Technol. 21, 551(1982).

(11) K. Hess, Appl. Phys. Lett., 35, 484(1979).

(12) B. K. Ridley, J. Phys. C, 15, 5899(1982).

(13) J. P. Leburton, J. Appl. Phys., 56, 2850(1984).

(14) C. V. Shank, R. L. Fork, R. Yen, J. Shah, B. I Greene, A. C. Gossard and C. Weisbuch, Solid State Commun. 47, 981(1983).

(15) C. H. Yang, Jean M. Carlson-Swindle, A. Lyon, and J. M. Worlock, Phys. Rev. Lett., 55, 2359(1985).

(16) J. Shah, A. Pinczuk, A. C. Gossard, and W. Wiegmaann, Phys. Rev. Lett., 54, 2045(1985).

(17) J. F. Ryan, R. A. Taylor, A. J. Turberfield, A. Maciel, J. M. Worlock A. C. Gossard, and W. Wiegmann, Phys. Rev. Lett. 53, 1841(1984).

(18) E. M. Conwell, *High Field Transport in Semiconductors*, (Academic Press, New York, 1967).

(19) K. T. Tsen, and H. Morkoc, Phys. Rev. B, 34, 6018(1986).

(20) C. V. Shank, Science, vol.129, 1027(1983).

(21) See for example, *Semiconductors Probed by Ultrafast Laser Spectroscopy* edited by R. R. Alfano, Academic Press, New York, 1984.

(22) M. J. Kelly, R. A. Davies, P. A. Long, N. R. Couch, P. H. Beton and T. M. Kerr, *Superlattice and Microstructures*, Vol. 2, No. 4, 313(1986).

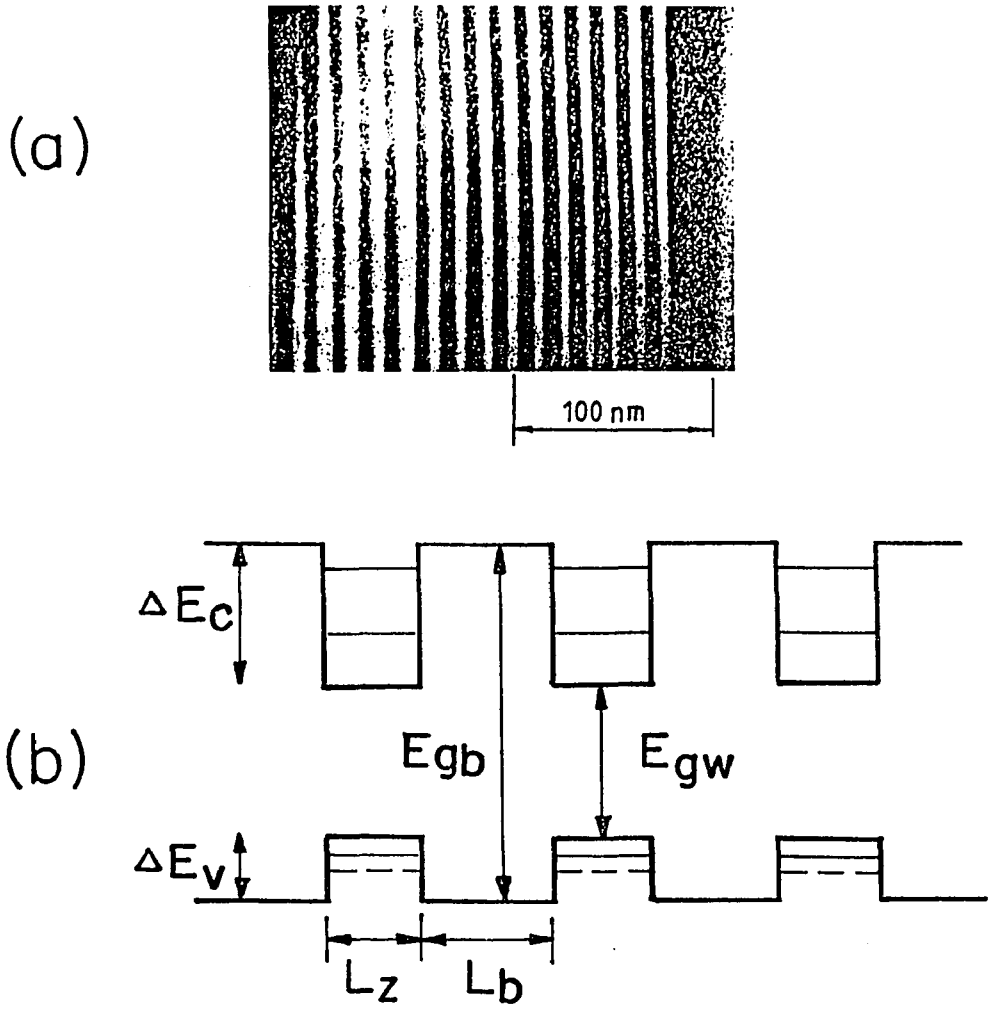

Fig.1-1-1 (a) TEM image of GaAs/AlGaAs multiple quantum well structure with $L_z = 65\mathring{A}$, and $L_b = 45\mathring{A}$ (from Ref.22). (b) A shematic energy diagram of MQW structure. ΔE is the energy separation of hh and lh subbands at $\vec{k} = 0$.

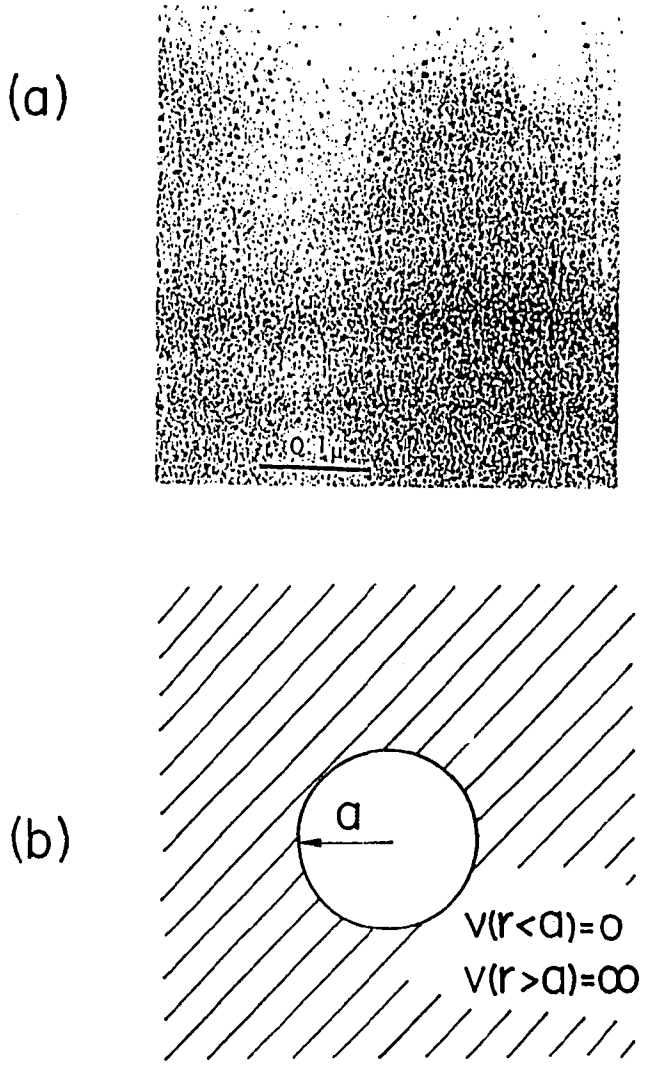

Fig.1-1-2 (a) A TEM micograph of the CdSe microcrystallites in insulating glass matrix (Ref.7). (b) A schematic diagram of a infinite spherical quantum well with radius a.

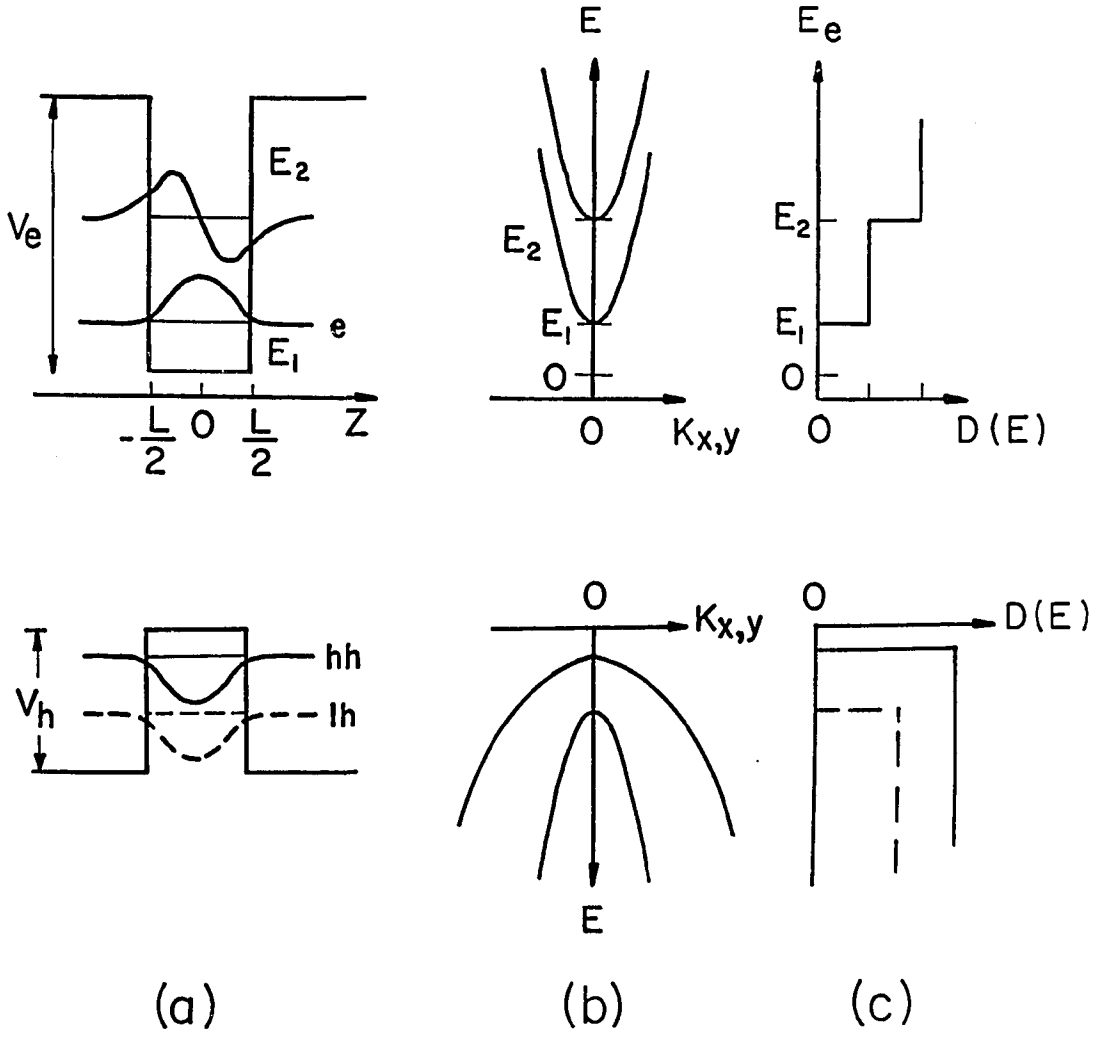

Fig.1-2-1 A recollection of the main properties of the quantum well confined states. (a) Well profiles and envelope wave functions. (b) In plane (x-y plane) dispersion relationships. (c) Density of states.

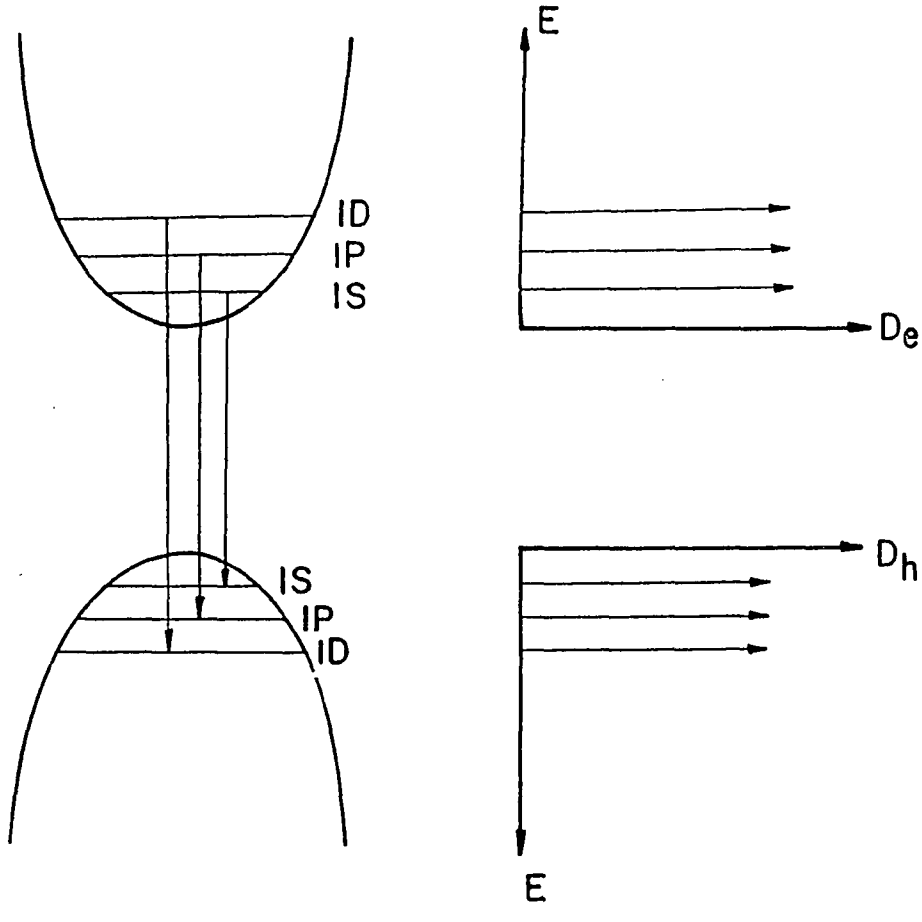

Fig.1-2-2 (a) Confined states of electron and hole in conduction and valence bands, respectively, in a semiconductor microcrystallites. (b) Density of states of three-dimensionally confined electron system.

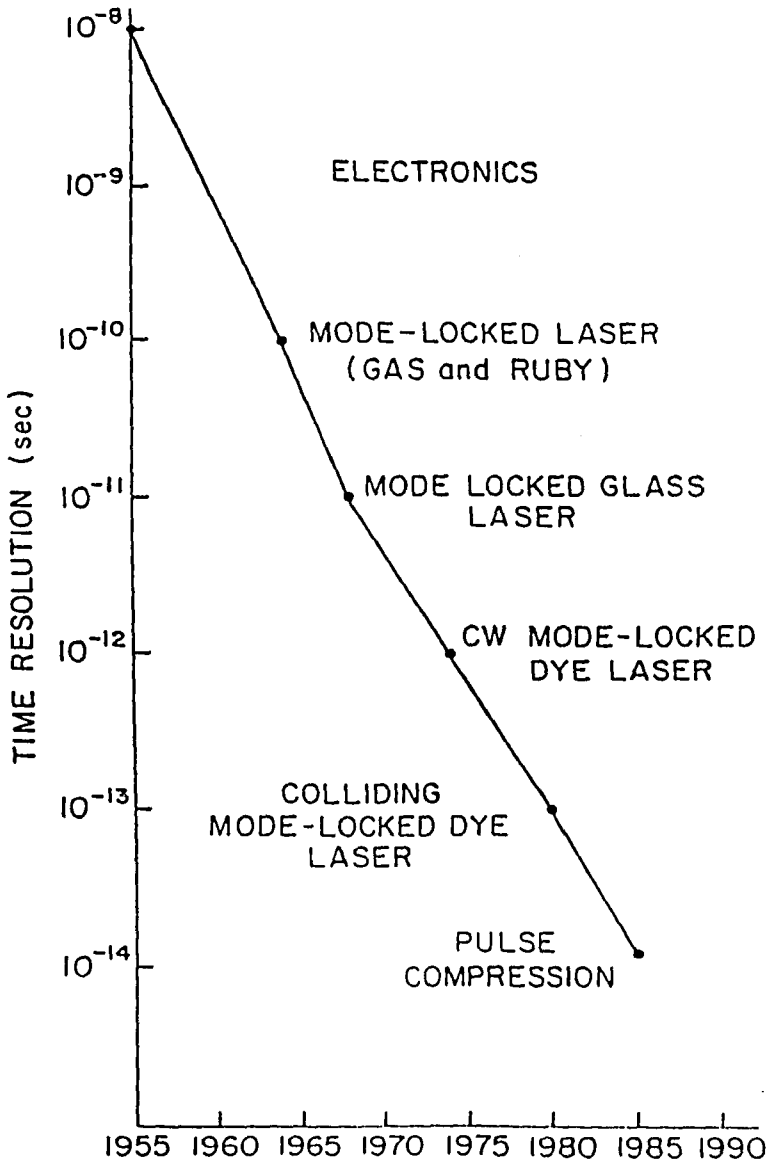

Fig.1-4-1 The time resolution plotted as function of year with the development of Laser.

Chapter 2

Determination of band discontinuities via optical transitions in ultrathin quantum wells

The energy separation ($\Delta E = E_{lh\,1} - E_{hh\,1}$) between the light-hole and the heavy-hole subbands (see Fig.1-1-1b) as a function of the well width for ultrathin quantum well structures is calculated using a single-band particle-in-a-box model. It is found that the most sensitive range for well width (L_z) to determine accurately the valence-band discontinuity (ΔE_v) is between 15Å and 80Å whereas insensitive for $L_z > 80$Å using the experimental data of ΔE from optical transitions in quantum wells. Furthermore, the theoretical calculated quantity of ΔE is also sensitive to the boundary conditions imposed at the interfaces. A controversial issue for the determination of the ΔE_v can then be resolved by measuring the ΔE's in sensitive zone of well width range: 15Å to 80Å. This chapter is devoted to the determination of the valence conduction band offsets of both $Ga_{0.47}In_{0.53}As/Al_{0.48}In_{0.52}As$ and GaAs/AlGaAs systems using our own optical data as well as the data from the other workers.

2.1 Background

A fundamental and long-standing problem in the study of the

semiconductor microstructures is the determination of the band-edge discontinuities (ΔE_c and ΔE_v) of heterojunctions.[1-6] It is crucial to solve this problem for device design and other applications. The intrinsic asymmetry associated with ΔE_c and ΔE_v for electrons in the conduction band and holes in the valence band respectively, has produced spectacular effects for photonic and electronic devices such as quantum well lasers, photodetectors and high speed logic elements. Four methods commonly employed to measure ΔE_v as well as ΔE_c are the photoemission spectroscopy [1], capacitance-voltage (C-V) technique,[2] optical transition measurements [3] and the charge-transfer method[7]. The first method is direct ; however, its accuracy is limited and can not be improved thus far beyond a value of about 0.15 eV. This is not sufficient for the most practical applications and critical testing of theories. The second method is not a direct method since it is based on the average properties of the transport of carriers. It is difficult to obtain accurate values of ΔE_v or ΔE_c from the C-V technique because of the numerical uncertainties of the quantities used in determination procedure such as the Fermi-energy-levels and band bendings. The third method is the one that the initial determination of ΔE_v by Dingle and his coworkers[3] was based on. Although, this optical method provides a convenient way to obtain the values of ΔE_v and ΔE_c, there have been excessive recent claims[4,5] that the Dingle's 15-85 rule for the band offset contribution for ΔE_v and ΔE_c found for GaAs/AlGaAs system is in error. Now, it is currently believed that 30-70 is more appropriate value for the offsets of GaAs/AlGaAs structure. In addition, the charge-transfer method[7] was utilized to investigate the orientational independence of band offset at GaAs/(Al,Ga)As hetero-interfaces. In spite of many measurement techniques utilized, the magnitudes of ΔE_c and ΔE_v even for well-studied GaAs/AlGaAs system remain a controversial subject.[6]

2.2 Determination of Band Offsets of AlInAs/GaInAs

2.2.1 Experimental Method

The sample were grown using a Varian 360 molecular-beam epitaxy (MBE) machine.[8] The structures were grown on a thermally cleaned InP substrate consisting of a 2500-Å-thick (Al, In)As layer followed by the (Ga, In)AS single-quantum-well of widths 14.5 and 19.3Å, respectively, and a 100-Å cap layer of (Al, In)As. Each sample was attached to an aluminum plate by "super" glue and contained inside a helium optical cryostat. The sample was excited by a 488-nm argon-ion laser from 10 to 160mW. The excitation area was about 200*um* in diameter. The photoluminescence was collected by a double half-meter Spex spectrometer, detected by Hamamatsu R632 S-1 or a S-20 photomultipliers, and analyzed by a lock-in amplifier and a x-y recorder. The temperature of sample was measured by a silicon diode connected to the cold finger on which the sample-aluminum plate combination was placed. The steady-state photoluminescence setup described above is shown in Fig.2-2-1.

2.2.2 Experimental Results

Various photoluminescence spectra were obtained as a function of lattice temperature T_c from 4 to 90K for two single-quantum-wells (SQW's) of well thickness L_z = 14.5 and 19.3 Å. A set of typical spectra for L_z = 14.5Å are shown in Fig.2-2-2. The peak are denoted by P_1, P_2, P_3, and P_4. The higher-energy set P_1 and P_2 are identified as arising from the electron-hole

recombinations in the barrier (Al, In)As. The lower-energy set P_3 and P_4 are identified as luminescence from the well (Ga, In)As, which are shifted above the bulk band gap $E_{gw} = 0.81eV$, due to confinement of carriers in the quantum well.

In order to determine precisely the band gap of (Al, In)As, which is crucial for the determination of band offset, the origin of the emission peaks P_1 and P_2 must be discussed. From spectra displayed in Fig.2-2-2, it is quite clear that P_1 is stronger than P_2 at lower temperatures and disappears when T_L is above 80K. This temperature corresponds to thermal energy $k_B T_L = 7meV$. The high energy tail of P_1 displayed in Fig.2-2-2a is fitted to $E^2 \exp(-E / k_B T_c)$ yielding a carrier temperature $T_c = 90K$ ($k_B T_c = 8meV$). T_c is higher than T_L due to the heating from photogenerated energetic carriers. The three dimensional exciton's binding energy in (Al, In)As is about 9meV using the parameters $m_e = 0.118m_0$, $m_{hh} = 0.677m_0$, $\kappa(AlAs) = 10.1$, and $\kappa(InAs) = 14.6$. The disappearance of P_1 is caused by the lattice vibrational energy ionizing the exciton in the barriers. Thus, P_1 emission most likely arises from the annihilation of acceptor-bound excitons. The P_2 emission is broader than the P_1 and is weak at $T_L = 90K$. This peak probably arises from the transitions of the electrons in conduction band edge to the shallow acceptor states. Furthermore, the intensity dependence of luminescence on pump intensity of higher-energy set (P_1 and P_2) is plotted in Fig.2-2-3. The luminescence intensity dependence varies as $I_e^{1.2}$. This confirms our speculation that the high-energy set is related to either impurity or exciton emission.[10] From the above identification of P_1 and P_2, the band gap of barrier (Al, In)As is determined to be $E_{gb} = E_{P_1} + E_B = 1.66+0.009 = 1.67eV$ at $T_L = 4K$, where

E_{P_1} is the peak energy of P_1 and E_B is the binding energy of acceptor-bound exciton.

The luminescence spectra of P_3 and P_4 emission for L_z = 14.5 and 19.3Å are shown in Fig.2-2-4. These arise from transitions in quantum well region for both well widths. The peaks P_3 and P_4 are separated by energy difference ΔE = 47 and 75 meV for L_z = 14.5 and 19.3Å, respectively. The following argument is presented to support the assignment of the two peaks P_3 and P_4 arising from the radiative transitions from n=1 electron states confined in the conduction band well to n=1 hh and n=1 lh states confined in the valence band well. The excitation-power dependence of luminescence intensity of P_3 and P_4 emission from $L_z = 14.5\mathring{A}$ quantum well is displayed in Fig.2-2-6. The ratio of intensity of peak P_3 and P_4 is defined by $R_P = I_3 / I_4$, where I_3 and I_4 are the peak intensity for I_3 and I_4, respectively. The electron temperature T_c from each spectrum is determined by fitting the high-energy tail of P_3 to $E^2 \exp(-E / k_B T_c)$. The most salient feature of spectra shown in Fig.2-2-5 is that the ratio R_P increase as electron temperature T_c increases. The R_P versus $k_B T_c$ is plotted in Fig.2-2-6. The cross dots are the peak intensity ratios measured from Fig.2-2-5. The solid curve is fitted to $R_P = C \exp(-\Delta E / k_B T_c)$, where ΔE is the energy separation depicted in the inset of Fig.2-2-6. A value of C = 5.2 takes care of the overlap of transitions from the n=1 electron subband to n=1 hh and lh subband tails. The value of C, in general, depends on the well width L_z, hh and lh interband scattering and other factors. The value of ΔE extracted from this fit is 47meV. Thus, the energy separation ΔE determined by this method is the same as the energy separation between hh and lh subbands in

the quantum well of $L_z = 14.5\mathring{A}$ measured from the photoluminescence spectra. The population of holes in two subbands change with the electron temperature T_c as schematically shown in the inset of Fig.2-4-6. The reason why the electron temperature increases with the increase of excitation power density is probably due to slow energy relaxation at higher carrier density. To further understand this point the more dynamic studies is needed. This argument supports the model involving transitions from n=1 electron subband to two n=1 hole subbands.

In the following, the energy separation ΔE between hh and lh subbands as a function of well width L_z are calculated to support the above data for the two thin wells as long as well depth ΔE_v in the VB is set to be 120meV. The following assumptions are used in the model: (1) the quantum well is simulated by an finite square well with width L_z ; (2) the well depth ΔE_v is used as an adjustable parameter to be determined by fitting the observed energy separation ΔE between hh and lh subbands at different well width L_z ; (3) the effective kinetic energy operator is obtained from three-dimensional effective-mass approximation, i.e., to take hh and lh effective mass (m_{hh} , m_{lh}) from the band edge of (Al,In)As and (Ga,In)As compounds. This is a reasonable approximation because the quantum well for localizing holes in the valence band is shallow. Therefore, the energy dependence on the effective mass of holes is negligible. However, for an electron in the conduction band one must consider the energy dependence on the effective mass, and (4) the boundary conditions are that the wave functions and their spatial derivatives are continuous at the boundaries. This is not Bastard model but Dingle's initial approach. Using above assumptions and the Eqs.(1-2-4), (1-2-5), and (1-2-9) the eigen-energy value E_n in the valence band well for either heavy-hole

or light-hole is determined for a finite well depth by following equation:

$$\tan p\,\sigma_n = \frac{2\sigma_n (m_w / m_b)^{1/2}(1 - \sigma_n^2)^{1/2}}{[(m_w / m_b + 1)\sigma_n^2 - 1]} , \qquad (2\text{-}2\text{-}1)$$

where $\sigma_n^2 = E_n / \Delta E_v$ and $p = L_z (2\Delta E_v m_w)^{1/2} / \hbar$ are two dimensionless variables; m_w and m_b are the effective mass in well and barrier, respectively, and n is the number of the localized states in the well. The value n is controlled by value of p. For L_z =14.5 and 19.3 Å , only one state (n=1) exists in both the CB and VB wells. The values of masses[9] used in this calculation are m_{whh} =0.06094m_0, m_{wlh} =0.0491m_0, m_{bhh} =0.6768m_0 , and m_{blh} =0.0860m_0.

It should be argued that whether or not an effective mass approach based on the band model is still valid for an ultrathin quantum well structure. We may take note of the fact that the conductivities and other electrical properties of the most semiconductors are virtually unchanged in melting[11], suggesting that a band structure is preserved even though there is no longer any long-range order. This is not surprising if we recall that in band model the influence of everything beyond one or two atomic spacings is lumped into a self-consistent field. Furthermore, the wave-function for valence-electrons piles up electronic charge on the cores of the positive ions, thereby valence-electrons are more localized on the nuclei than conduction-electrons. Therefore, the influence on the effective mass of holes due to the reduced dimensionality can be expected to be small.

Various value of parameter ΔE_v have been used in Eq.(2-2-1) to calculate ΔE versus L_z. The calculated results ΔE versus L_z for parameters ΔE_v =100, 120, 140meV are plotted in Fig.(2-2-7). The inset shows the schematic energy-band diagram of a SQW. The dots in Fig.(2-2-7) locate the position of the measured ΔE

for the two wells. The best fit to observed energy separations between hh and lh of 47 and 57meV at well width L_z =14.5 and 19.3 Å is for the parameter ΔE_v =120meV. The fit of the theoretical calculation to experimental data for the well widths of L_z = 14.5 and 19.3Å demonstrates that well depth in the VB is ΔE_v =120meV. The corresponding well depth for the CB is ΔE_c =740meV which is 0.86 ΔE_g . The results of this photoluminescence method agree well with Dingle's relationship ΔE_c =0.85 ΔE_g for (Al,Ga)As/GaAs system obtained by absorption. However, it deviates from the result of 0.73ΔE_g at room temperature obtained by Morgan *et al.* [12] for (Al,In)As/(Ga,In)As who used the current-voltagenmethod. The methods use to determine the well depths may account for this discrepancy. The current-voltage method may have systematic errors due to the background-carrier profile, concentration density of states, and the thermal energy of the free carriers.[13] The photoluminescence method requires the knowledge of hh and lh masses and interaction of carriers among the hh and lh in subbands. For an ultrathin quantum well, the energy separation ΔE is large enough to be observed in photoluminescence spectra and the coupling between hh and lh could be neglected. Our results agree well with Harrison's linear-combination of atomic orbitals (LCAO) approach [14] and photoemission studies of Katnani and Margaritondo [1] within their limited accuracy (± 100meV). By using interpolation method, the absolute position of the valence-band maximum can be obtained from the table given in Ref.14. This yields a value of ΔE_v = 22 meV. The large uncertainty in theoretical approach allows the agreement with our valut of ΔE_v =120meV.

From the result of theoretical calculation shown in Fig.(2-2-7), three salient features appear. First, the value of ΔE is extremely sensitive to the energy discon-

tinuity ΔE_v for an ultrathin SQW of thickness L_z =14.5 and 19.3 Å . This enables us to determine ΔE_v as well as ΔE_c very accurately (± 3meV). Second, for thick wells of L_z >80 Å , the valute of ΔE is insensitive to the choice of ΔE_v . Therefore, it is difficult in practice to determine ΔE_v for thick well. A recent paper [15] reported the value of ΔE_v =290meV for (Ga,In)As/(Al,In)As system using the absorption spectra of a quantum well with L_z varying from 85 to 165 Å . The energy measures for the optical transitions for L_z =110Å well given in Ref.15 can also be fitted well to the absorption transition using the value of ΔE_v =120meV determined by us. The thickness of quantum wells studied by Weiner *et al.* [13] is in an insensitive range for determination of ΔE_v by fitting the measured optical transition using the [see Fig.(2-2-7)]. This will result in an inaccurate determination of ΔE_v . Furthermore, they measured ΔE=29meV for n=1 hh and lh subbands of L_z =110Å well which exactly agrees with our results shown in Fig.(2-2-7). This adds further support to our determination using a PL method. Third, there is a maximum energy separation ΔE_m which occurs at well width L_{zm} for a given ΔE_v . This feature may explain maximum quantum efficiency measured by Welch, etc.[8] Moreover, the value of ΔE_m increases and L_{zm} decreases with increasing ΔE_v .

2.3 Determination of Valence Band Offset of AlGaAs/GaAs

In this section, the simple model used in the previous section for calculating ΔE is further justified and the approach for determination of the valence-band offset of GaInAs/AlInAs system is extended to determine the counterpart at GaAs/AlGaAs hetero-interfaces. It is shown that one can also determine ΔE_v and

ΔE_c very accurately for GaAs/AlGaAs system by measuring the values of ΔE's from optical transitions for a set of ultrathin quantum wells: $15\mathring{A} < L_z < 80\mathring{A}$. The calculated results of ΔE vs. L_z are presented and compared with available experimental data[16-20] in the literature. Our results indicate that the fraction number (Q_v) to the total band discontinuity (ΔE_g) for GaAs/AlGaAs system is not a close issue and this issue can be settled by systematically measuring data of ΔE's in sensitive well width range.

Various values of the parameter $\Delta E_v = Q_v \Delta E_g$, where $\Delta E_g = 1247x$ meV is assumed, and various set of hole masses have been used in Eq.(2-2-1) to generate ΔE vs. L_z curves-1 to 7 in Fig.(2-3-1) for GaAs/Al_x Ga_{1-x}As quantum well structure to test the validity of our approach. The change in hole effective masses is essential[21] to describe the measured spectra by Miller *et al.*[17,18], in particular for $\Delta n \neq 0$ transitions. Relying on that, an apparent new valence-band offset was determined for GaAs/AlGaAs system. A careful attention was paid to choosing the values of hole effective masses by which the band offset ΔE_v and Q_v are determined by us based on the available experimental data.[16-20] We have chosen here to use most reliable measured cyclotron masses[22] in the [100] L_z direction, $0.087m_0$ for lh, $0.403m_0$ for hh, respectively for our determination. In order to further eliminate the possible deviations due to the simple constant-mass picture, various sets of hole masses for GaAs were tested in such a way so that the curves of ΔE vs. L_z will deviate most from the curve using the above masses. For example, the solid curve-4 was calculated using the [100] masses[22] and a value of ΔE_v=75meV. The masses for generating curve-1, 2, and 3 are the density-of-states effective masses[21], the masses initially used by Dingle[3] and the new set of masses proposed

by Miller *et al.*[5], respectively. The same value of ΔE_v=185meV was used for those three dot-dash curves. Variations on hole effective masses can not compensate the larger calculated ΔE than measured ΔE due to large value of $\Delta E_v(Q_v=0.40)$. The effective masses for the holes of alloy barriers were obtained from a linear extrapolation as function of x from the hole masses of AlAs defined by Luttinger parameters γ_1=3.45 and γ_2=0.68 given in Ref.23. All parameters used for the various curves plotted in Fig.(2-3-1) are described in Tab.(2-3-1).

The most significant features appearing in those curves plotted in Fig.(2-3-1) should be addressed here despite of very different masses used. There are two distinct regions for well widths L_z from calculated curves. One *region* is called the *sensitive range* ($15\text{Å} < L_z < 80\text{Å}$) in which ΔE's are very sensitive to the value of ΔE_v in spite of various sets of masses for hh and lh [see Tab.(2-3-1)]. In this region, it is possible to determine ΔE_v very accurately by fitting ΔE's to the experimental data. One can also clearly show whether or not the recent trend of determination of ΔE_v is correct and was determined without any ambiguity. The other region ($L_z > 80\text{Å}$) is called the *insensitive range* in which ΔE's are very insensitive to the choice of ΔE_v. In fact, the lowest energy levels can often be adequately found by using the " infinite-well " approximation for thick wells. Therefore, it is very hard in practice to determine ΔE_v by fitting transition energies from the thick quantum wells. Since most previous optical measurements were performed on quantum wells with $L_z > 80\text{Å}$,this feature from the curves explains why different values of Q_v were obtained from study to study. Our calculations also show that varying Q_v from 0.10 to 0.50 does not alter the energies of low lying optical transitions by much for $L_z > 100\text{Å}$. For example, for a single quantum

well with the values of L_z =100Å and x=0.30, the calculated variation of energy for n=1 electron to n=1 heavy-hole transition is only 3meV for wide variation of Q_v from 0.10 to 0.50. The energy separation between n=2 hh and lh subbands are not sensitive at all to ΔE_v when L_z > 180 Å (see similar work in Ref.24 in this respect).

Three key advantages should be emphasized here for determining ΔE_v in the sensitive range of well widths by fitting the experimental data ΔE to the calculated ΔE. First, the mixing between the hh and lh bulk states can be neglected since the values of ΔE are relatively large. Furthermore, from the results of multiband effective-mass approach the valence-band mixing affects higher subbands (n > 1) resulting in poor description of dispersion of hole bands and ambiguous identification of transitions among all pairs of valence and conduction subbands [25] and possible impurity states involved. However, lowest subbands (n=1) remain unaffected. Therefore, the envelope-function approximation for n=1 subbands is realistic.[26] One can almost exactly determine ΔE at defined well widths. This accuracy is crucial to infer band offsets. Second, the influence of band bending can be also neglected since the wells are thin enough. Third, the effects of any possible symmetric, linear interface grading is to increase the eigen-energies of all confinement states.[27] Although it may be sensitive for L_z < 50Å, ΔE which is the energy difference of hh and lh states may remain relatively unchanged. It should be pointed out that the effects of errors in determination of L_z can be overcome by systematically comparing the derived value of L_z using contouring approach[28] with that determined by the RHEED oscillation technique or real-time layer growth rate. In fact, one can estimate Al composition x as accuracy as 0.4%.[29]

Therefore, by knowing x and the nearly exact measured energies of transitions from n=1 electron states to both hh and lh states, the well width L_z can be determined very accurately since those transitions depend strongly on this parameter (because L_z is small).

Since the energy difference of electron-hh exciton and electron-lh exciton is relatively small (< 2meV), we did not include the dependence of exciton binding energy on L_z in our calculation. However, we took 1 $\sim$ 2meV reduction from the measured ΔE to account for the binding energy difference. In order to further justify this point the two dot curves are also plotted in Fig.(2-3-1) from the data in Tab.(2-3-1) of Ref.30 in which the different exciton binding energy for hh and lh at different L_z was considered. The upper one corresponds to x=0.3 (ΔE_v=45meV for Q_v=0.12) while the lower one corresponds to x=0.15(ΔE_v=22meV for Q_v=0.12). The masses used[30] were $m_{whh}=0.45m_0$, $m_{wlh}=0.082m_0$, $m_{bhh}=(0.45+0.2x)m_0$ and $m_{blh}=(0.082+0.068x)m_0$ which are different from masses we used. However, all three features discussed above are preserved.

In this section, the available experimental data[16-20] of ΔE vs. L_z in *sensitive range* are used to determine ΔE_v and Q_v according to our calculation. The data denoted by the triangle at location (L_z =42Å, ΔE=28.5meV) in Fig.(2-3-1) was taken from the excitation spectrum at 6K given in Ref.16. The composition number x for the Al is 0.37. This data yields a value of ΔE_v=75 meV which corresponds a fraction number Q_v=0.16. Using the data denoted by solid triangles in Fig.(2-3-1) from the other group[19] yield Q_v=0.14. Data on ΔE from the other Refs.17, 18, 20 are also displayed in Fig.(2-3-1). Using our calculation the data consistently yield a fraction number Q_v=0.12. It is interesting to note that samples cited here were

mainly grown in the [100] direction at Bell and Philips laboratories (except the sample studied in Ref.16). Those samples consistently yield an approximately same fraction number Q_v when the most accurate optical data ΔE and the most reliable effective masses in the growth direction were used in the sensitive range.

Recently, there have been reports suggesting Q_v=0.40.[5] It is necessary to show how Q_v=0.40 fails to fit the experimental data[16-20] in the *sensitive range.* For example, let us take the data of Ref.16. When Q_v=0.40 ($\Delta E'_v$=185meV for x=0.37) and the *new* set of masses ($0.340m_0$, $0.094m_0$) for hh and lh of GaAs proposed by Miller *et al*[5] for GaAs/AlGaAs system were used by us for data fitting, a value of $\Delta E'$=46meV was obtained which does not fit the observed value of ΔE = 28.5meV.[16] Including nonparabolicity in our calculation only make a insignificant reduction about 1.5meV from 46meV. Also, our calculation does not yield the observed values of ΔE[17-20] using Q_v=0.40 for both the conventional masses[22] and the *new* set of masses[5]. It should be pointed out here that *new* set of mass parameters[5] including fraction number Q_v =0.40 for GaAs/AlGaAs system, deduced from the measurements of optical transitions in thick quantum wells (for $L_z > 80$ Å) and in parabolic quantum well are not determined uniquely. These results[5] are subject to large errors for finding Q_v because of the insensitivity of ΔE vs. L_z for the choice of ΔE_v for $L_z > 80$Å. Moreover, using smaller value of effective mass for hh in quantum well over the conventional bulk value is not consistent with the $\vec{K} \cdot \vec{P}$ theory since effective mass for a particle away from the band edge is in general larger than at the edge.[30]

Data from various sources[16-20] are summarized in Tab.(2-3-1) The values of ΔE_v and Q_v are obtained by our model.

2.4 Discussion

We have used a simple model for calculating the energy separation ΔE between maxima of hh and lh subbands and showed how the valence-band discontinuity at the interface of different semiconductors can be determined by fitting this right quantity ΔE to the experimental data measured in the right region of parameter space (the *sensitive range* of well thicknesses 15 to 80Å).

We have also noticed that the theoretical calculated quantity of ΔE is also sensitive to the boundary conditions at the interfaces in the *sensitive range* of L_z. In Fig.2-4-1, we have plotted the ΔE as function of L_z using three different sets of boundary conditions with the material parameters as used for the curve-4 in Fig.2-4-1 except $Q_v = 0.27$. The solid curve is for the Bastard's boundary conditions.[32] The broken curve is for the conventional[3] as well as χ-normality boundary conditions.[33] The dot-dashed curve is for the *new connection rules* recently introduced by Ishibashi *et al.*[34] A data point from Ref.16 is also indicated in the figure as a triangle. From these plotted curves one can clearly see the differences among different sets of boundary conditions used in the theoretical calculations. This gives rise the question which set of boundary conditions should be used in the determination of band offsets by comparing the measured and calculated ΔE. Experimental data in the *sensitive range* are compared with the calculated results for the GaInAs/AlInAs and GaAs/AlGaAs systems yielding an agreement with Dingle's initial work[3]: $\Delta E_v \approx 0.15 \Delta E_g$ using either the conventional[3] and χ-normality[33] boundary conditions. By adopting the Bastard's boundary conditions[32] and the conventional hole masses[22,23] the fractional number Q_v is more favorable[35]

to be 0.27 using the experimental data[16–20] in the sensitive range. The most recent resonance Raman scattering data[36] seems to support the value of 0.30. However, using the new connection rules and the *new* heavy-hole effective mass $m_{hh} = 0.340 m_0$ proposed by Miller *et al.* [5] Ishibashi et al.[34] have demonstrated that the Dingle's rule still holds for the GaAs/AlGaAs.

The essential point of our work is to demonstrate what experimental data from optical transitions should be used and how it is sensitive to the Q-value of band offsets. To precisely determine ΔE_v using optical transitions in quantum well structures, more measurements should be performed in the sensitive range of well width: $15\mathring{A} < L_z < 80\mathring{A}$.

Reference

1. A. D. Katnani and G. Margaritondo, Phys. Rev. B 28, 1944(1983).

2. H. Kroemer, Wu-Yi Chien, J. S. Harris,Jr. , and D. D. Edwall, Appl. Phys. Lett. 36, 295(1980).

3. R. Dingle, W. Wiegmann, and C. H. Henry, Phys. Rev. Lett. 33, 827(1974).

4. H. Okumura, S. Misawa, S. Yoshda, and S. Gonda, Appl. Phys. Lett. 46, 377(1985).

5. R. C. Miller, D. A. Kleiman, and A. C. Gossard, Phys. Rev. B 29, 7085(1984).

6. G. Duggan, J. Vac. Sci. Technol. B3(4), 1224(1985).

7. W. I. Wang, T. S. Kuan, E. E. Mendez and L. Esaki, Phys. Rev. B 31, 6890(1985).

8. K. Shum, P. P. Ho R. R. Alfano, D. F. Welch, G. W. Wicks, and L. F. Eastman, Phys. Rev. B 32, 3806(1985).

9. S. S. Yao and R. R. Alfano, Phys. Rev. Lett. 49, 69(1982).

10. P. Lawaetz, Phys. Rev. B 10, 3460(1971).

11. J. S. Blakemore, *Semiconductor Statistics* (Pergamon Press) P. 35 (1962).

12. D.V.Morgan, K.Board, C.E.C.Wood, and L.F.Eastman, Phys.Status Solidi A72, 251(1982).

13. R. People, K. W. Wecht, K. Alavi, and A. Y. Cho, Appl. Phys. Lett. 43, 118(1983).

14. W. A. Harrison, J. Vac. Sci. Technol. 14, 1016(1977).

15. J. S. Weiner, D. S. Chemla, D. A. B. Miller, T. H. Wood, D. Sivco, and A. Y. Cho, Appl. Phys. Lett. 47, 619(1985).

16. R. C. Miller, D. A. Kleinman, W. T. Tsang, and A. C. Gossard, Phys. Rev. B 24, 1134(1981).

17. R. C. Miller, A. C. Gossard, G. D. Sanders and Y. C. Chang, Phys. Rev. B 32,8452(1985).

18. P. Dawson, G. Duggan, H. I. Ralph, and K. Woodbridge, Phys. Rev. B 28, 7381(1983).

19. G. Duggan, H. I. Ralph, and K. J. Moore, Phys. Rev. B 32, 8395(1985).

20. Daniel S. Chemla, Phys. Today 57 (May 1985).

21. Increase in hh mass is to lower the hh states while decrease in lh mass is to lift the lh states resulting in smaller ΔE. However, masses are less critical in Ref.21. They even used density-of-states (DOS)effective masses for their fitting. Therefore, we also tested DOS effective masses given by P. Lawaetz, Phys. Rev. B4, 3460(1971) for comparison (topmost curve 1).

22. M. S. Skolnick, A. K. Jain, R. A. Stradling, J. Leotin, J. C. Ousset, and S. Askenasy, J. Phys. C9,2809(1976).

23. E. Hess, I. Topol, K. R. Schulze, H. Neumann, and K. Unger, Phys. Status Solidi B55, 187(1973).

24. W. Porod, W. Potz, and D. K. Ferry, J. Vac. Sci. Technol. B3(4), 1290(1985).

25. G. D. Sanders and Y. C. Chang, Phys. Rev. B31, 6892(1985).

26. J. N. Schulman and Yia-chung Chang, Phys. Rev. B 31, 2056(1985).

27. J. N. Schulman, J. Vac. Sci. Technol. B1, 644(1983).

28. P. Dawson,G. Duggan, H. I. Ralph, K. Woodbridge, and G. W. 't Hooft, superlattice and microstruct. 1, 231(1985).

29. M. H. Meynadier, C. Delalande, G. Bastard, and M. Voos, Phys. Rev. B31, 5539(1985).

30. Tsin-Fu Jiang, Solid State Comm. 50, 589(1984).

31. J. C. Maan, G. Belle, A. Fansolino, M. Altarelli, and K. Ploog Phys. Rev. B 30,2253(1984).

32. G. Bastard and J. A. Brum, IEEE J. of Quantum Electronics, QE-22, 1625(1986).

33. H. Kromer and Q. G. hu, J. Vac. Sci. Technol. 21, 551(1982).

34. A. Ishibashi, Y. Mori, K. Kanneko, and N. Watanabe, J. Appl. Phys. 59, 4087(1986).

35. C. Zhang, K. Shum, and R. R. Alfano, (unpublished).

36. J. Menendez, A. Pinczuk, D. J. Werder, A. C. Gossard, and J. H. English, Phys. Rev. B 33, 8863(1986).

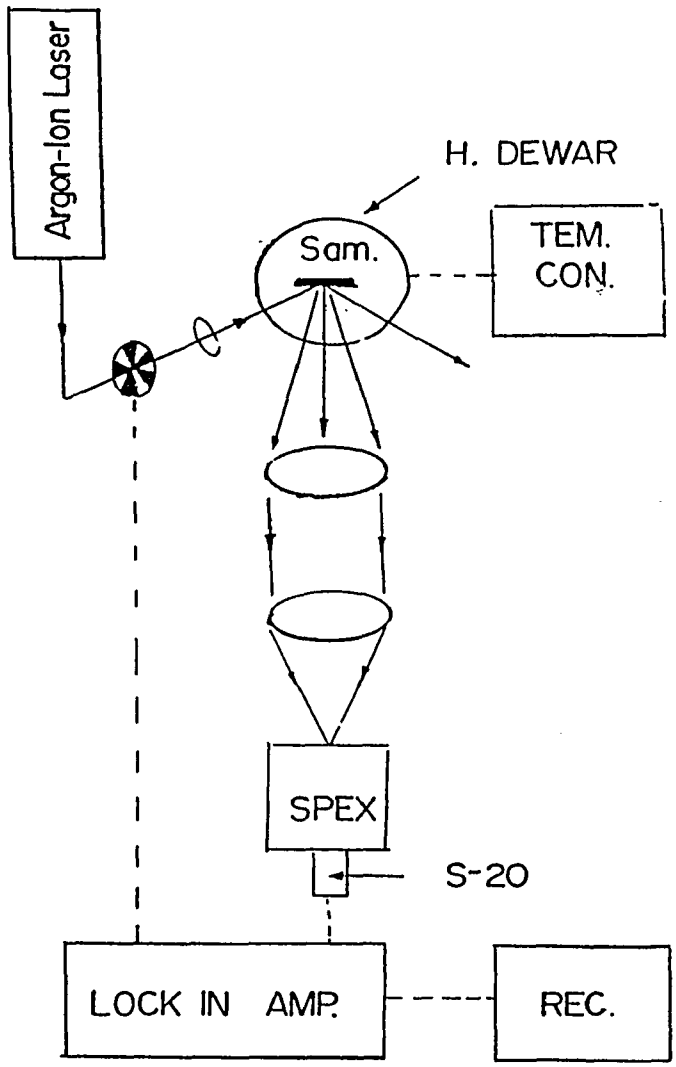

Fig.(2-2-1) The steady-state photoluminescence set-up.

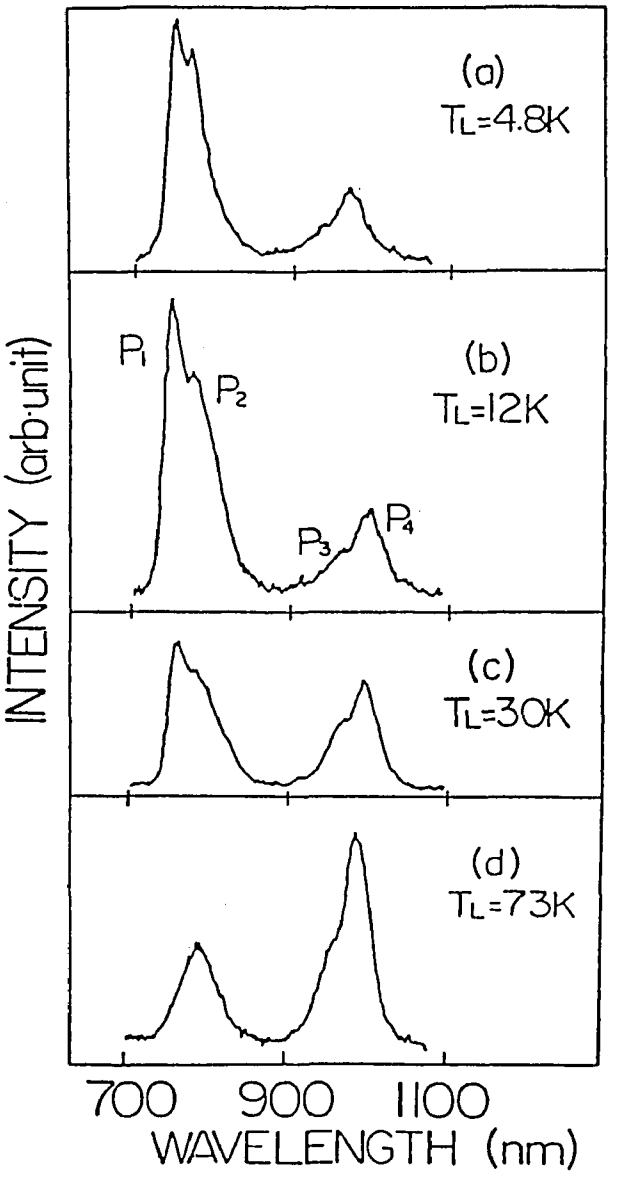

Fig.(2-2-2) Photoluminescence spectra of a AlInAs/GanAs SQW at L_z =14.5Å as function of T_L. Excitation power density was about $10^2 W / cm^2$. The peaks P_1, P_2, P_3, and P_4 are explained in the text.

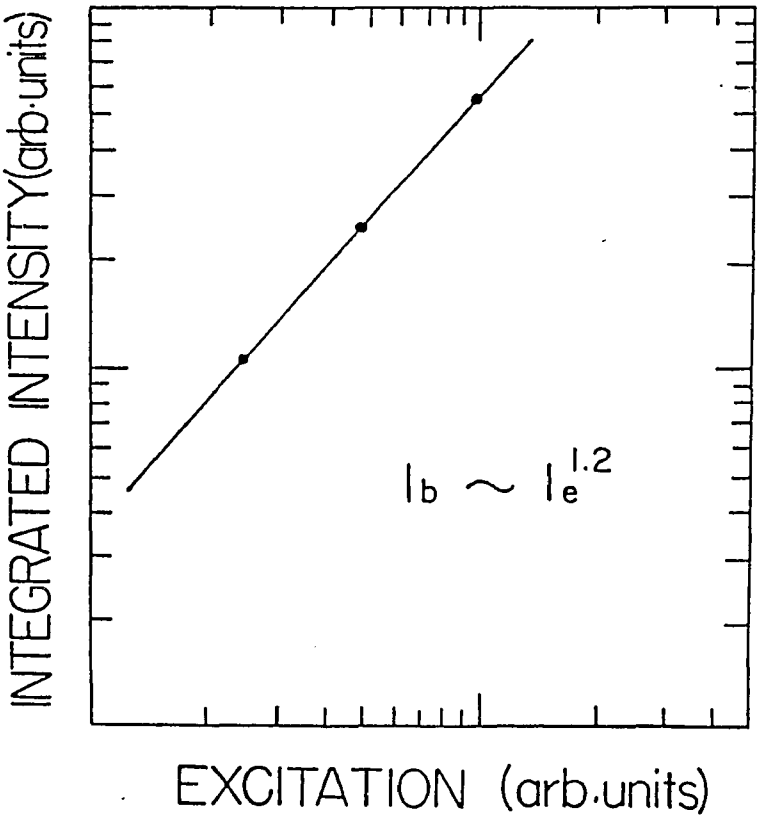

Fig.(2-2-3) Intensity dependence of emission from barriers of 14.5Å-SQW with respect to excitation power density I_e.

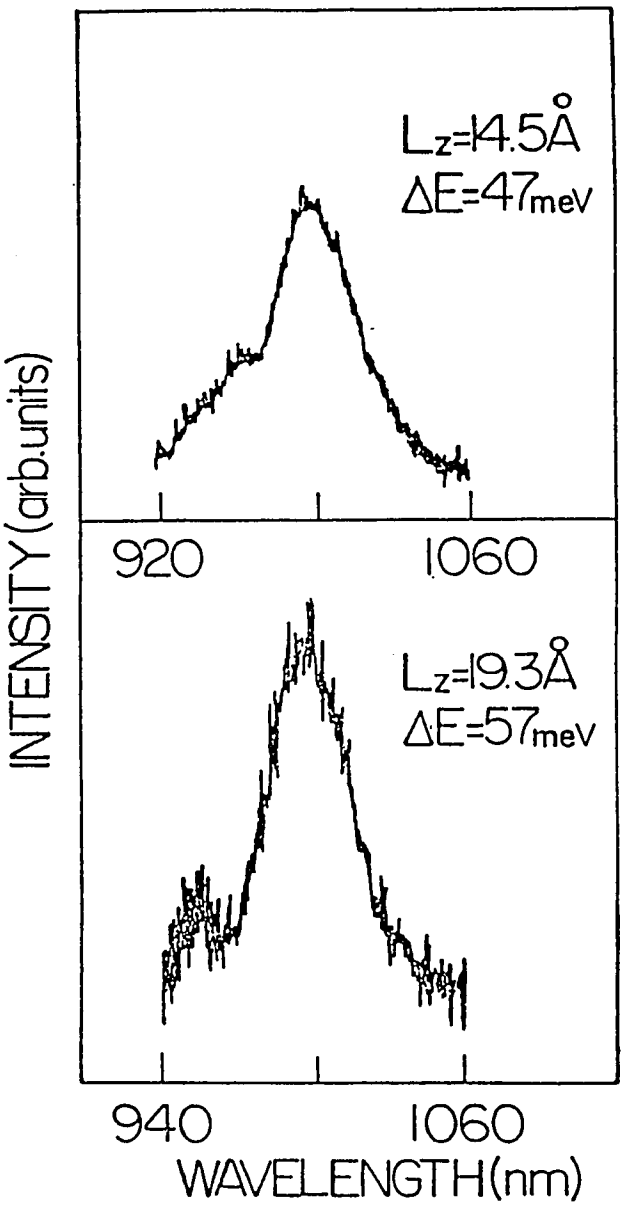

Fig.(2-2-4) SQW photoluminescence spectra from well GaInAs of two narrow wells at T_L =7K. The energy separations ΔE=47 and 57meV between hh and lh subbands for L_z =14.5 and 19.3Å, respectively, are indicated in each curve.

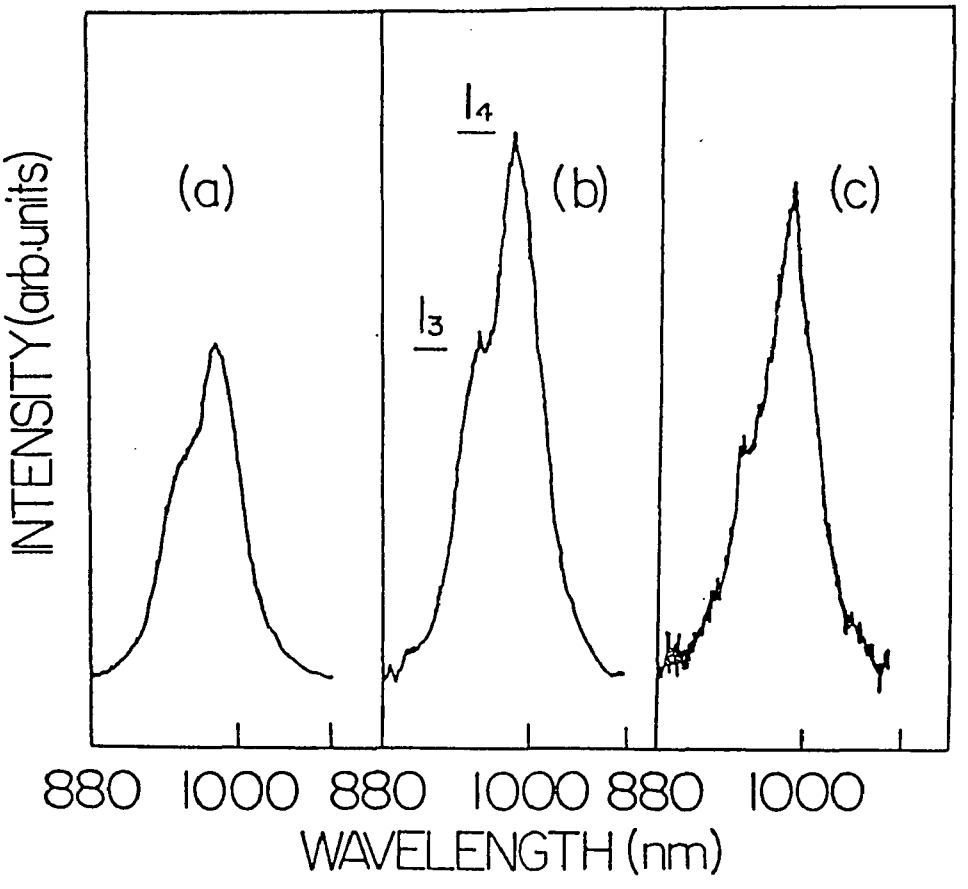

Fig.(2-2-5) SQW photoluminescence spectra from GaInAs well region for L_z =14.5 Å with different excitation power P_e at T_L =7K. The peak intensity are denoted as I_3 and I_4. (a)P_e =160mW, (b)P_e =80mW, (c)P_e =40mW.

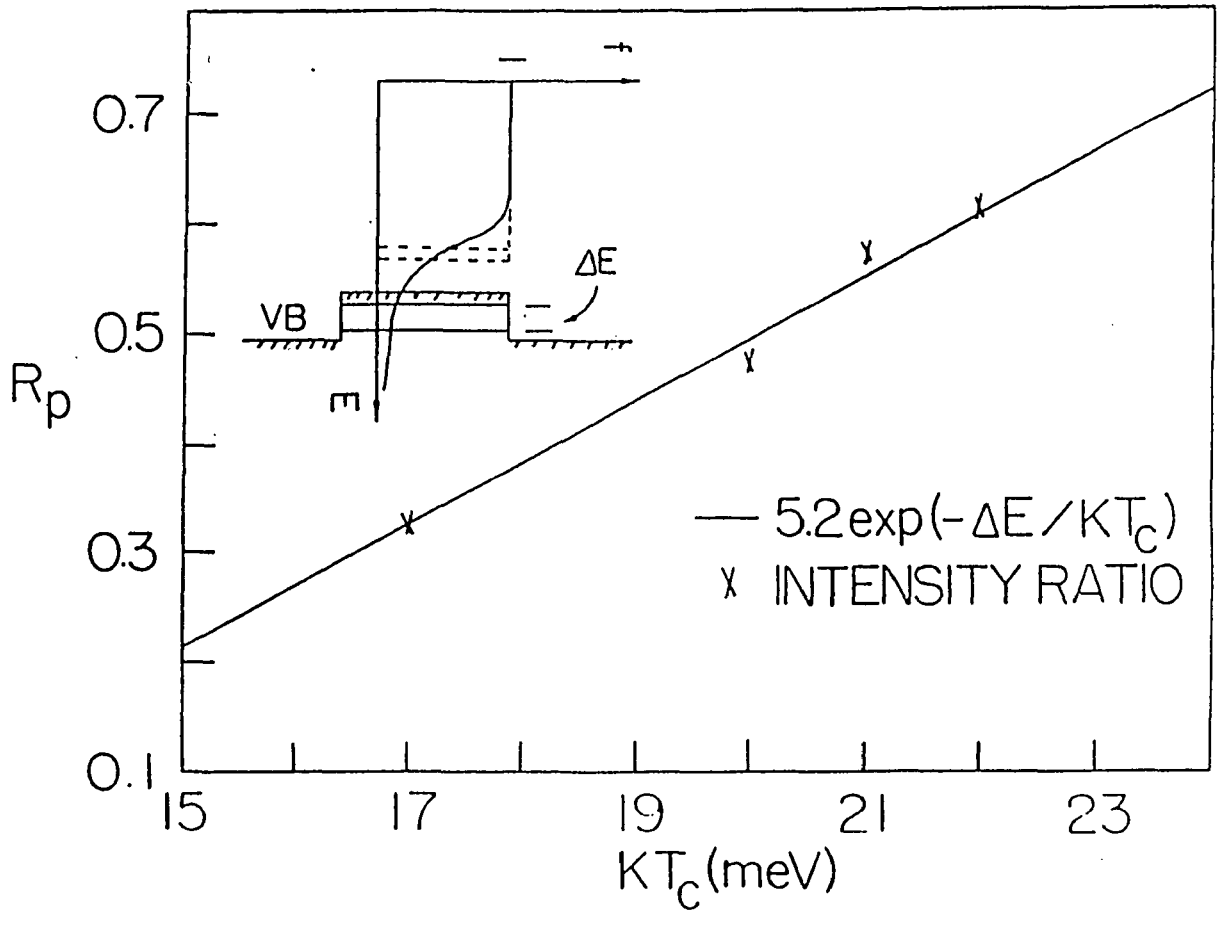

Fig.(2-2-6) Ratio of peak intensity of I_3 and I_4 with respect to the $k_B T_c$. The inset shows a Fermi-Dirac function.

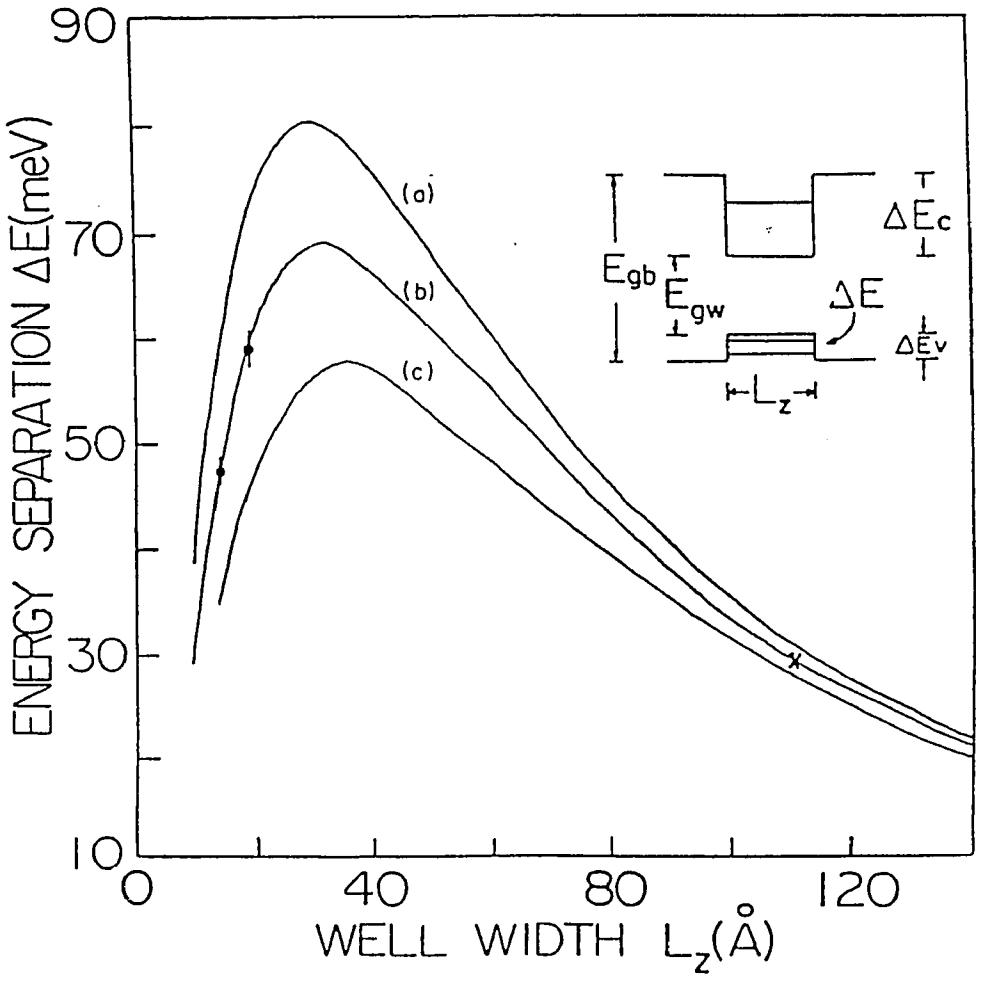

Fig.(2-2-7) Calculated ΔE as function of L_z with ΔE_v as a parameter for GaInAs quantum well. (a) ΔE_v =140meV, (b) ΔE_v =120meV, and (c) ΔE_v =100meV. The dots are our data from PL and a cross is the data from Ref.15. The inset shows approximate band diagram of a SQW.

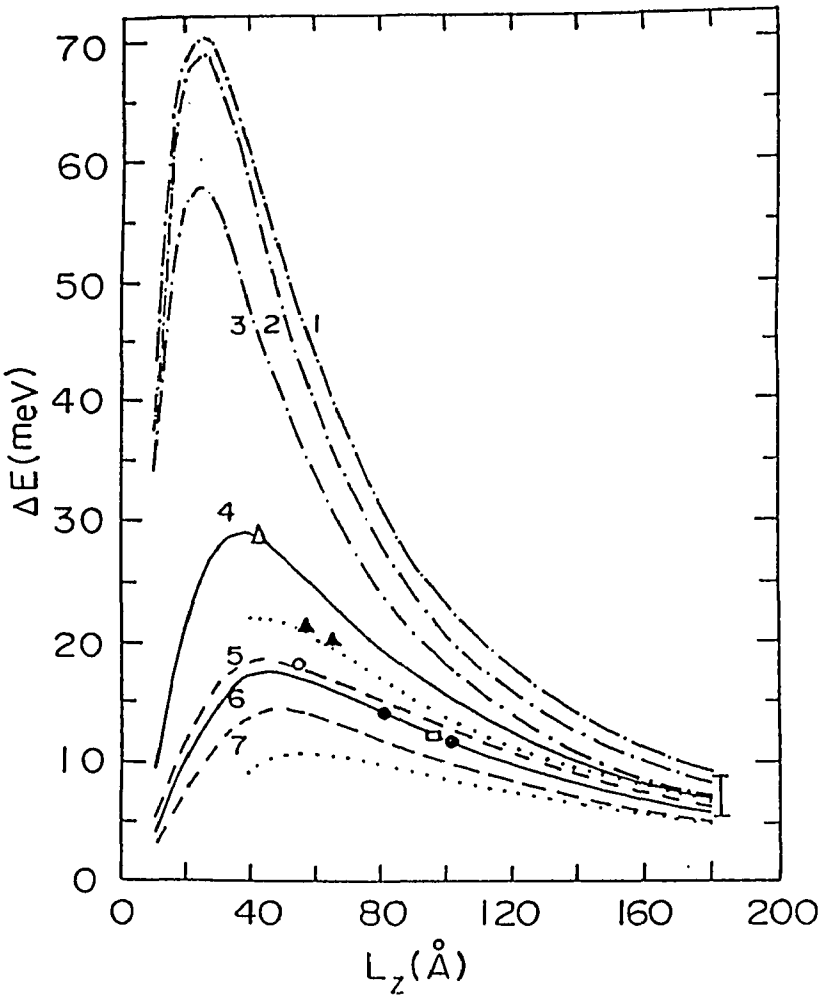

Fig.(2-3-1) Calculated ΔE vs. L_z for various ΔE_v and hole masses described in Tab.(2-3-1) for GaAs quantum well structures. Two dot curves were extrapolated from Ref.30, where exciton binding energies were calculated. The composition number x for upper and lower dash curves were 0.30 and 0.15, respectively. The open triangle corresponds to the data taken from the excitation spectrum of Ref.16. The solid triangles are from excitation spectrum of Ref.19. The open circle is from the photoluminescence spectrum of Ref.18. The square is from the absorption spectrum of Ref.20. Two close circles are from excitation spectrum of Ref.17. The error bar illustrates the insensitivity of ΔE vs. L_z to the choice of ΔE_v.

Curve	x	Q_v	ΔE_v	m_{hh}	m_{lh}	Ref. for mass
1	0.37	0.40	185	0.620	0.074	18
2	0.37	0.40	185	0.450	0.080	3
3	0.37	0.40	185	0.340	0.094	5
4	0.37	0.16	75	0.403	0.087	19
5	0.30	0.12	46	0.450	0.080	3
6	0.30	0.12	46	0.403	0.087	19
7	0.30	0.12	46	0.340	0.094	5

Tab.2-3-1. The parameters used for generating curves plotted in Fig.(2-3-1). Unit of mass is in m_0.

ΔE	L_z	X	ΔE_v	Q_v	$\Delta E_v'$	$\Delta E'$
28.5[a]	42	0.37	75	0.16	185	46
21[b]	56.6	0.36	63	0.14	180	33
20[b]	65	0.36	63	0.14	180	29
18[c]	55	0.33	49	0.12	165	34
12[d]	96	0.30	46	0.12	150	17
14[e]	81	0.30	46	0.12	150	21
11.5[e]	102	0.30	46	0.12	150	15

Tab.(2-3-2) The available experimental data of ΔE in the literature. The values of ΔE_v and Q_v are obtained by our model. The super subscript " ' " denotes the corresponding values using Miller's *new* set of parameters ($0.34m_0$ for hh mass, $0.094m_0$ for lh mass and Q_v=0.40) given in Ref.5. Unit of energy is in meV. [a From Ref.16. b From Ref.19. c From Ref.18. d from Ref.20 e from Ref.17]

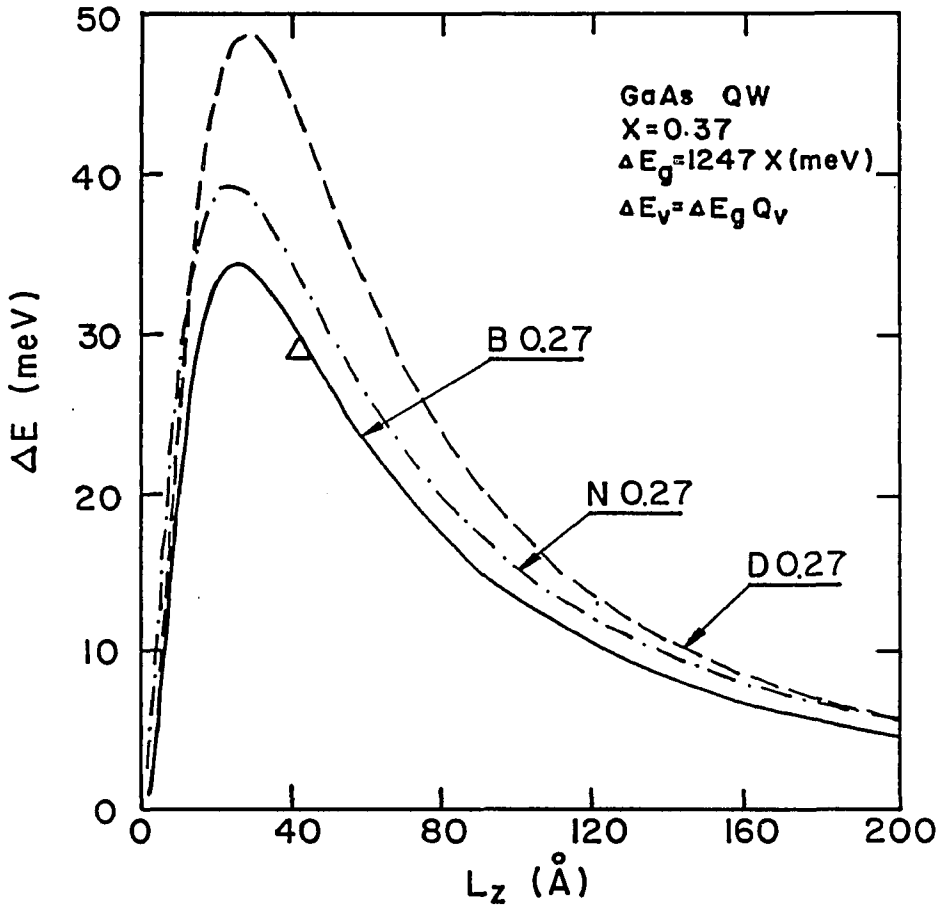

Fig.(2-4-1) Calculated ΔE as function of L_z using various sets of the boundary conditions (B. C.) with material parameters as used for the curve-4 in Fig.(2-3-1) except Q_v = 0.27, broken curve (conventional B. C., Dingle), solid curve (Bastard's B. C.), and dot-dashed curve (new connection roles, Ishibashi). The open triangle corresponds to the data taken from the excitation spectrum at 6K of Ref.16.

Chapter 3

Electron-Phonon Scattering in Quantum Wells

3.1 Introduction

Recently, there has been a considerable interest in the transport and optical properties of photogenerated carriers which are confined in quantum wells. Knowledge of the hot-carrier behavior in semiconductor microstructures is needed to develop small and fast optoelectronic devices. A key factor that affects photogenerated carrier dynamics in quantum well structures is the electron-phonon (e-p) scattering rate which determines how fast carriers loss their excess kinetic energy to the host lattice. To assess and understand the differences of the electron-phonon scattering rate in quantum well structures from their bulk counterpart is of technological importance.

Previous studies have been performed related to e-p interaction in quasi-two-dimensional (quasi-2D) structures. Hess and his coworkers [1] predicted an enhanced e-p scattering rate over the bulk semiconductor by a factor of $3.5(E_{LO} / E)^{1/2}$ for $E_{LO} < E < 10E_{LO}$. Ridley[2] obtained a $1/L_z$ relationship of quasi-2D e-p scattering rate by introducing a momentum conservation approximation in well direction (MCA). Leburton[3] has shown that L_z effect has a rather weaker influence on longitudinal optical (LO) phonon and electron interaction than

Ridley's result.

From theoretical point of view, it is important to take into account the effect of electron confinement on the scattering of electrons by polar optical phonons (POP) in quantum wells.[1-4] The Hamiltonian $\hat{H}$ of the electron system and the operator $\hat{k}_z$ for the electron momentum in z-direction do not commute with each other because of the potential profile experienced by electrons in the confinement z-direction. That is,

$$[\hat{H}, \hat{k}_z] = i\frac{d}{dz}\hat{V}(z) \quad , \tag{3-1-1}$$

where $\hat{V}(z)$ is the potential operator in z-direction. The usual conservation law of momentum in z-direction:

$$q_z = \pm k_z \mp k'_z \tag{3-1-2}$$

must be modified in the sense that q_z, k'_z and k_z are no longer deterministic observable variables but are **random variables** (r.v.). Here, q_z is the z-component of the phonon wave vector, k_z and k'_z are the electron wavevectors in z-direction before and after scattering, respectively. The statistics of the each r.v. is characterized by its probability density function. The pioneering work of Hess[1], Price[4] and Leburton[3] essentially adopted a "non-momentum-selection rule" in z-direction for calculation of phonon emission and phonon absorption rates. They treat q_z as a regular deterministic variable. Although Ridely[2] realized "fuzzy momentum conservation" in z-direction, he used instead a "momentum conservation approximation". Furthermore, the value of k_z in wave function in the coordinate representation was considered as the electron momentum in z-direction in his

analysis. This approach is not valid since k_z is equal to a precise value of π/ L_z in an "infinite well" approximation and for a "finite well" k_z is just a parameter that related to the eigen-value of the Hamiltonian of the electron system.

Although theoretical calculations predict a somewhat enhanced e-p interaction in quasi-2D structures, the experimental results by many groups[5-7] have showed a much slower hot-electron cooling rate. The explanation for this is very much complicated by the presence of screening of electron-phonon interaction and of nonequilibrium phonons. One can not distinguish the various mechanisms that cause the slow hot-electron cooling rate in a particular experiment. Therefore, it is very difficult to quantitatively verify the theoretical results mentioned above.

In this chapter, a theoretical analysis of electron scattering by POP in Quasi-2D structures placing emphasis on confinement effects is developed by taking into account the non-commutation relationship between the Hamiltonian operator $\hat{H}$ and the electron momentum operator $\hat{k}_z$. An experiment used to demonstrate the confinement effects is also described.

3.2 Theoretical Calculation

In this section, we theoretically show how "fuzzy momentum conservation" in z-direction is exactly treated using neither the "non-momentum-selection rule" nor the "momentum conservation approximation" but by considering the q_z as a random variable. The results that distinguish this work from the previous work[1-4] are (i) the phonon emission rate at the onset is shown to be 3 times smaller than previously reported, (ii) the rate has a weaker L_z dependence, and (iii) the rate increases with initial electron energy. The use of random varible is a

main point to our understanding of dynamics of carriers in confined structures.

There are two important aspects of the noncommutation relationship given by Eq.(3-1-1). First, the corresponding observables can not be measured simultaneously with arbitrary accuracy. The product of their quantum root-mean-square deviation must not be less than the half of the quantum expectation value of the operator $i\frac{d\hat{V}(z)}{dz}$ in a given state. Second, the electron energy due to the motion in z-direction has no correlation with the corresponding electron momentum in this direction. The eigen-value of momentum operator $\hat{k}_z$ can not precisely determined due to the electron confinement by the potential well and must be considered as a random variable. When an electron is restricted in the first bound state the quantum expectation value of $[\hat{H}, \hat{k}_z]$ is zero resulting in a precise determination of the lowest eigenvalue of operator $\hat{H}$ and root-mean-square deviation for k_z can be determined. Those two points play the key role in calculating the electron-POP scattering rate.

In our analysis, the unscreened electron-POP interaction, equilibrium bulk phonon spectrum and an infinite depth square well with the lowest subband occupied are assumed.

Within the framework of the effective-mass-approach the wave function for electron in coordinate representation are then given by

$$|k\rangle = \frac{e^{i\vec{k}\vec{r}}}{\sqrt{A}}\phi(z), \qquad (3\text{-}2\text{-}1)$$

where

$$\phi(z)=\sqrt{\frac{2}{L_z}}\sin\frac{\pi z}{L_z} \tag{3-2-2}$$

is the wave function in z-direction describing the bound state. The vectors $\vec{r} = (x, y)$ and $\vec{k} = (k_x, k_y)$ denote the two dimensional electron position and the wavevector parallel to the interfaces, respectively. The corresponding electron energy can be expressed as

$$E = \frac{\hbar^2 k^2}{2m} + E_z , \tag{3-2-3}$$

where

$$E_z = \frac{\hbar^2 \pi^2}{2m L_z^2} . \tag{3-2-4}$$

Here m is the isotropic electron effective mass, L_z is the well width and A is the layer area.

The probability density function for the r.v. k_z can be obtained from the wave function given by Eq.(3-2-2) by a representation change to the wavevector space using

$$\phi(k_z) = \frac{1}{\sqrt{2\pi}}\int_{-\infty}^{\infty}\phi(z)\, e^{-ik_z z}\, dz . \tag{3-2-5}$$

This yields

$$\rho(k_z) = |\phi(k_z)|^2 = \frac{4L_z \cos^2(k_z L_z / 2)}{\pi^3(1-k_z^2 L_z^2/\pi^2)^2} . \tag{3-2-6}$$

Since there exists a "fuzzy momentum conservation law"[3] in z-direction given by Eq.(3-1-2), the probability density function for the r.v. q_z, $\rho(q_z)$, can be obtained from the convolution expression:

$$\rho(q_z) = \rho(\pm k_z)^* \ \rho(\mp k'_z) \ . \tag{3-2-7}$$

The electron scattering rate ($w_{kk'}$) per unit area in k-space in Quasi-2D structures can be expressed in Born approximation by Fermi's golden rule by:

$$w_{kk'} = \frac{4\pi A}{\hbar (2\pi)^2} | M_{k'k} |^2 \delta(E_k - E_{k'} - \hbar\omega_0) \ , \tag{3-2-8}$$

where

$$M_{kk'} = \frac{-c (n_Q + 1)^{1/2}}{Q} \delta_{\vec{k}' - \vec{k} + \vec{q}} F(q_z, L_z) \tag{3-2-9}$$

with

$$c = i [\frac{e^2 \hbar\omega_0}{\bar{\epsilon} V_s}]^{1/2} \tag{3-2-10}$$

is the matrix element for the Frohlich electron-POP interaction. For simplicity we have only considered phonon emission process. Q and V_s denote the three dimensional phonon wavevector ($\vec{q}$, q_z) and the sample volume, respectively. The δ is a modified Kronecker function defined as

$$\delta_{a-b} = \begin{cases} 1 & \text{if } a = b \\ 0 & \text{if } a \neq b \end{cases} \tag{3-2-11}$$

The function F in Eq.(3-2-9) is the form factor in z-direction and is defined as:

$$F(q_z, L_z) = \frac{2}{L_z} \int_0^{L_z} e^{-iq_z z} \sin^2 \frac{\pi z}{L_z} dz \ , \tag{3-2-12}$$

where the exponential factor $e^{-iq_z z}$ is not a phonon wave function in z-direction (since it is no longer a plane wave), but a Fourier component of phonon wave packet emitted by a electron at state $|k>$. The other treatments of wave vector q_z

(which is a r.v.) are as follows: (1) Set $q_z = 0$ (Ref. 1) and (2) q_z is consider to be deterministic variable[2-4] which implies that $e^{-iq_z z}$ is a phonon plane wave function in z-direction. These two treatments yield an overestimate of electron-phonon scattering rate in quasi-2D quantum well structures (see numerical results below). The essential point made here is to realize that the matrix element M_{kk} is the function of a r.v. q_z. Therefore, the w_{kk} also becomes a r.v.. The most likely value of the w_{kk} that can be experimentally measured is given by its expected value using the statistics associated with the r.v. q_z. This is,

$$\overline{w}_{kk} = \int_{-\infty}^{\infty} \rho(q_z) w_{k'k}(q_z) dq_z \quad . \tag{3-2-13}$$

The total emission rate is then given by

$$W_{kk} = \int \overline{w}_{kk} \, d\,\mathbf{q} \tag{3-2-14}$$

$$= \int\int I^{Quasi-2D}(q, L_z) \delta(E_k - E_{k'} - E_{LO}) \delta_{\mathbf{k}'-\mathbf{k}+\mathbf{q}} \, q dq d\theta$$

where

$$I^{Quasi-2D}(q, L_z) = I_0 \int_{-\infty}^{\infty}\int_{-\infty}^{\infty} g(x, y) dy dx \quad , \tag{3-2-15}$$

and θ denotes the angle between the $\vec{k}$ and $\vec{q}$. The factor I_0 is defined as:

$$I_0 = \frac{(n_Q + 1) e^2 q_0 \omega_0}{2\pi\bar{\epsilon}} \quad . \tag{3-2-16}$$

The function g(x,y) is given by:

$$g(x, y) = 0.1 \frac{z}{q^2 + x^2} \frac{\sin^2(\frac{xz}{2})}{[1-(xz/2\pi)^2]^2 (xz/2)^2} \tag{3-2-17}$$

$$\times \frac{\cos^2[(x+y)z/2]\cos^2(yz/2)}{[1-(x+y)^2z^2/\pi^2]^2[1-y^2z^2/\pi^2]^2}$$

with $z \equiv q_0 L_z$, which includes $1/Q^2$ from Frohlich electron-POP interaction Hamiltonian, the form factor in z-direction and the probability density function $\rho(q_z)$ for r.v. q_z. All the wave vector are normalized by $q_0 = \sqrt{\frac{2m\omega_0}{\hbar}} \equiv L_0^{-1}$, where L_0 is about 40Å for GaAs and ~ 45Å for $Ga_{0.47}In_{0.53}As$.

The integral $I^{Quasi-2D}$ given by Eq.(3-2-15) for Quasi-2D structures represents the electron-POP interaction strength as function of q. It contains all the information about confinement effects as well as size effects[3] on the scattering rates. In order to further understand how electron confinement make the difference in the electron scattering rate between Quasi-2D structures and its bulk counterpart, a plot of the electron-POP interaction strength I^{3D} versus q for 3D electron system is needed in such a form that can be compared with $I^{Quasi-2D}$. It can be shown that

$$I^{3D}(q) = \frac{I_0}{q^2+\Delta k_z^{(-)2}} + \frac{I_0}{q^2+\Delta k_z^{(+)2}} \quad , \tag{3-2-18}$$

where $\Delta k_z^{(\mp)} = (k_z \mp k'_z)$. The first and second terms on the right side of Eq.(2-3-18) represent the scattering processes without and with change of initial direction of electron momentum, respectively. Since $\Delta k_z^{(\mp)}$ in Eq.(2-3-18) depends on both the magnitudes as well as the scattering angle θ , one can not find an explicit expression for $\Delta k_z^{(\mp)}$ in terms of q and θ unless a variational parameter for the

electron kinetic energy ratio ($r \equiv K^2 / k_z^2$) between the total kinetic energy and the energy due to the z-direction motion is introduced.

Using the momentum and the energy conservation laws for the 3D scattering process, the $\Delta k_z^{(\mp)}$ can be expressed as

$$\Delta k_z^{(\mp)} = \frac{(q^2+\xi) \mp \sqrt{(q^2+\xi)^2 - \xi 4q^2\cos^2\theta}}{2q\cos\theta\sqrt{r-1}} \qquad (3\text{-}2\text{-}19)$$

where $0 \leqslant \theta \leqslant arccos\sqrt{\frac{\hbar\omega_0}{E_k}}$ and $\xi = \frac{r-1}{r}$ with $1 < r < \infty$ The value of r=3 implies that the kinetic electron energy is equally distributed in all direction, while $r < 3$ more electron kinetic energy is in the z-direction. The exact 2D electron motion in x-y plane corresponds to the case when r approaches infinite.

The two solid curves in Fig.(3-2-1) show the probability density profiles for the r.v. q_z obtained from Eq.(3-2-7) for well width $L_z = 2L_0$ and $5L_0$. The larger well width L_z, the smaller is the variance of the density curve resulting in the less fuzzy momentum conservation in z-direction. The magnitudes of $F(q_z, L_z)$ versus q_z for $L_z = 2L_0$ and $5L_0$ are also displayed in Fig.(3-2-1) as two dotted curves. The two features from the plots should be noticed. First, in the limit $q_z \to 0$, $|F(q_z, L_z)|$ approaches unity independent of L_z reflecting *a scattering event* with an exact momentum conservation in z-direction. This is also the most favorable process according to the density curve for q_z. Second, for very thick well the $|F(q_z, L_z)|$ can be written as $\delta_{k_z - k_z - q_z}$ which implies the momentum conservation law for *any scattering event* and $\rho(q_z)$ approaches a δ-function for the bulk situation. **The fact that not every scattering event follows the**

exact momentum conservation law in z-direction is due to the electron confinement. This produces the weakening of electron-POP interaction in Quasi-2D structures.

The solid curves in Fig.(3-2-2) show the integral $I^{Quasi-2D}$ as function of the parallel component of phonon wave vector q with L_z as a parameter. Curves 1, 2, 3 and 4 are plotted in Fig.(3-2-2) for the value of L_z of $0.5L_0$, L_0 , $3L_0$ and $5L_0$, respectively. Our exact calculation procedure using the probability density function $\rho(q_z)$ for r.v. q_z yields a significant reduction by a factor 2 on the value of the integral $I^{Quasi-2D}$ obtained by Leburton[4] in the range from 0.1 to 4 for q. In spite of this key difference other features of our integral $I^{Quasi-2D}$ are very similar to what Leburton has shown.[4] Namely, the integral $I^{Quasi-2D}$ is a monotonic decreasing function of q for Quasi-2D electron system and weakly dependent on L_z. This similarity occurs just because the profile of probability density function for q_z happens to have similar shape as $|F(q_z, L_z)|$.

The interaction strength I^{3D} for 3D system with various values of θ and r are also displayed in Fig.(3-2-2) by the dotted curves 5 to 8. The values of r for curve 5, 6, and 8 are 10, 3, and 1.2, respectively. The value of θ for those three curves is set to be zero. The curve 7 with r=1.2 and $\theta=\pi/6$ is used to see the variation of $I^{3D}(q)$ by the change of the scattering angle θ. A comparison of the dotted curves 5 to 8 for 3D with the solid curves for Quasi-2D provides the physical insight into electron confinement in quantum wells. The following three points are discussed: First, the value of I^{3D} increases with increase of the value of r. It indicates that the electron-POP interaction strength for given value of q in the system with $r > 3$ is stronger than the system with $r \leq 3$. The reason for this

is the weakness of electron motion in z-direction resulting in small amount change of the electron momentum $\Delta k_z^{(\mp)}$. It should be emphasized that the value of $I^{Quasi-2D}$ at q as $L_z \to 0$ do not approach the value of I^{3D} with $r \to \infty$ which corresponds to the 2D case. In another words, as far as electron scattering process is concerned the Quasi-2D quantum well structure with $L_z \to 0$ is not equivalent to a 2D system due to the potential barriers which confine electrons inside the well. The values of I^{3D} and $I^{Quasi-2D}$ are close each other for the value of the ratio r between 1.2 to 1.5. This implies the origin of the difference in electron scattering between Quasi-2D and 3D systems comes from the fact that the electron kinetic energy is not equally distributed in all directions arising from electrons in the well obtain extra kinetic energy in z-direction from the potential barriers. These are important findings which were overlooked in previous works.[1-4]

Second, the larger scattering angle θ yield a larger value of I^{3D}. For $q > 1$, i.e., for the scattering processes in which electrons change their initial momentum direction, the value of I^{3D} is almost independent of θ and to be distinguished from various value of r by the second term of right hand side of Eq.(3-2-18). The value of $I^{Quasi-2D}$ is independent of θ and insensitive to the L_z for $q \leqslant 1$ giving rise a weak L_z dependence of total electron scattering rates. It also appears that the value of $I^{Quasi-2D}$ for $q > 1$ is more sensitive to L_z than for $q < 1$.

Third, a dent occurs in each dotted curve which becomes smaller when r increases. The position of the dent moves towards the smaller q when r decreases. It should be noticed that the dent does not appear in solid curves for Quasi-2D structures. This is because the non-commutation relationship given by Eq.(3-1-1) employed for Quasi-2D systems which gives rise that the momentum change in z-

direction does not correlate with the momentum change in the direction parallel to the quantum well interfaces.

The total normalized phonon emission rate (W_{kk} / W_0) in Quasi-2D quantum wells versus normalized energy E_k / E_{LO} is displayed in Fig.(3-2-3) by two solid curves. The normalization factor W_0 is given by $W_0 = 2mI_0/\hbar^2 q_0^2$. Using GaAs material parameter[8] a value of $1.24ps^{-1}$ is obtained. For comparison, the calculated results for Quasi-2D by Leburton[4] (dash curves) and for 3D (dotted curves) are also plotted in Fig.(3-2-3). The results of our approach clearly differs from the others[1-4] in two aspects. First, the Quasi-2D phonon emission rates for various L_z at the onset of phonon emission ($E_k / E_{LO} = 1$) are 3 times smaller than previously obtained.[1-4] Second, the phonon emission rate is a slowly increasing function of initial electron energy instead of being a decreasing function. The non-zero value of the phonon emission rate for $E_k = \hbar\omega_0$ stems from the nature of Quasi-2D density of states. For thick quantum wells ($L_z > 5L_0$) the phonon emission rate is about a factor of 2 smaller than 3D rate for $E_k / hbar\ \omega_0 > 2$ resulting from the weakening of the electron-POP interaction in z-direction for Quasi-2D case and neglecting higher intra-subband and inter-subband contributions. The Quasi-2D emission rate will approach the 3D result when $L_z \rightarrow \infty$ if all the contributions mentioned above are included. The phonon emission rate is comparable to the 3D rate for very thin quantum wells arising from the competition between Quasi-2D density of states and the weakening of electron-POP interaction strength in z-direction.

For completeness, it should be pointed out that the phonon absorption scattering rate can be treated in the same way as outlined here. One should expect

that the emitted phonon by Quasi-2D electrons traveling in the direction perpendicular to the quantum well interface may be easily reabsorbed. This is because those phonons are not plane-wave-like phonon mode that is extended to the whole sample. The phonons are localized inside the well as same as the localized electrons.

3.3 Experimental Investigation

This section reports on measuring the variation of temperature (T_c) of the thermalized hot electrons in quantum well with well width L_z using steady state photoluminescence spectra of various single quantum wells (SQW's) taken at 4K. This measurement allows us to compare the electron-phonon scattering in quantum wells as theoretically invoked in the last section. The steady state temperature of a Fermi electron gas is determined by the energy balance between the laser pumping and electron energy loss to the lattice through the electron-phonon scattering. The information about the variation of T_c on L_z can test the L_z dependence of phonon emission rate calculated using various approximation[1-4] as well as our exact calculation. The much higher carrier temperature than lattice temperature is described by a model taking into account the high carrier density and slow energy relaxation.

The T_c was determined using the method introduced by Shah,[9,10] namely, by fitting the high energy tails of photoluminescence (PL) spectra of electron system in a set of undoped (Al,In)As/(Ga,In)As SQW's for the different well width from $L_z = 14.5\text{Å}$ to $L_z = 130.5\text{Å}$. The observed variation of steady state electron temperature with L_z provides direct information about the quasi-2D electron and

LO-phonon scattering rate which we found to be independent of L_z within our experimental accuracy. The average energy loss rate per hot-electron was determined to be much smaller than 3D electron gas.[10] The intrinsic 2D electron degeneracy may cause further lowering of e-p interaction than 3D electron case when carrier density is high enough such that $E_{fe} - E_{cn} = k_B T_c \ln(n/N_c) > k_B T_c$, where E_{fe} is the quasi-Fermi level for electrons and E_{cn} is the energy level of the sub-conduction band edge. However, Shah et al.[7] have recently attributed this reduction in electron-energy-loss rate primarily to hot-phonon effect while hole-energy-loss rate is not significantly altered.

The epitaxial layers used in this study were also grown by a Varian MBE machine.[9] The structures were grown on a thermally cleaned InP substrate consisted of a 2500Å thick AlInAs layer followed by the GaInAs SQW's and 100Å layer of AlInAs. The thickness of the GaInAs SQW was varied from 14.5Å to 130.5Å. Both of GaInAs and AlInAs were not intentionally doped. Each SQW was pumped at a wavelength of 5145Å (hbar ω_e=2.41eV) with a low power density excitation fixed at about 10W/cm^2. The sample was suspended in a gas transfer liquid helium cryostat which kept the sample temperature (T_L) at 3.5K . The PL spectra was measured by a double dispersive spectrometer. The signal was detected by Ge and S-1 photodetectors.

Four typical PL spectra from well GaInAs for different well size are displayed in Fig.(3-3-1) as circles. The emission peak energy increases with decrease of well width L_z due to carrier confinement and the emission extends to much higher energies than their bulk counterpart. More important feature is the extent of high-energy tail increases as well width decreases. For example, at L_z =14.5Å

and 130.5Å, the high energy tails above half maximum of luminescence extend to 39meV and 25meV, respectively. This implies that the fractional number of energetic electrons in the n=1 subband of the SQW is increased as well width decreases. The emission from n=1 electron to n=1 light-hole transition is not visible because of low carrier temperature (see determination of carrier temperature below).

An important question should be addressed here is whether or not this broad high-energy tail could be explained only by well width fluctuations. The mechanisms of the broading the full line-width at half-maximum (FWHM) of the luminescence from SQW's have been discussed by Welch et al..[12] It was found that the dominant PL spectra broading was primarily due to a transfer of electrons from AlInAs into GaInAs. The broad FWHM of the spectra could not interpreted only by well width fluctuations even under the worst case of well width fluctuations. For the present investigation, we focus on the spectral characteristics of high-energy tail where the emission intensity decreases exponentially with photon energy to explain the broadening of the high-energy tails. It is well known that inhomogeneous broadening resulting from well-width fluctuations within a well can be quite large in thin well and the fact that the high energy tail decreases exponentially is not sufficient evidence for assignment of a hot electron temperature which differs from lattice temperature. We must deconvolve the broadening out of the high energy tail before deducing electron temperature from it. The strategy for this purpose is illustrated in following section.

For an ultrathin SQW, the FWHM of its PL spectrum is dominated by well-width fluctuations. We can fit (See next paragraph for discussion on fitting)

the line-shape of the luminescence spectrum of the 14.5Å-well to obtain a maximum extent for well-width fluctuations as if the electron system were in equilibrium with the lattice. Since the interfacial quality of the structures are independent of well width, we can calculate the line shapes of PL spectra for the thicker wells using the maximum extent of well-width fluctuations with assumption that the electron temperatures are same as the lattice temperature. The calculated results are shown in Fig.(3-3-1a) to (3-3-1d) as dotted curves for various well-widths. It is clearly demonstrated that the change in the high energy tail with change in the well-width is only a partial result of the increased inhomogeneous broadening as well-width decreases. Therefore, an illusive explanation of high energy tail broadening entirely by well-width fluctuation is ruled out. Introducing a hot electron temperature to explain the broadening of high energy tail is numerically justified.

The theoretical calculation of PL spectra is outlined below. The probability density function for a random variable (r.v.) L_z in "large-island approximation"[13] is assumed to have a Gaussian shape given by:

$$f(L_z) = \frac{1}{\sigma\sqrt{2\pi}} exp\left[-(L_z - L_{z0}^2) / 2\sigma^2\right] , \qquad (3\text{-}3\text{-}1)$$

where L_{z0} and σ^2 are the mean well-width and the variance of r.v. L_z, respectively. The statistics of r.v. L_z is then characterized by its variance σ^2 and independent of mean L_{z0}. Two Gaussian shapes are depicted in Fig.(3-3-2). The dotted curve with obtained maximum extent σ=1.2Å gives a value of 2.8Å for FWHM of the curve, while solid curve corresponds σ=1Å having FWHM=2.4Å .The electrons and holes within the well will experience the well-width

fluctuations resulting in fluctuation of their confinement energies. The effective energy gap is defined as:

$$E_{ge} = E_{1e} + E_{1h} + E_{gw}, \tag{3-3-2}$$

where, E_{1e} and E_{1h} denote the lowest energy edges of electron and hole subbands, and E_g is the band gap of well material (GaInAs). For a finite SQW, E_{1e} can be expressed by:

$$E_{1e} = E_o (L_{zo} / L_z)^{\alpha}, \tag{3-3-3}$$

with

$$E_o = \frac{h^2}{8mL_{zo}^{\alpha}}, \tag{3-3-4}$$

where m is the electron effective mass and α can be determined from an exact equation given in Ref.14. Using a standard method[15] of transformation of a r.v., the probability density function of r.v. E_{ge} with neglect of E_{1h} fluctuation and excitonic effect[16] were found to be:[17]

$$f(E_{ge}) = g(E_{ge}) \exp\left(-(\eta/2)[(E_o/(E_{ge} - E_g - E_{1h}))^{\frac{1}{\alpha}} - 1]^2\right), \tag{3-3-5}$$

with

$$g(E_{ge}) = \sqrt{(\eta/2\pi)} \frac{E_o^{1/\alpha}}{\alpha (E_{ge} - E_g - E_{1h})^{\frac{1+\alpha}{\alpha}}}, \tag{3-3-6}$$

where $\eta=(L_{Z0}/\sigma)^2$. This expression gives PL spectrum as if all the carriers were located at random moving subband edges.

Under condition that well-width is certain the intrinsic PL spectra arise from recombination of thermalized electrons and holes within subbands were calculated using allowed density of states (D) and Fermi-Dirac distributions (f_e and f_h). This is given by:

$$PL^{(intri)} \sim D_e f_e D_h f_h \tag{3-3-7}$$

with

$$D_i = \frac{Am_i}{\pi\hbar^2}, \tag{3-3-8}$$

and

$$f_i = \frac{1}{1+exp[(\epsilon_i-\epsilon_{fi})/kT_c]}, \tag{3-3-9}$$

where ϵ_i and ϵ_{fi} are the kinetic energy and quasi-Fermi energy measured from the subband edge, i=e,h denote the electron and the hole. In our calculation, momentum conservation and energy dependent electron effective mass in the manner given in Ref.18 were considered.

The exact PL spectra can be calculated by taking into account both well-width fluctuations and hot electron temperatures using the following convolution expression:

$$PL^{(exact)}(E)=\int_{-\infty}^{E} PL^{(intr)}(\quad) \quad (\quad)dF_{ge}. \qquad (3\text{-}3\text{-}10)$$

The calculated results for 14.5Å and 33.8Å using σ=1Å are shown in Fig.(3-3-1a) to (3-3-1b) as solid curves. The values of 120K and 105K for electron temperatures for the two wells were obtained.

The main conclusions from such a fitting process are summerized as follows:

(i) Using σ=1Å the high energy tails of PL spectra from various well-widths can be fitted with various electron temperatures which differs from the lattice temperature T_L.

(ii) For $L_z > 40$Å, the high energy tail can be fitted only using Eq.(3-3-7). The fitting using Eq.(3-3-10) just adds some fine structures[19] on high energy tails. But the envelope of high energy tails remain unchanged. Two solid curves for 58Å-well and 130.5Å-well were calculated using Eq.(3-3-7). The electron temperatures were determined 95K and 85K respectively.

(iii) It was found that $kT_c/\epsilon_{fh} \approx 0.69$ and $\epsilon_{fe} \sim 5meV$ lead to the best fits of the measured spectra. The values of ϵ_{fe} deduced from spectra are related to the excess carrier density. For example, ϵ_{fe}=10.6meV for 130.5Å well corresponds a sheet carrier density n_s of 2.2×10^{11} cm^{-2}.

(iv) Another observation from Fig.(3-3-1) is that the widths of the low energy side of emission peaks are about same (60meV) for all the well investigated. This confirms those emissions are extrinsic. They either arise from phonon-assisted recombinations or deep impurities. In general, it is much complicated to

analysis. Therefore, no attempts were made to fit those emissions in this paper.

The experimental data of T_c versus L_z extracted from PL spectra of SWQ's are plotted by the dots in Fig.(3-2-3). There are two salient features. First, electrons in a deep SQW are much hotter than their bulk counterpart under the same excitation conditions.[20] This hot feature is due to the high density in the well via the trapping of the carriers from the barriers. The relatively large amount of electrons have to be distributed in high energy tail in order to form a steady state distribution because the allowed density of states is independent of energy within one subband for 2D electron system. Second, the electron temperature increases as well width becomes smaller. This dependence arises from the increase in power transfer from photogenerated energetic electrons to thermalized electrons,[9] which is also due to the increasing thermalized electron density in the well as L_z decreases.

The steady state variation T_c with L_z shown in Fig.(3-2-3) discussed above is further quantitatively explained using the following model. Under steady state condition the electron temperature T_c is determined by the balance between the rate at which the electron gas receives energy from the photogenerated electron and the rate at which the electron gas loses energy to the lattice. The excitation laser beam with photon energy $h\omega_e$ creates excess energetic electrons (N_{ex}) into the conduction band of the SQW. It is those electrons via drift and diffusion that are effectively trapped into the SQW and thermalized among themselves at T_c via electron-electron collision. It should be noted that a substantial electron population may exist at high T_L as a result of transfer from unintentionally doped AlInAs even without photopumping. However, at very low T_c, deep impurities can not totally ionized. This is convinced by the relative PL intensity variation with T_L

between well and barriers.[14]

The power per electron given to the thermalized electrons from photogenerated energetic electrons is given by[9]

$$P_e = P_a (E_k/\hbar\omega_e) f (1/ C_{tr} N_{ex}) \quad (3\text{-}3\text{-}11)$$

where f is the fraction of absorbed laser power (P_a) by the sample given to the thermalized electron system by the energetic electrons ; A $\sim 4\text{x}10^{-4}$ cm^2 is the laser beam area at the sample; E_k is the average excess energy per electron and the factor E_k / *hbar* ω_e is about 0.3; and C_{tr} is a phenomenological factor that takes trapping process into account. The value of f is given by $f = n_w/(n_w + n_c^*)$, where $n_c^* \sim 5\text{x}10^{17}$ cm^{-3} is the density of thermalized electrons at which the photogenerated energetic electrons lose the same amount of power as directly to the lattice by emission of the energetic LO-phonons. The $n_w = C_{tr} N_{ex} / AL_z$ is the thermalized electron gas density in the well. The fractional number f can be rewritten as follows

$$f = 1/ (1+L_z/4L_c) \quad (3\text{-}3\text{-}12)$$

by defining a characteristic length $L_c = C_{tr} N_{ex} / (4A n_c^*)$. Since the well width L_z is much less than absorption length (L_a) which is about 1um for both GaInAs and AlInAs, P_a and E_k can be treated as constants. Tha factor C_{tr} is inversely proportional to the average trapping time τ_{tr} which may be expressed by[21] $\tau_{tr} = (L_a - L_z)/ v_d \sim L_a / v_d$ for $L_a \gg L_z$, where v_d is an average drift velocity. The v_d may be very close to the maximum value of 10^7cm/s (1um/10ps) due to large well depth[14] for our samples. Therefore, the total number $C_{tr} N_{ex}$ of electrons that are transferred from the AlInAs can be also assumed as a constant.[12]

The photogenerated carrier density is estimated to be about 1.1×10^{15} cm^{-3}. This yields a value of $L_c = 11\text{Å}$. Therefore, from Eq.(3-3-12), the narrower well width, the more efficient is the energy transfer from energetic electrons to the thermalized electrons.

When the energy loss of thermalized electrons in the SQW is dominated by the polar LO-phonons, the average power per electron transferred from electrons in the SQW to the lattice is given by [9,22]

$$P_L = \frac{E_{LO}}{\tau_{avg}} exp\,[-E_{LO}/k_B T_c(L_z)], \tag{3-3-13}$$

where E_{LO}=32meV is the LO-phonon energy. The value of $E_{LO}\ exp\,[-E_{LO}/k_B T_c(L_z)]$ is the average energy loss per hot-electron. The exponential factor is the fractional number of the thermalized electrons in the SQW that can emit LO-phonons, and τ_{avg} is the average phonon emission time (averaged over a given Fermi-Dirac distribution). Under steady state equilibrium condition, the electron temperature T_c can be determined from $P_e(L_z) = P_L(T_c)$, that is

$$T_c = E_{LO}/k_B ln\,[g\,(1+L_z/4L_c)], \tag{3-3-14}$$

where the factor g is given by

$$g = (C_{tr} N_{ex} / 0.3 P_a)(E_{LO}/\tau_{avg}). \tag{3-3-15}$$

The value of g=20 is obtained by the least square fit of the experimental data given in Fig.(3-2-3). The calculated variation of T_c with L_z given by Eq.(3-3-14) is plotted in Fig.(3-2-3) as a solid curve(a). It should be emphasized that the data

were taken under the fixed excitation power since T_c depends on the excitation as shown in Ref.14. The excellent fit of Eq.(3-3-14) to the steady state electron temperature data extracted from high-energy tails of the PL spectra implies three important conclusions. First, the electron and polar LO-phonon scattering dominates the excess energy loss of the thermalized electrons in the SQW's. Second, since the fractional number f given in Eq.(3-3-12) increases by the same amount as the exponential factor given in Eq.(3-3-13) does when L_z decreases from 130.5Å to 14.5Å, the e-p scattering rate ($R_{2D}=1/\tau_{avg}$) in SQW is independent of the well width L_z within our experimental accuracy, indicating that the influence of reduced dimensionality does not play an important role in carrier-energy-loss rates. This is in contrast to the theories of Ridley[2] and Leburton[3] (See next section for details). Third, because the excess carriers trapped into the well are proportional to the power absorbed by the sample, the value of g given in Eq.(3-3-15) is inversely proportional to the time constant τ_{avg} for the hot-electron relaxation through phonon emission. This enables us to estimate τ_{avg}. Since P_a is about 4mW, a value for the e-p scattering time τ_{avg} of about 18ps is calculated from Eq.(3-3-15). This is comparable to the time determined by Ryan et al.[6] The τ_{avg} in the SQW's is about a factor of 4 longer than its bulk counterpart[10] within the carrier density range from $n_w \sim 1.7\times10^{17}$ cm^{-3} to 1.5×10^{18} cm^{-3}. Shah et al.[7] and others[5,6] have also observed further slower electron-energy relaxation in (AlGa)As/GaAs s[illegible]n. Shah et al.[7] concluded that nonequilibrium optical phonon effects was the primary cause for the low electron-energy-loss rate. The hot-phonon effect may explain our experimental results. However, how to establish this nonequilibrium population when τ_{avg} is comparable or longer than phonon lifetime τ_p is still not clear.

From the theoretical studies given by Hess[1], Ridley[2], and Leburton[3] as well as ourselves, the e-p scattering rate R_{2D} should be dependent on L_z and somewhat enhanced as L_z decreases within one-subband approximation. This implies the electron temperature T_c would increases slowly or even decreases as L_z becomes smaller. When the approximate analytic results for the R_{2D} at the onset of phonon emission (not averaged over the Fermi-Dirac distribution) calculated by Ridley[2] and Leburton[3] are used in deriving Eq.(3-3-14), T_c are given by the following:

$$T_c = E_{LO}/k_B \ln[(1+L_z/4L_c)130.5/L_z] \qquad (3\text{-}3\text{-}16)$$

and

$$T_c = E_{LO}/k_B \ln[(1+L_z/4L_c)/1.63(1+L_z/4L_o)] \qquad (3\text{-}3\text{-}17)$$

respectively, where $L_o = h/(2mE_{LO})^{1/2}$. The calculated variation of T_c with L_z given in Eq.(3-3-16) (Ridley) and Eq.(3-3-17) (Leburton) are also plotted in Fig.(3-3-3) as dash curves (b) and (c). A forced fit at the data point (130.5Å ,85K) has taken into account in both Eq.(3-3-16) and Eq.(3-3-17). These curves do not fit the data well. However, Leburton's model shows a similar trend for the variation of T_c with L_z, indicating that the phonons that interact with confined electrons do not behave much differently from those of the bulk. The dash curve (c) clearly demonstrates that the MCA fails for the polar LO-phonon intra-subband scattering in thin quantum wells. However, the disrepancy is partially due to the other crude approximation we used. Using the results on electron-phonon scattering rate from our more exact calculation as presented in the previous section, a more close agreement with the experimentally determined carrier temperature variation with L_z can be obtained because the scattering rate calculated by us has a

weaker L_z dependence than that by Ridley.[3]

3.4 Summary

In summary, the effects of carrier confinement and finite well thickness on the phonon emission rate of the electron in Quasi-2D structures through the unscreened electron-POP interaction are shown by taking into account the non-commutation relationship between the Hamiltonian of the system and the electron momentum operator in the z-direction. It is explicitly demonstrated how one can exactly treat the fuzzy momentum conservation in z-direction using neither "non-momentum-selection rule" nor "momentum conservation approximation" by considering the phonon wavevector q_z as a r.v.. The phonon emission rate at the onset is shown to be 3 times smaller than previously reported and has a weaker L_z dependence. The electron-phonon scattering rate in quasi-2D system increases with initial electron energy. This behavior distinguish all previous works[1-3] and is more like 3D system except that there is a finite value of the rate at the emission onset due to the finite electron density of states.

The temperature of electrons confined in the SQW's has been determined from high energy tails of PL spectra of a set of undoped SQW's. The high electron temperature in the SQW's is attributed to the high carrier density and slow hot-electron relaxation. The observed variation of the steady state electron temperature with L_z indicates that the phonon scattering rate for electrons confined in SQW's does not strongly depend on the well width L_z within our experimental accuracy.

Reference

1. K. Hess, Appl. Phys. Lett. 35, 484(1979).

2. B. K. Ridley, J. Phys. C 15, 5899(1982), and F. A. Riddoch and B. K. Ridley, J. Phys. C 16, 6771(1983).

3. J. P. Leburton, J. Appl. Phys.56, 2850(1984).

4. P. J. Price, Ann. Phys. 133, 217(1981).

5. Z. Y. Xu and C. L. Tang, Appl. Phys. Lett. 44, 692-694 (1984).

6. J. P. Ryan, R. A. Taylor, A. J. Turberfield, Angela Maciel, J. M. Worlock, A. C. Gossard and W. Wiegmann, Phys. Rev. Lett. 53, 1841-1844 (1984).

7. J. Shah, A. Pinczuk, A. C. Gossard, and W. Wiegmann, Phys. Rev. Lett. 54,2045-2053 (1985).

8. The material parameter used for GaAs are $m=0.067m_0$, $\bar{\epsilon}=70$ and $h\omega_0=36.8meV$.

9. J. Shah and R. C. C. Leite, Phys. Rev. Lett. 22, 1304-1307 (1969).

10. K. Kash and J. Shah, Appl. Phys. Lett. 45, 401-403 (1984).

11. D. F. Welch, G. W. Wicks and L. F. Eastman, Appl. Phys. Lett. 43, 762-764 (1983).

12. D. F. Welch, G. W. Wicks, and L. F. Eastman, Appl. Phys. Lett. 46, 991-993 (1985).

13. R. Dingle, A. C. Gassard, and W. Wiegmann, Solid State Comm. 38, 709-712 (1981).

14. K. Shum, P. P. Ho, R. R. Alfano, D. F. Welch, G. W. Wicks, and L. F. Eastman, Phys. Rev. B 32, 3806-3810 (1985).

15. "Probability, random variables, and random signal principles" Peyton Z. Peebes Jr., McGRAW-Hill book company, p.67 (1980).

16. J. Sing, K. K. Bajaj, and S. Chaudhuri, Appl. Phys. Lett. 44, 805-807 (1984).

17. Another term with "+" sign in [ ] was neglected.

18. S. Chaudhuri and K. K. Bajaj, Phys. Rev. B 29, 1803-1806(1984).

19. B. Deveaud, A. Regreny, J-Y. Emery, and A. chomette, J. Appl. Phys. 59, 1633-1640(1986).

20. A. F. S. Penna, J. Shah, T. Y. Chang, M. S. Burroughs, R. E. Nahory, M. Tamargo, M. M. Cox, Solid State Comm. 51,425-428 (1984). The spectrum which was taken from the sample MBE(20324) could be fitted to $E^2 exp(-E / kT_c)$ yielding a value of electron temperature of about 15K. Their excitation density power was about $10W/cm^2$ and the sample temperature was kept at about 2K.

21. E. O. Gobel, H. Jung, J. Kuhl, and K. Ploog, Phys. Rev. Lett. 51, 1588-1591 (1983).

22. D. Von der Linde and R. Lambrich, Phys. Rev. Lett. 16, 1090-1093 (1979).

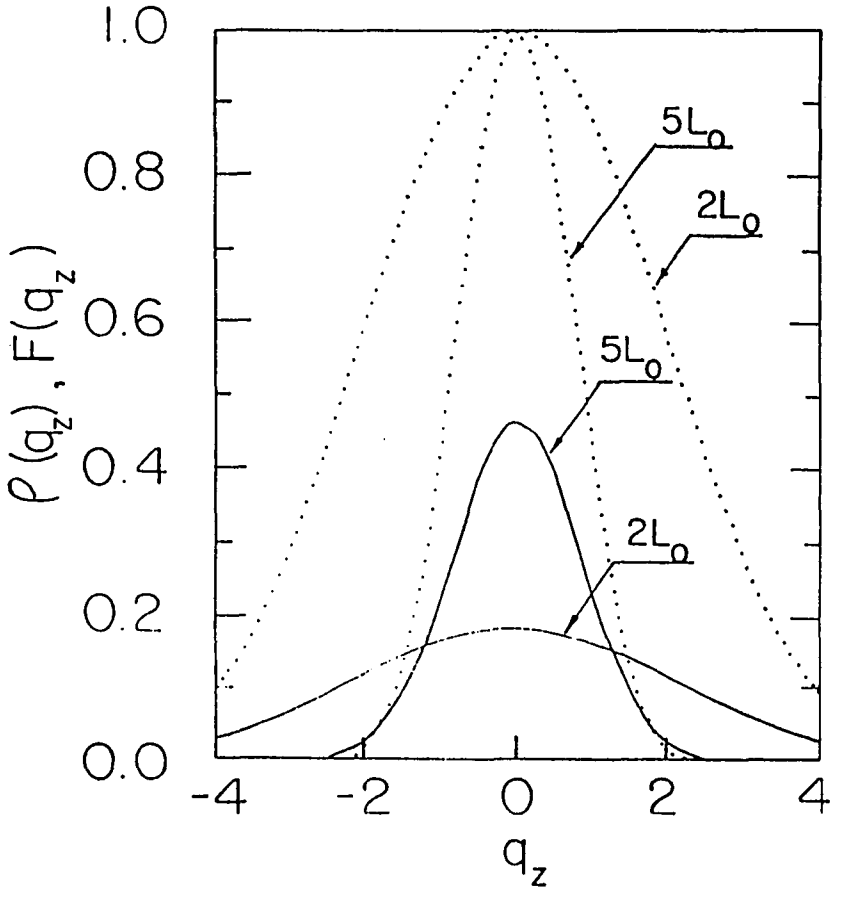

Fig.(3-2-1) The solid curves are for the probability density functions for r.v. q_z . The dotted curves are for the magnitudes of the form factor in z-direction $F(q_z, L_z)$. The well width are indicated on the curves.

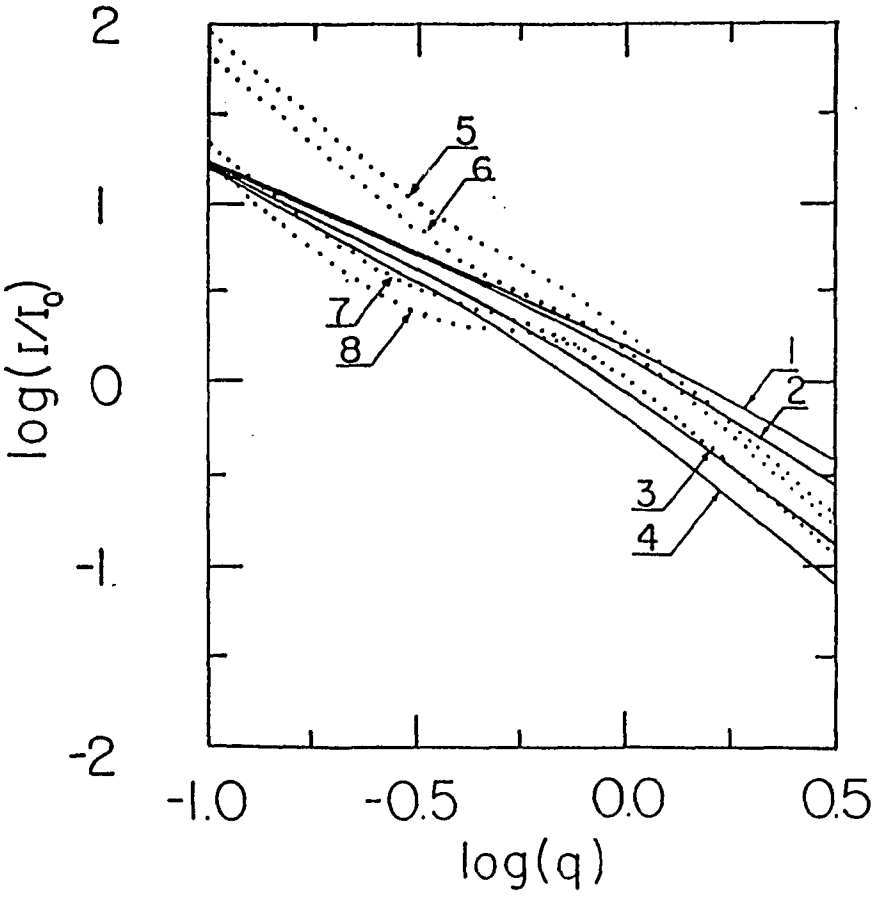

Fig.(3-2-2) The electron-POP interaction strength for Q2D and 3D systems versus the parallel component of phonon wave vector $\vec{q}$. The solid curve from 1 to 4 are for the Q2D structures with well width $0.5L_0$, L_0,$3L_0$ and $5L_0$ accordingly. The main contribution of the integral $I^{Q\,2D}$ to the total phonon emission rate occurs at q=1, where $I^{Q\,2D}$ presents a weak L_z dependence. The dotted curves from 5 to 7 are for the 3D system with ratio r=10, 3 and 1.2, respectively. The scattering angle θ for those three curves are set to be all zero. The dotted curve 8 is also for 3D system with r=1.2 and $\theta=\pi/6$. The larger scattering angle θ, the larger the value of I^{3D} in the range from 0.1 to 1 for q.

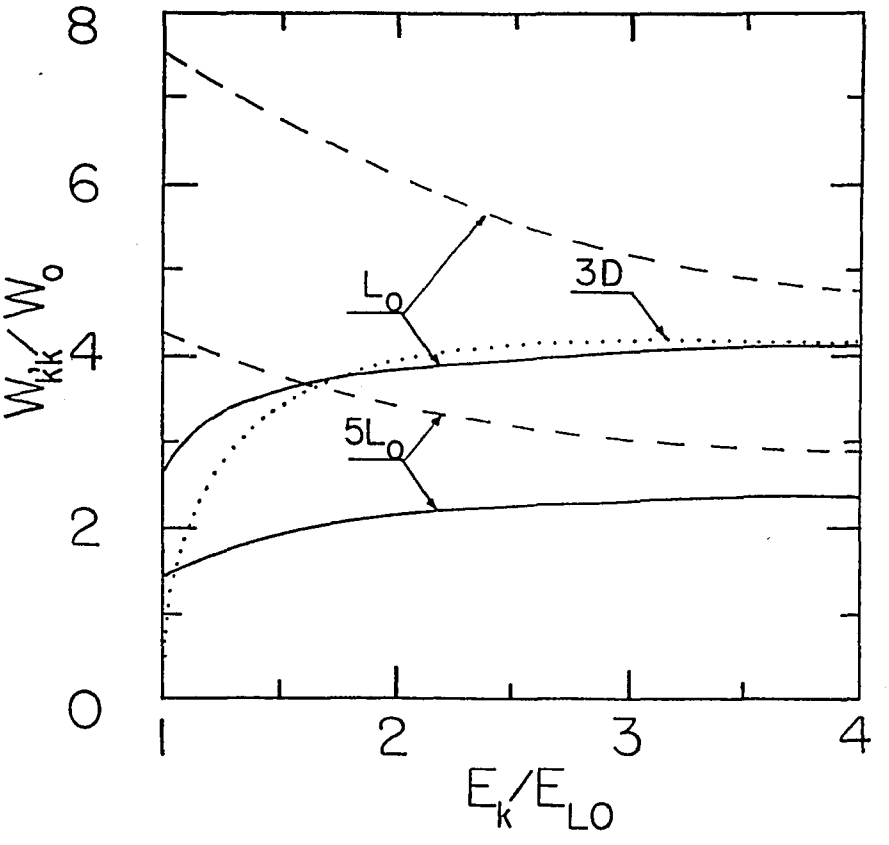

Fig.(3-2-3) The normalized phonon emission rates as function of E_k / $\hbar\omega_0$ in semiconductor structures at 0 K lattice temperature. The solid curves are from this work and the dash curves were generated from Leburton's result.[4] The well thicknesses are indicated on the curves. The dotted curve is 3D result.

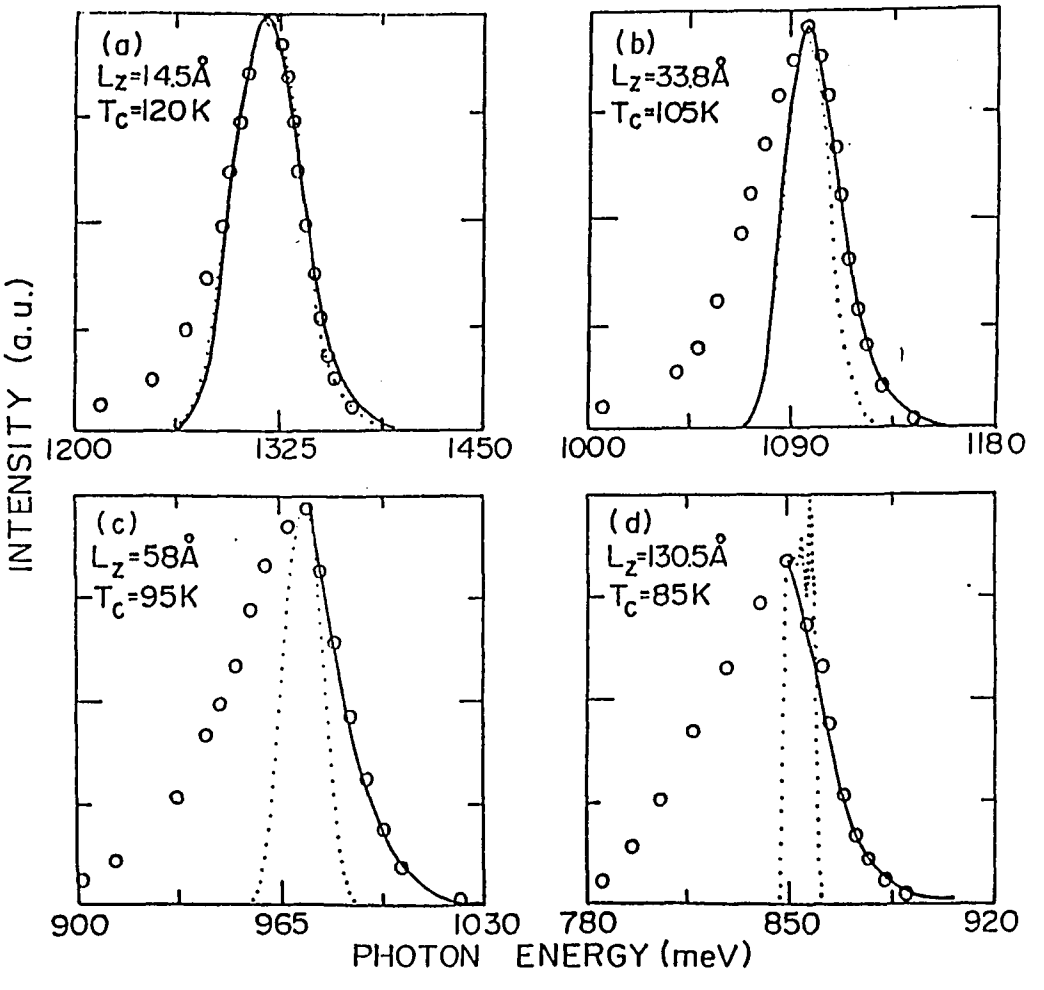

Fig.(3-3-1) The PL spectra (circles) from the SQW's of various well-widths with excitation power density about 10W/cm^2 at lattice temperature T_c=3.5K. The dotted lines are the theoretical fits using the maximum extent of well-width fluctuations (σ=1.2Å) with assumption that carrier temperatures are same as lattice temperature. The solid lines in a. and b. are the

exact fits using convolution expression Eq.3-3-10 with σ=1Å and various electron temperatures displayed in the figure. The solid lines in c. and d. are the high-energy-tail fits using Eq.3-3-7. The edges of dotted lines in low energy sides marks the boundary between extrinsic and intrinsic emissions.

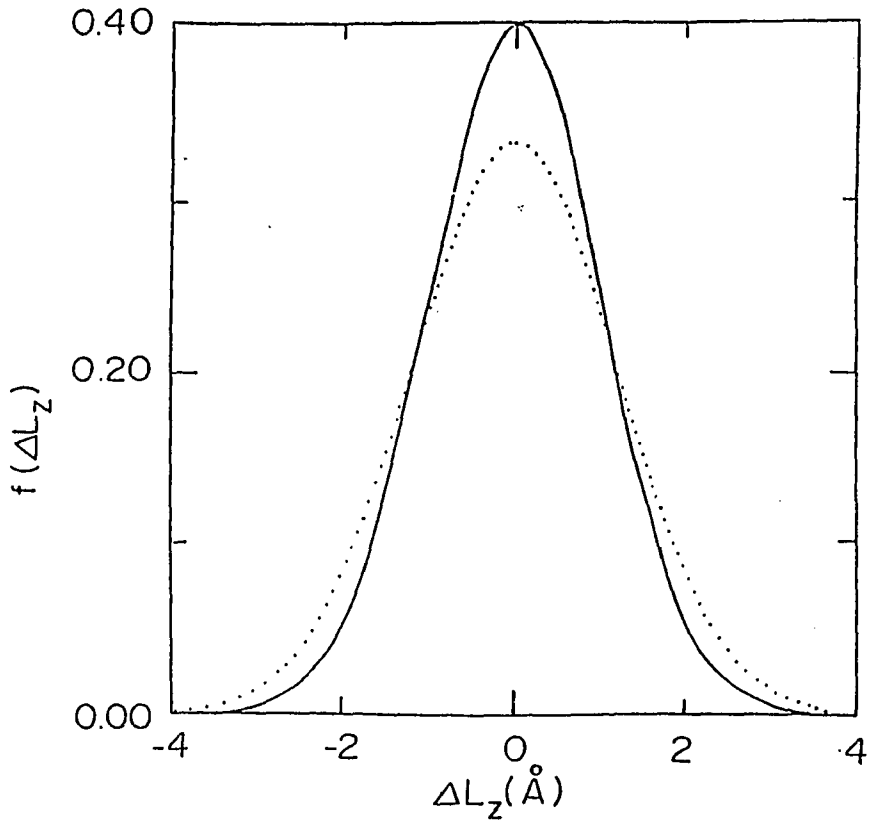

Fig.(3-3-2) Probability density functions versus well-width change ΔL_z with σ=1Å for solid curve and σ=1.2Å for dotted curve respectively.

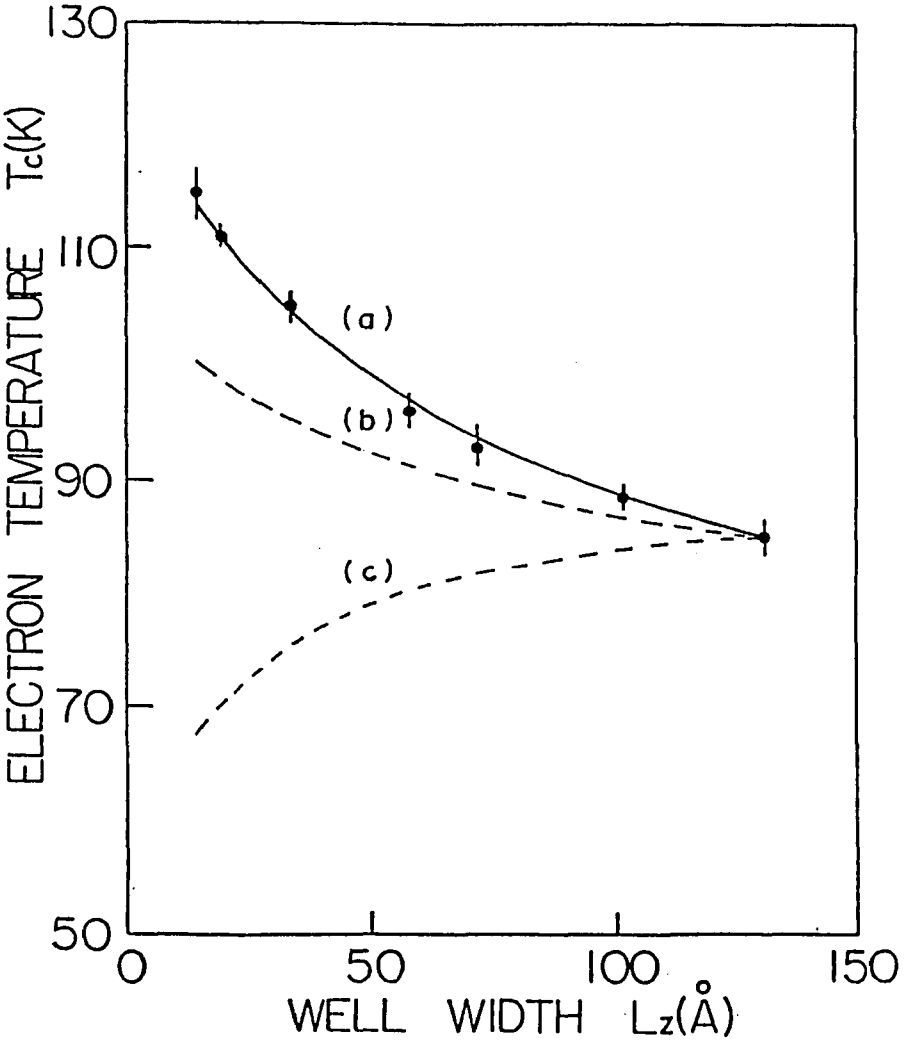

Fig.(3-3-3) Electron temperature (T_c) is plotted versus well width L_z at fixed power density excitation of about 10W/cm^2. The solid curve (a) is a plot of the Eq.(3-3-14). The dash curves (b) and (c) are the plots of the Eq.(3-3-16) (Ridley) and the Eq.(3-3-17) (Leburton), respectively.

Chapter 4

Nonequilibrium phonon effects on the energy relaxation and lifetime of photogenerated carriers in undoped GaAs quantum wells

4.1 Introduction

Recently, there have been growing interest in microstructures from both a device as well as a physics point of view to understand the fundamental interactions of free and confined electrons and holes with phonons. This understanding is crucial for the operation of ultrahigh speed devices based on the principles of ultrafast carrier dynamics. The slowing of carrier cooling in bulk semiconductor was attributed to the screening[1] of electron-phonon interaction or re-heating of carriers by hot-phonons.[2,3] The first comparison[4] of the hot-electron cooling rates in undoped multiple quantum well (MQW) structures and in the bulk GaAs done by time-resolved measurements of optical absorption and gain. The cooling rates were approximately same for the bulk and the MQW at a carrier density of 2.5×10^{17} cm^{-3}. This is expected from a simple theory[5] where the lattice is treated as a heat bath for the quasi-equilibrium carriers. Quasi-steady-state experiments have been carried out from two groups[6,7] to investigate the interaction of electrons and holes with phonons in modulation-doped MQW structures. These experiments have

generated conflicting results regarding the presence[6] or absence[7] of nonequilibrium phonons. The time-resolved photoluminescence measurements from modulation doped semiconductor MQW with more than 20ps time resolution were reported by Ryan *et al.*[8] who found that the cooling of hot carriers was anomalously slow after 40ps.

By reviewing these and other previous works we noticed two important points. First, one can not extract information on the initial carrier relaxation process from both quasi-steady-state experiments and time-resolved measurements with time resolution greater than 10ps. To assess the importance of non-equilibrium phonon effect on the energy relaxation of hot carrier one use a corresponding theory to match the experimental carrier temperature cooling curve or the logarithm of power loss as function of the inverse of the carrier temperature. There has been no report on the direct evidence for existence of non-equilibrium phonons in quantum well structures under high excitation. It is necessary to study the initial carrier relaxation process for substantiating the existence of nonequilibrium phonons and its importance to the hot-carrier relaxation since phonon lifetime is about 5-7ps. Second, one can not easily obtain information on photoinjected carrier lifetime because the large doped-in carrier density in modulation doped MQW structures is comparable to the photoexcited carrier density. In these experiments the carrier lifetime is essentially close to the value in bulk which is about 1ns.[8] Therefore, it is necessary to study photoinjected carrier dynamics in undoped MQW structures in order to obtain both information on the energy loss rates and on the carrier lifetime. The electron-hole pairs generated by the photoexcitation by femtosecond laser pulses thermalize via carrier-carrier

interaction to reach a quasi-equilibrium state in less than 1ps. Simultaneously, three other processes take place. The first is the loss of energy of the electron-hole system through the electron-phonon interaction. The second process is the carrier diffusion process due to the gradient of carrier density between photoexcited and non-excited areas. The third process is recombination of electron-hole pair through both nonradiative and radiative mechanisms. The work reported here on photoluminescence experiments uses the last process to probe the first process. The investigation on dynamic process of photogenerated carriers in this sample is described elsewhere.[9]

In this chapter, the experimental observations are reported from the measurements of time-resolved photoluminescence with 2ps time resolution as well as the studies of integrated luminescence spectra from an undoped GaAs MQW structure with dependences of lattice temperature, excitation intensity, and polarization. The non-equilibrium phonons emitted by hot electrons are directly observed by measuring the time-integrated as well as time-resolved phonon replica luminescence below n=1 electron to heavy-hole transition energy. Energy relaxation of hot electrons is found to be substantially suppressed due to the existence of a large population of nonequilibrium phonons after an initial rapid cooling. The photoexcited carrier density extracted from fitting of time-resolved photoluminescence profiles at various emitted photon energies decreases non-exponentially and very rapidly within the first 30ps. An effective carrier depletion time is determined to be as short as 10ps. The mechanism leading to such short carrier lifetime is associated with nonequilibrium phonon enhanced phonon-replica-emission.

4.2 Multiquantum Well Structure

The undoped GaAs/$Al_xGa_{1-x}As$ symmetric MQW structure investigated were grown by molecular-beam epitaxy on a (001)-oriented undoped GaAs substrate. The MQW consists of 50 periods of 55Å thick GaAs and 100Å thick $Al_{0.3}Ga_{0.7}As$ layers and followed by a 1.2*um* GaAs buffer layer. The lateral size of the structure is 2×4*mm*. The samples was mounted on the cold finger in an optical helium cryostat.

Using a finite-depth square well model and material parameters given in Ref.10 the subband energy positions in the wells were calculated. There are two subbands for electron (e) and heavy-hole (hh) and only one subband for light-hole (lh). The good quality of samples is confirmed by well resolved heavy-hole and light-hole excitonic structures at room temperature as shown in Fig.(4-3-1). The HWHM for the heavy-hole excitons is about 5.5meV.

4.3 Experimental Method

An ultrashort light pulse of 500fs duration at 620nm was used to excite the electron-hole pairs with a carrier density of $\sim 10^{19} cm^{-3}$. This light source was generated from a colliding-pulse passive mode-locked dye laser and amplified by a four-stage dye amplifier pumped with a frequency doubled Nd: YAG laser at 20Hz. A block diagram of this laser system is shown in Fig.(4-3-1). The photoluminescence was spectrally filtered using various narrow band filters, and temporally

dispersed by a 2ps time resolution Hamamatsu streak camera system. The luminescence intensities were corrected for the nonlinearity of streak rate, the spectral response, and the transmission of each narrow band. The time resolution for the present work is about 2ps.[11] The experimental apparatus used in this research is shown in Fig.(4-3-2).

4.4 Results and Discussion

4.4.1 Steady State Studies

Time-integrated luminescence spectra the symmetric MQW structure excited by the subpicosecond laser pulse at various lattice temperatures (T_L) are shown in Fig.(4-4-1a). These spectra were taken in conventional Raman $z(y,y)\bar{z}$ configuration, where z is the growth direction. In order to eliminate radiation from the edges of the sample the luminescence spot was imaged on an aperture with aid of a streak camera and then focused onto a vertical slit of a grating spectrometer. Several features are displayed in the data shown in Fig.(4-4-1a). (1) The emission peak (A) on high energy side of the spectra is from the recombination of photogenerated n=1 electrons and n=1 heavy-holes. This peak shifts towards the low energy side as T_L increases. An high energy tail on the main peak (A) develops with increase of T_L. For $T_L > 150K$, the shoulder on high energy side of the A-peak arising from the recombination of n=1 electrons and n=1 light-holes can be identifyed.

(2) A broad emission band (C) at low energy side of the spectra arises from

1.2*um* GaAs buffer layer. The total emission intensity decreases as T_L increases.

(3) The most interesting feature of the spectral data is the appearance of an emission band (B) ~30meV below the n=1 electron to n=1 heavy-hole transition. This B emission band is attributed to the nonequilibrium phonon enhanced phonon-replica. The following reasons support this assignment to the B band:

(i) This B emission band does not appear in the steady-state photoluminescence spectra taken at low power excitation about $1W/cm^2$ at 4.3K using a 488nm line of an argon-ion laser. However, the photoluminescence spectra using the weak train of laser pulses (120fs) directly from the colliding-pulse passive mode-locked dye laser as the excitation source, with an excitation power density in range of 10^{-5}—$10^{-3}W / cm^2$, shows a weak electron to acceptor emission band separated by 17meV from n=1 electron to heavy-hole transition accompanied by its phonon-replica[12] at low temperatures. This extrinsic emission band disappeared completely when the sample temperature was raised to ~80K, whereas the B band displayed in Fig.(4-4-1a) exists up to room temperature. Moreover, the relative time-integrated intensity between B and A bands shown in Fig.(4-4-1a) which is detected under amplified 500fs light pulse excitation decreases as the excitation power density decreases. The B band is not visible when the excitation power density is lower than $10^{-3}P_m$, where $P_m \sim 10^{12}W / cm^2$ is the maximum value of the excitation power density. This contradicts what is generally expected for impurity emission. Since the concentration of acceptors is low in our sample as confirmed by the luminescence studies using the weak train of 120fs light pulses, the impurity emission should be more readily apparent and pronounced at lower excitation. Therefore, the B emission band shown in Fig.(4-4-1a) can not be

attributed to electron to acceptor luminescence under high excitation.

(ii) We have also measured the polarization of the emission bands A, B, and C by adopting a "right-angle"[13,14] integrated luminescence spectra. It was found that the emission band B detected along the y-direction (emitted at the sample edge as shown in the inset of Fig.4-4-1b) was highly polarized in x-direction, while A and C emission bands were depolarized independent of excitation power density and lattice temperature. The intensity ratio between x- and z-direction for B band was about 20 and independent of lattice temperatures from 4.3 to 300K at full excitation power density P_m. The polarization behavior of B band is consistent with the Raman scattering measurements reported by Zucker *et al.*[14] where the initial photons are provided by the external laser source. In our case the initial photons are provided by the luminescence from the recombination of n=1 electrons and n=1 heavy-holes at the subband edges. This process is strongly enhanced by the presence of a large number of nonequilibrium phonons emitted by the hot-electrons at high excitation. But, the polarization ratio strongly depends on the excitation power density at given lattice temperature. For example, at $T_L = 20K$, the ratio decreases from 20 to ~ 6 as the excitation power density decreases from P_m to $0.017P_m$ (2ND13). When lattice temperature is above $100K$, the B band is very weak and shows no difference in luminescence intensity between two polarizations at $0.017P_m$ as displayed in Fig.4-4-1b for the case of $T_L = 100K$, while the ratio remain 20 at full excitation P_m. The depolarized feature of emission band C is expected since the emission is from 1.2*um* GaAs buffer layer. This in fact provides a good check of our system. However, the polarization behavior of the emission band A is not understood. In terms of the

selection rule of dipole recombination described by Iwamnra *et al.*[15], the emission intensity for x-polarization (TE polarization) should be at least four times higher than that for z-polarization (TM polarization) due to different density of states for heavy-hole and light-hole.

(iii) The ratio of emission intensity between B and A emission bands increases at lattice temperature increases. The value of the ratio as function of temperature are shown in Fig.(4-4-2) as solid triangles. This behavior is remarkablely different from the conventional stimulated emission process in which phonons do not participate. As in semiconductor lasers, the stimulated emission is less effective when the sample is at room temperature. To convince the emission band B arises from phonon-assisted process, we calculate the sum of occupation numbers for both equilibrium phonons (lattice temperature T_L) and nonequilibrium phonons (carrier temperature T_c) by assuming the carrier temperature is same as the effective temperature for the nonequilibrium phonons after 30ps (see later discussion on the carrier temperature). The calculated result is shown by the solid line in Fig.(4-4-2). The fitting of the total phonon occupation number to the obtained intensity ratio from the spectra is impressively good. This implies that the intensity of peak B is well correlated with the LO-phonon population. Because of participation of non-equilibrium phonon the intensity of the B band (see also time-resolved luminescence at 780nm in Fig.(4-4-3)) is strongly enhanced especially at low temperatures. This further supports our assignment of the B band to the non-equilibrium phonon enhanced phonon replica.

(iv) It is also not possible to attribute the emission band B to the emission from renormalized band-band transition because the peak position of A band

(766.7nm) and B band as well as the energy separation between between them at 4.3K do not change with variation of excitation intensity by a factor of 10^{-3} (2ND3). A further support to above statement is the fact that the spectral position of peak-A exactly coincides with each other for two different luminescence studies using different light excitation sources: one is the weak 120fs-pulse train with a repetition rate of 125MHz, and the other is the amplified 0.5ps-pulse with a 20Hz repetition rate.

Over years, there has been much debate[15-17] on the interpretation of the spectral features locate below the n=1 electron to heavy-hole transition energy. This is because many species can exist in this energy region: impurity states, longitudinal optical phonon (LO)-phonon replica, and intrinsic band gap-renormalization due to many body interactions. Holonyak and co-workers[18] have demonstrated the LO-phonon participation in GaAs-AlGaAs based QW laser emission by the observation of more than one LO-phonon sidebands of laser operation below the n=1 confined-particle transition. The phonon replica of n=1 electron to heavy-hole luminescence also occur in the InGaAs based systems. The observation of coupling at both the GaAs- and InAs-like bulk LO-phonon energies of InGaAs QW by Skolnick *et al.*[18] has confirmed that the peak below the n=1 electron-heavy-hole transition is phonon replica. It should be pointed out that our assignment of the B emission band to phonon replica of n=1 electron-heavy-hole transition is consistent with the time-resolved photoluminescence data described in next section.

4.4.2 Time-Resolved

Time-resolved photoluminescence intensities of the symmetric MQW structure at 4.3K are shown in Fig.(4-4-3) for various emitted photon energies. The emission centered at 770nm arise from the recombination of electrons and heavy-holes near the respective first subband-edges. The radiation with wavelengths less than 770nm are from the recombinations of hot carriers. The time-resolved luminescence intensity of the phonon replica is shown in Fig.(4-4-3) by the emission centered at 780nm. Each luminescence profile was the average from 10 individual shots using a prepulse[19] for averaging. The left peak of the dotted curve is the prepulse which reflects the 2ps temporal resolution. The right peak on the same curve is the Rayleigh scattering light from the sample surface which defines the "zero" time for our analysis. Several features appear in the data displayed in Fig.(4-4-3). (i) The rise time for all the luminescence profiles are instrumental; the 2ps up-limit reflects the rapid thermalization and initial cooling. (ii) The shape of rise-part of luminescence profile at 780nm is similar to that at 770nm, but delayed by 3ps. This implies that the emission at 780nm does not originate from the same band as the emission at 770nm; otherwise, the rise-part of the luminescence at 780 should start at the same zero point as that at 770nm. The 3ps delay is consistent with our assignment of the emission band center at 780nm to the stimulated phonon replica band. This 3ps is just the effective time required to establish a large nonequilibrium hot phonon population. (iii) The luminescence decay time of 30ps[20] (broken curve) for the phonon replica emission at 780nm is shorter than the luminescence decay time of 60ps[20] at 770nm. This suggests that the emission at 780nm can not be due to impurity emission at high excitation.

To study the energy relaxation process quantitatively, the carrier

temperature as function of time must be determined. There are many ways to obtain the time evolution of the carrier temperature. One way is to analyze the high energy tail of time-resolved spectra using a Maxwell-Boltzmann or a Fermi distribution.[6-8] Another way is to measure the ratio of luminescence intensity profiles as function of time at two energy positions[1] within exponential energy tail by also assuming a Maxwell-Boltzmann or a Fermi distribution. The above two methods can not extract the information on the photogenerated carrier density. An expression in the time domain is introduced to fit the luminescence profiles in time obtained experimentally by using two adjustable parameters, namely, the carrier density (n_e , n_{hh} , n_{lh}) and the electron temperature (T_c). Assuming the direct optical transitions, the luminescence intensity is given by:

$$I(E_i, t) = C_i(1-e^{-t/\tau_r}) \qquad (4\text{-}4\text{-}1)$$

$$[\,|M_{e-hh}|^2 \rho_e f_e \rho_{hh} f_h + |M_{e-lh}|^2 \rho_e f_e \rho_{lh} f_h\,],$$

where the $\rho_{e,hh,lh} \sim m_{e,hh,lh}$ are the density of state for electron, heavy-hole, and light-hole; the $M_{e-hh(lh)}$ is the matrix element[21] for electron to hh(lh) transition; C_i absorbed all the constant factors including the corrections for detector response and the transmission of each narrow band filters used; τ_r is the rise time of luminescence and is set to be 1ps (approximately the response time of the system) which is an up-limit of thermalization time of electron-hole system;

$$f_{e,h} = \frac{1}{e^{(\epsilon_i - u_{\epsilon,h})/KT_c} + 1} \qquad (4\text{-}4\text{-}2)$$

is the Fermi-Dirac distribution for electrons in conduction band (with subscript e) and for holes in valence band (with subscript h).

The quasi-Fermi energy of holes (u_h) is related to the quasi-Fermi energy for electrons (u_e) and the carrier temperature by the relation of

$$n_e = n_{hh} + n_{lh} \quad . \tag{4-4-3}$$

This value is given by:

$$u_h = KT_c \ln [e^{a \ln (1 + e^{u_e / KT_c})} - 1] \quad , \tag{4-4-4}$$

with

$$a = \frac{m_e}{m_{hh} + m_{lh}} \quad . \tag{4-4-5}$$

An **unique** set parameters of $T_c(t)$ and $u_e(t)$ was used to consistently fit **all** the luminescence profiles detected at different photon energies E_i. Three typical calculated luminescence profiles are shown in Fig.(4-4-3) by the thick solid curves in which one determines experimentally $T_c(t)$ and $n_{e,hh}(t)$.

The **experimentally** determined values of T_c as function of time is plotted as the solid curve in Fig.(4-4-4). The shaded area reflects the extent of the uncertainty in deducing the carrier temperature within the first 4ps due to our limited time resolution. The plot of T_c vs. t is interpreted as follows. Carrier-carrier collisions quickly leads to a thermalized distribution at very high T_c within 1ps due to a large number of hot carriers excited.[22] The initial thermalization process of carriers can only be probed by femtosecond spectroscopy. **The initial cooling of the thermalized distribution is studied with our present time resolution of 2ps, providing information about both the electron-phonon interaction and the carrier dynamics.** The initial cooling within first

5ps is very fast (250K/ps) assuming a Fermi-Dirac distribution for electrons.[5] After the initial cooling, a large number of longitudinal optical phonons in finite wavevector space accumulates due to the finite phonon lifetime[23]. The phonons emitted by the hot electrons are reabsorbed by the electrons as a reverse process of the emission giving rise to a slower cooling for the hot-carriers.[3] It should be emphasized here that the rapid initial cooling rules out the importance of significant screening of electron-phonon interaction in the present study. If the initial screening was important,[1] the initial rapid cooling would be slow and a nonequilibrium phonon population would not be built up.

Another important observation displayed in Fig.(4-4-4) is the time constant of ~30ps for the slow component of carrier temperature cooling curve. This decay time is same as the decay time of the nonequilibrium phonon enhanced phonon replica emission at 780nm (see Fig.(4-4-3)). It is suggested that $\sim 5ps$ is required for the electron system and the nonequilibrium phonon system to be essentially equilibrated with each other. The coupled electron-phonon system then decays with a decay constant 30ps. It should be emphasized that this time constant is the lifetime of non-equilibrium phonons which differ from the equilibrium phonon lifetime of 5-7ps. The longer life time for non-equilibrium phonons than equilibrium phonon is due to the coupling between the hot electrons and nonequilibrium phonons.

The **experimentally determined quasi-Fermi-energies** for electrons and holes from Eq.(4-4-4) are plotted in Fig.(4-4-5). The changes of u_e and u_h are very rapid with the first 10ps reflecting a rapid decrease of the carrier density. The behavior of the degeneracy for electrons and holes with function of time are

reversed due the difference in effective masses for the electrons and the holes.

Using the experimentally determined distribution for electrons and holes in terms of $T_c(t)$ and $u_{e,h}(t)$ the energy loss rates for electrons and holes as function of T_c or n_e can be obtained. The energy loss rate ($P_{e,hh}$) is **defined** as follows:

$$P_{e,hh} \equiv \frac{d <E>_{e,hh}}{dt} = \frac{d}{dt} \left[\frac{\int_0^\infty \epsilon f(T_c, u_{e,hh}, \epsilon) d\epsilon}{\int_0^\infty f(T_c, u_{e,hh}, \epsilon) d\epsilon} \right]. \qquad (4\text{-}4\text{-}6)$$

When the electron-hole system is treated as the Maxwell-Boltzmann gas, (i.e., the electrons and holes have same distribution function which is Maxwell-Boltzmann distribution) the energy loss rate for the carriers (c=e,hh) is given by:

$$P_c = K \frac{dT_c(t)}{dt}. \qquad (4\text{-}4\text{-}7)$$

It should be pointed that the energy loss rates for electrons and heavy-hole obtained by Eq.(6) are the *net* loss rates. These include the energy loss due to electron(hole)-phonon interactions and the energy exchange between electrons and holes by carrier-carrier scattering. The hole-phonon scattering rates were calculated[24] and measured[6] to be 2.5 to 3 times larger than the rate for electrons due to the additional coupling through the deformation-potential. The energy transfer from electrons to holes should be expected in our photogenerated carrier system as long as the characteristic time for electron-hole scattering is shorter than the electron-phonon scattering time.

The **experimentally determined energy loss rates** using Eq.(4-4-6) or Eq.(4-4-7) are shown in Fig.(4-4-6). The solid and dotted curves were obtained

from Eq.(4-4-6) for electrons and heavy-holes, respectively. The dot-dashed curve was obtained from Eq.(4-4-7). It should be pointed out that the curves obtained from either Eqs.(4-4-6) or (4-4-7) are the experimental data because the distribution $f\ (T_c\ ,\ u_{e,h}\ )$ was experimentally determined. The broken line in Fig.(4-4-6) is calculated based on the simple theory[5] where the lattice can be treated as a heat bath for quasi-equilibrium carriers. This theoretical curve does not agree with experimentally determined curves. The smaller P_{hh} than P_e is because of the presence of light-hole population and the different masses for electron and hh which leads to different behaviors of quasi-Fermi energies for electron and hh as function of time.

The salient features of the experimental determined curves displayed in Fig.(4-4-6) are:

(i) The experimental obtained energy loss rate for electrons is more than two order smaller than predicted by the simple theory[5] (broken line). The reasons for difference arises from the re-heating of electrons by non-equilibrium phonons. The energy loss rate determined for electrons by scattering with LO-phonons via the wave-vector dependent Frohlich interaction may be even smaller than what we have determined because the net energy loss rate determined from Eq.6 is sum of rates due to electron-phonon interactions and electron-hole interactions.

(ii) The *net* energy loss rates for electrons and heavy-holes almost follow the rate determined from Eq.(4-4-7). The reasons for this are the rapid decrease of u_e as shown in Fig.(4-4-5) as well as the slow cooling of the carrier temperature which result in $u_e\ /\ KT_c < 0.5$, making the electron-hole system behave more like

a Boltzmann gas.

(iii) The energy loss rates increase as T_c increase. The curves in Fig.(4-4-6) even bends over and approaches the maximum value of $5.3\times10^{-8}W$ for bulk GaAs. This "bending" behavior reflects the initial rapid cooling of hot carriers and was also observed by Shah *et al.*.[6] This may be the indication for the presence of nonequilibrium phonons in the system.

The average phonon emission time for hot carrier to emit a LO phonon is defined by:[7,8]

$$\tau_{avg} = \frac{E_{LO}}{P_e} e^{-E_{LO}/KT_c} . \qquad (4\text{-}4\text{-}8)$$

The value of τ_{avg} as function of the carrier temperature is plotted in Fig.(4-4-7). This is just another way to describe the energy relaxation process. As can be seen the τ_{avg} **is not a constant but carrier temperature dependent and hence time dependent.** For $T_c > 1200K$ or t < 5ps the τ_{avg} remains at a value of about 1ps. As time t > 5ps (or $T_c < 1200K$) the τ_{avg} increases quickly with decrease of the carrier temperature. At $T_c = 480K$, τ_{avg} is 10ps. Ryan *et al.*[8] obtained a constant value of 7ps for τ_{avg} by studies of time-resolved photoluminescence of modulation doped-MQW. The reason for this is simply because their time resolution did not allow them to monitor the entire carrier cooling process. At the early stage of carrier cooling only an up-limit of 0.9ps was determined from the data shown in Fig.(4-4-3). The theoretical predicted value should be $\sim 0.16ps$ [7] which is consistent with our value within the limited time resolution. As soon as a large nonequilibrium phonon population is built up the carrier cooling is suppressed due to re-heating resulting in a larger τ_{avg}.

Information about the initial carrier population can be obtained using experimentally determined distribution function $f_{e,h}$. The densities are obtained by the following expressions:

$$n_e(t) = \int_0^\infty \rho_e \, f_e \, d\epsilon \, ; \tag{4-4-9}$$

$$n_{hh}(t) = \int_0^\infty \rho_{hh} \, f_h \, d\epsilon \, ; \tag{4-4-10}$$

$$n_{lh}(t) = \int_{\Delta E}^\infty \rho_{lh} \, f_h \, d\epsilon \, , \tag{4-4-11}$$

where ΔE is the energy separation between the hh- and lh-subbands at the zone center. The relation $n_e = n_{hh} + n_{lh}$ must be satisfied. The carrier densities for electrons, heavy-holes, and light-holes as function of time are plotted in Fig.(4-4-8) using the experimental determined distribution functions. The quantity of $ln\,[n_e(t)]$ is also plotted in Fig.(4-4-8) as a broken curve.

The salient feature of the data in the Fig.(4-4-8) is that the carrier density decreases non-exponentially and very rapidly within first 30ps after the end of 0.5ps pulse excitation. One can not define a single carrier lifetime due to the non-exponential of the density curves. However, an effective carrier depletion time [density decreases by a factor of e^{-1} from $n_e(t=0)$] is deduced to be as short as 10ps. The slow component of density decay curve reflects part of bimolecular recombination process. The fast decrease of carrier density occurring in such a short time cannot be accounted for by the usual bimolecular recombination, which is a much slower process, on the nanosecond time scale in the bulk GaAs and about 350ps in quantum well structure with well thickness of ~5nm.[25] This short carrier depletion time is *not* caused by the rapid carrier diffusion which is

described in the another paper.[9]

Such a short intial carrier depletion time $\sim 10ps$ can only be accounted for consistently by the participation of nonequilibrium phonons. The nonequilibrium LO phonons in the quantum well system play two essential roles. First, these phonons can substantially suppress the energy relaxation process of carriers due to reabsorption of these phonons by carriers. Second, since these phonons are localized in both wavevector space and real physical space (in the well plane) they can behave like coherent Bosons. The existence of the coherent Bosons will tend to increase the number of the Bosons in the system with a rate proportional to the present number of Bosons resulting in a stimulated phonon emission process. This can give rise to the phonon replica emission, i.e., when an electron in the conduction subband recombine with a hole in the valence subband not only a photon but also a phonon or more phonons will be emitted to join the Boson system. Since this is a stimulated process, it is very effective to exhaust carriers from the system. Unlike conventional stimulated emission in semiconductor laser, this process is expected to be even more effective at room temperature since equilibrium phonon occupation will also increase as lattice temperature increases. The nonequilibrium phonon induced stimulated-phonon-emission has been confirmed by the detailed polarization studies of integrated luminescence spectra discussed in steady-state section. *By employing the nonequilibrium-phonon model we able to explain not only the slow carrier cooling but also the ultrashort carrier depletion time in highly photoexcited undoped quantum well structures.*

4.5 Conclusion

With 2ps time resolution we are able to study the initial energy relaxation of the hot carriers and the decrease of carrier density simultaneously. The existence of a large population of nonequilibrium phonons in highly excited semiconductor quantum well structures is experimentally verified. Its effect on the energy relaxation is to slow down the cooling rate after an initial rapid cooling (0-5ps). A new mechanism to explain the ultrashort carrier depletion time $\sim 10ps$ deduced from the fitting of time-resolved photoluminescence profiles at various emitted photon energies is proposed to be associated with nonequilibrium phonon enhanced phonon replica emission rather than other nonradiative processes.

Reference

(1) R. J. Seymour, M. R. Junnarkar, and R. R. Alfano, Solid State Commun. 41, 657(1982).

(2) J. Shah, Solid-State Electronics, 21, 43(1978).

(3) H. M. van Driel, Phys. Rev. B, 19, 5928(1979).

(4) C. V. Shank, R. L. Fork, R. Yen, J. Shah, B. I Greene, A. C. Gossard and C. Weisbuch, Solid State Commun. 47, 981(1983).

(5) E. M. Conwell, "High Field Transport in Semiconductors" (Academic, New York, 1967).

(6) J. Shah, A. Pinczuk, A. C. Gossard, and W. Wiegmaann, Phys. Rev. Lett., 54, 2045(1985).

(7) C. H. Yang, Jean M. Carlson-Swindle, A. Lyon, and J. M. Worlock, Phys. Rev. Lett., 55, 2359(1985).

(8) J. F. Ryan, R. A. Taylor, A. J. Turberfield, A. Maciel, J. M. Worlock A. C. Gossard, and W. Wiegmann, Phys. Rev. Lett. 53, 1841(1984).

(9) Kai Shum, M. R. Junnarkar, H. S. Chao, R. R. Alfano, SPIE conference proceeding, vol.793, 1987.

(10) P. P. Ho, A. Katz, R. R. Alfano, and N. H. Schiller, Optics Commun. 54, 57(1985).

(11) Kai Shum, P. P. Ho, and R. R. Alfano, Phys. Rev. B 33, 7259(1986).

(12) Kai Shum, M. R. Junnarkar, H. S. Chao, R. R. Alfano, (unpulished).

(13) R. Sooryakumar, D. S. Chemla, A. Pinczuk, A. C. Gossard, W. Wiegmann, and L. J. Sham, Solid State Comm., 54, 859(1985).

(14) J. E. Zucker, A. Pinczuk, D. S. Chemla, A. C. Gossard, and W. Wiegmann, Phys. Rev. Lett., 53, 1280(1984).

(15) H. Iwamnra, T. Saku, H. Kobayashi, and Y. Horikoshi, J. Appl. Phys., 54, 2692(1983).

(16) N. Holonyak, Jr., R. M. Kolbas, W. D. Laidig, B. A. Vojak, H. Hess, R. D. Dupuis, and P. D. Dapkus, J. Appl. Phys., 51, 1328(1980).

(17) P. Blood, E. D. Fletcher, P. J. Hulyer, and P. M. Smowton, Appl. Phys. Lett., 17, 1111(1986).

(18) M. S. Skolnick, K. J. Nash, P. R. Tapster, D. J. Mowbray, S. J. Bass, and A. D. Pitt, Phys. Rev. B, 35, 5925(1987).

(19) The absolute intensity at different transition energies was obtained with same excitation condition. To do this, we fixed the channel plate gain, temporal analyzer gain, prepulse intensity as well as time scale for the weakest signal (at high energy tail) to be detected. The intensity of pre-pulse was then treated as the standard of excitation level. As intensity increases at lower energies, neutral-density(ND) filter(s) can be placed in the luminescence path if necessary. For the curves in Fig.(4-4-3) and Fig.(4-4-5) ND filter was not used to attenuate the luminescence intensity.

(20) The decay times were obtained by fitting the data in Fig.(4-4-3) to the expression of $I(E, t) = I_0[1 - e^{-t/\tau_r}] e^{-t/\tau_d}$, where the parameters ($I_0$, τ_r τ_d) are the proportional constant, the rise time, and the decay time, respectively.

(21) The ratio of squared matrix elements between $e-hh$ and $e-lh$ was estimated from a calculation by Y. C. Chang and G. Sanders, Phys. Rev. B, 32, 5521(1985).

(22) For a recent review, see J. Shah and R. F. Lehery in "Semiconductors Probed by Ultrafast Laser Spectroscopy" edited by R. R. Alfano, Academic Press, New York,1984; pg.45.

(23) R. K. Chang, J. M. Ralston, and D. E. Keating, in "Proceeding of the International Conference of Light Scattering Spectra of Solid", edited by G. B. Wright (Springer-Verlag, New York, 1969), pg.369.

(24) M. Costato, and L. Reggiani, Phys. Status Solidi (b) 58,,47(1973).

(25) E. O. Gobel, H. Jung, J. Kuhl, and K. Ploog, Phys. Rev. Lett., 51, 1588(1983).

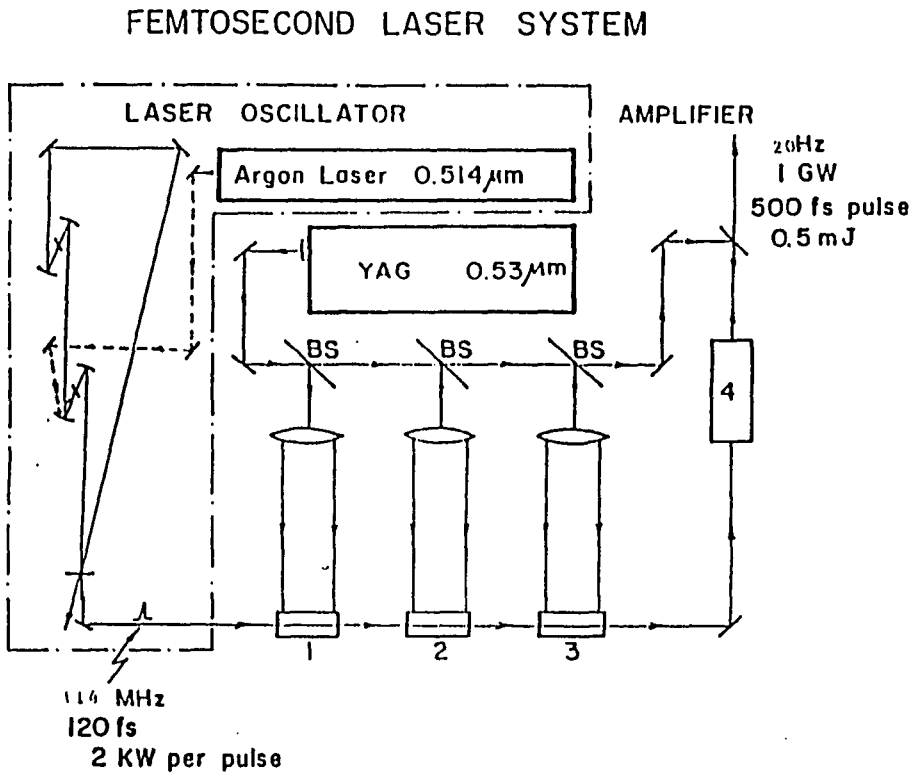

Fig.(4-3-1) A block diagram od subpicosecond dye laser system.

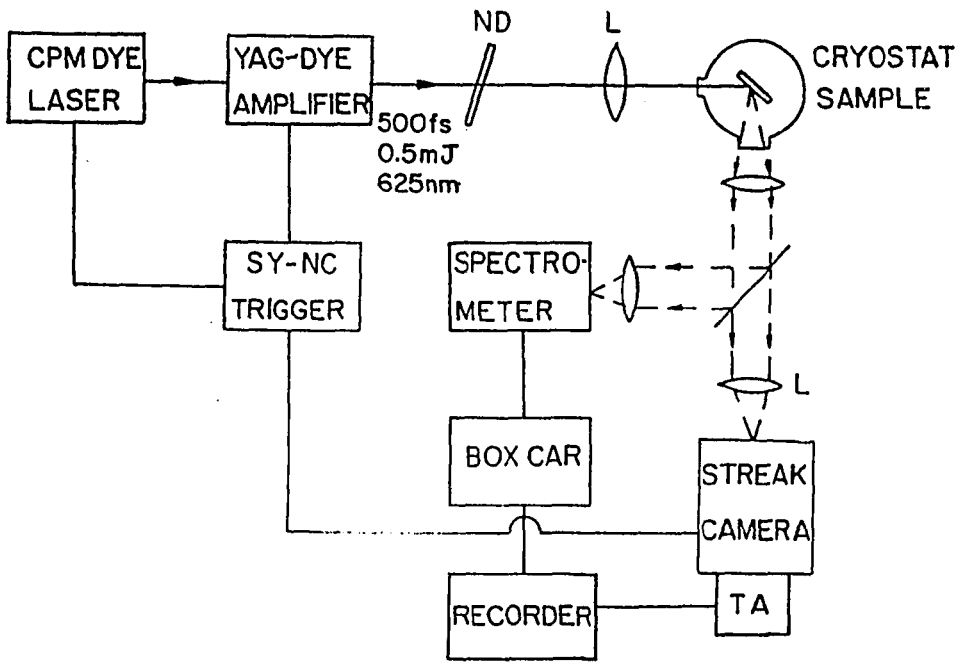

Fig.(4-3-2) The experimental set-up used for time-integrated and time-resolved (2ps time resolution) photoluminescence studies.

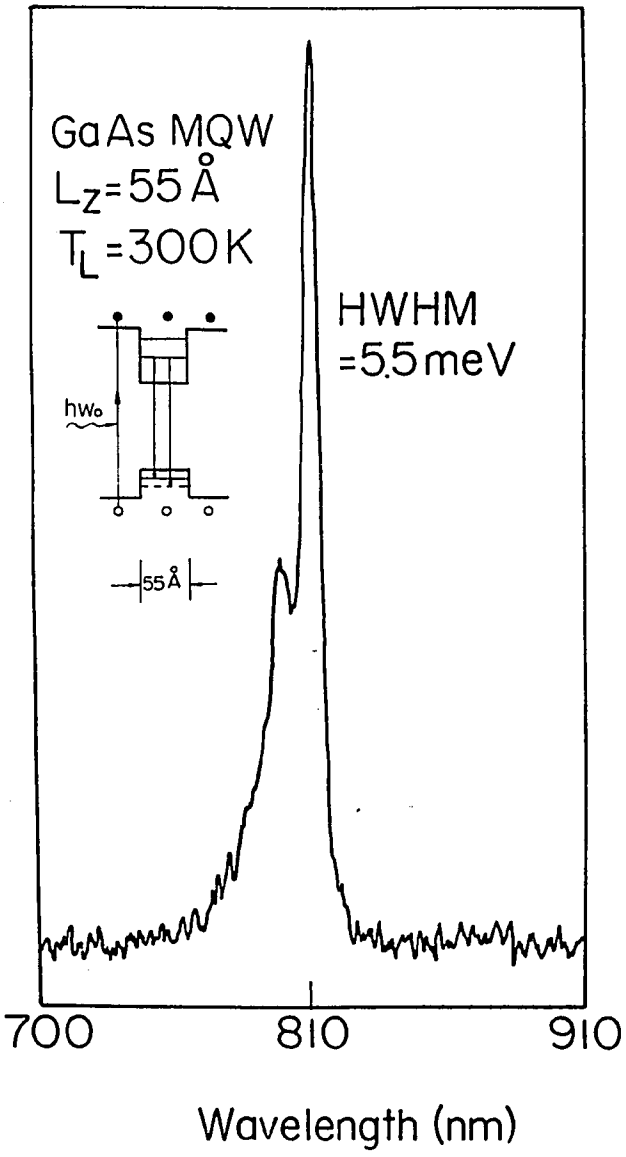

Fig.(4-3-3) Room temperature photoluminescence spectra of the 55Å MQW structure excited by a 514.5nm argon ion laser (5mW, ~ 400*um* excitation-spot size). The spectrum shows n=1 light-hole and heavy-hole exciton transitions as shown in the inset. The HWHM is about 5.5meV.

(a)

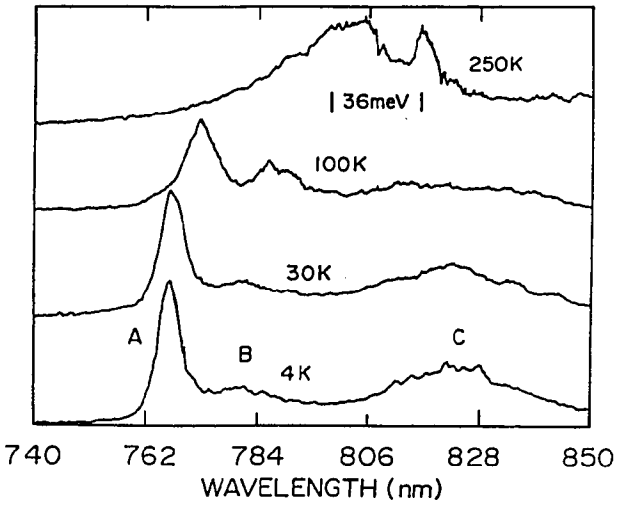

(b)

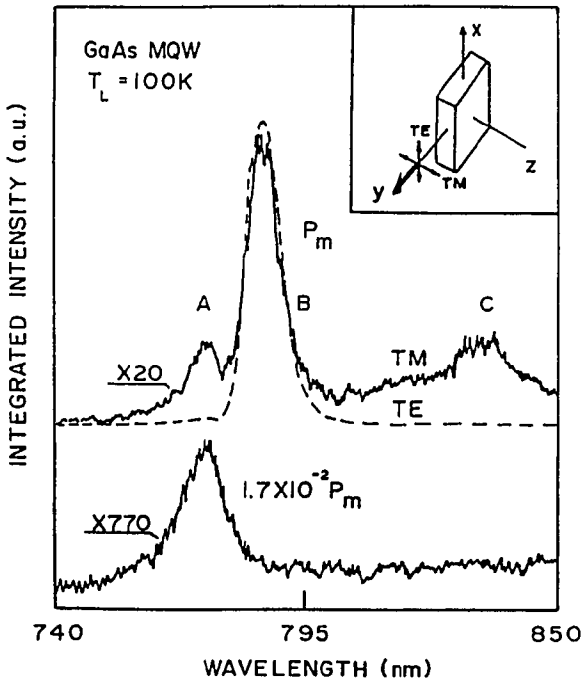

Fig.(4-4-1) (a) Time-integrated luminescence spectra at various lattice temperatures. The peaks A, B, and C are explained in the text. (b) Time-integrated luminescence spectra taken in the geometry as shown in the inset at 100K.

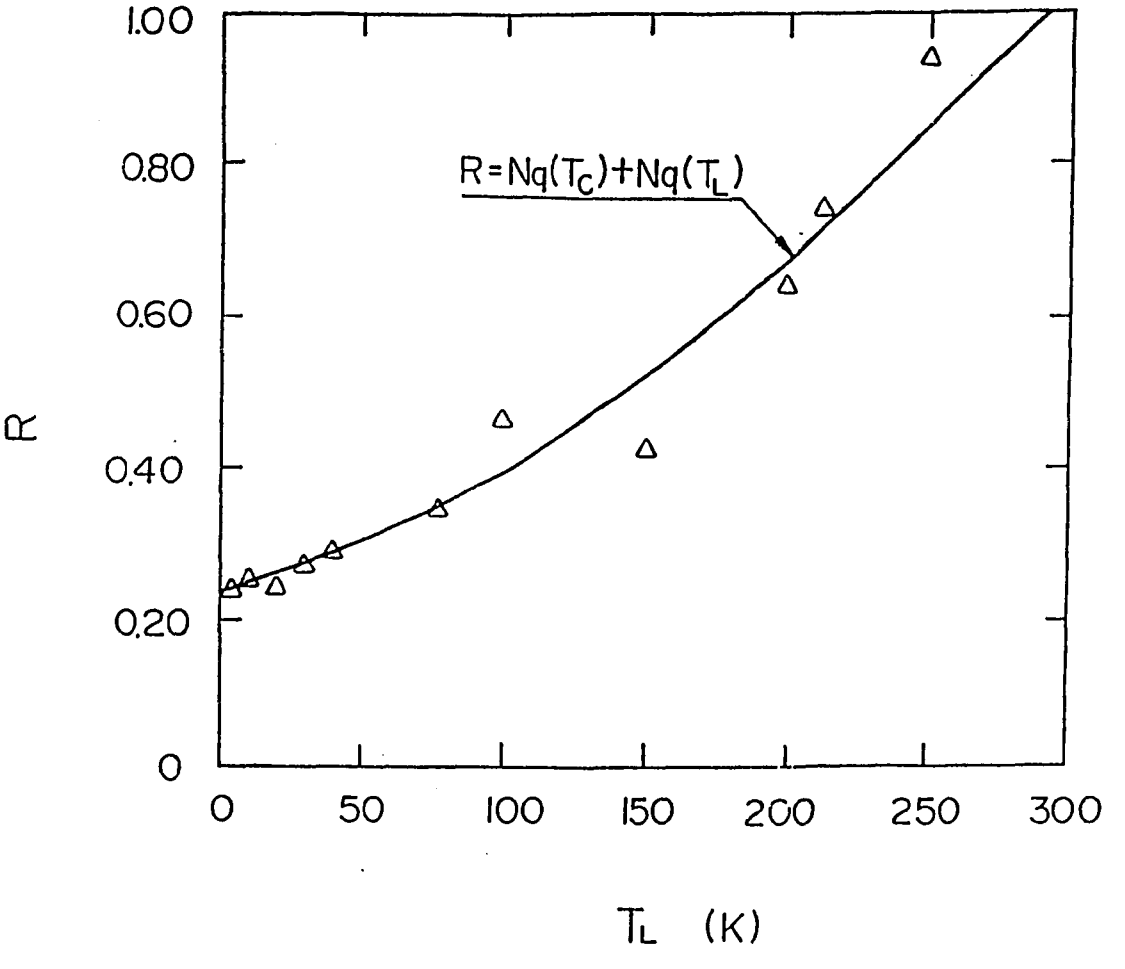

Fig.(4-4-2) The triangles are the ratios of the peak intensity of B and A indicated in Fig.(4-4-1). The solid curve is explained in the text.

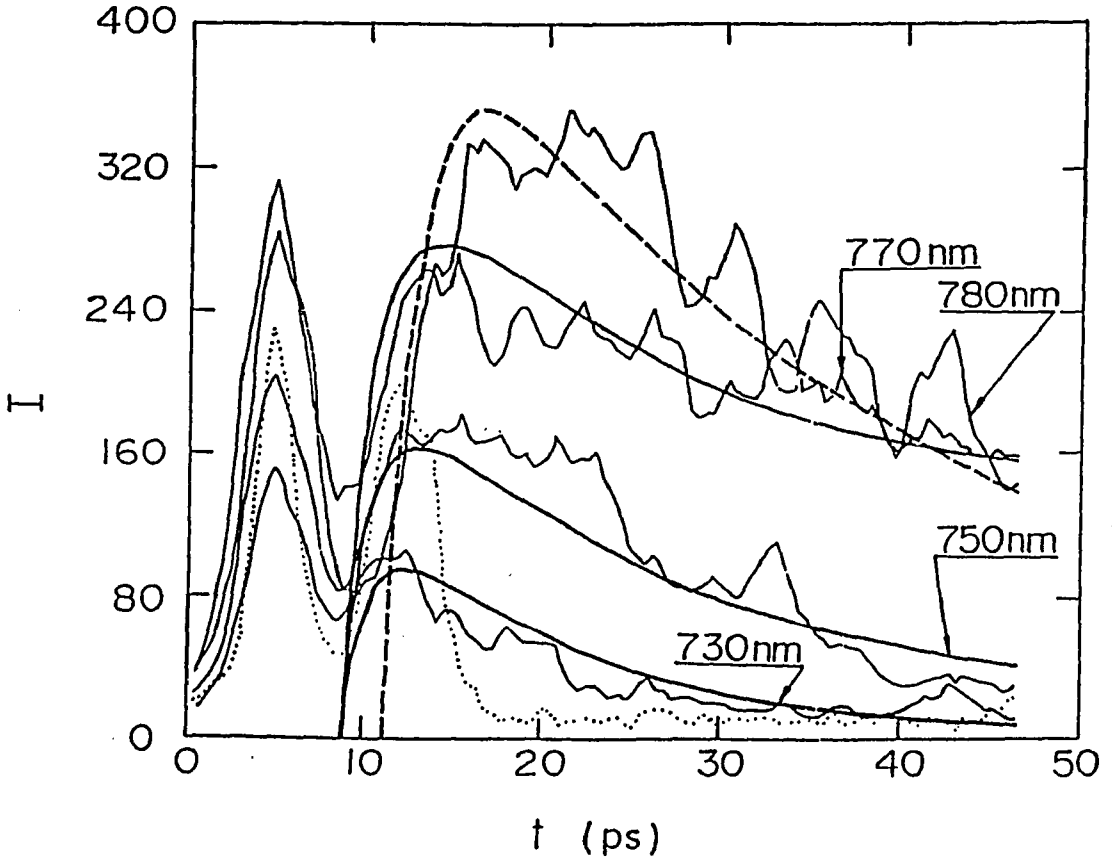

Fig.(4-4-3) Time-resolved photoluminescence profiles (thin solid curves) from the symmetric MQW at 4K at various wavelengths. The narrow peaks within 0-10ps are the pre-pulses used for averaging. The next peak of dotted curve is the Rayleigh scattering light from the sample surface. The thick broken curve is generated by an expression of $I(E,t)=I_0[1-e^{-t/\tau_r}]e^{-t/\tau_d}$ and the thick solid curves are generated by Eq.(4-4-1).

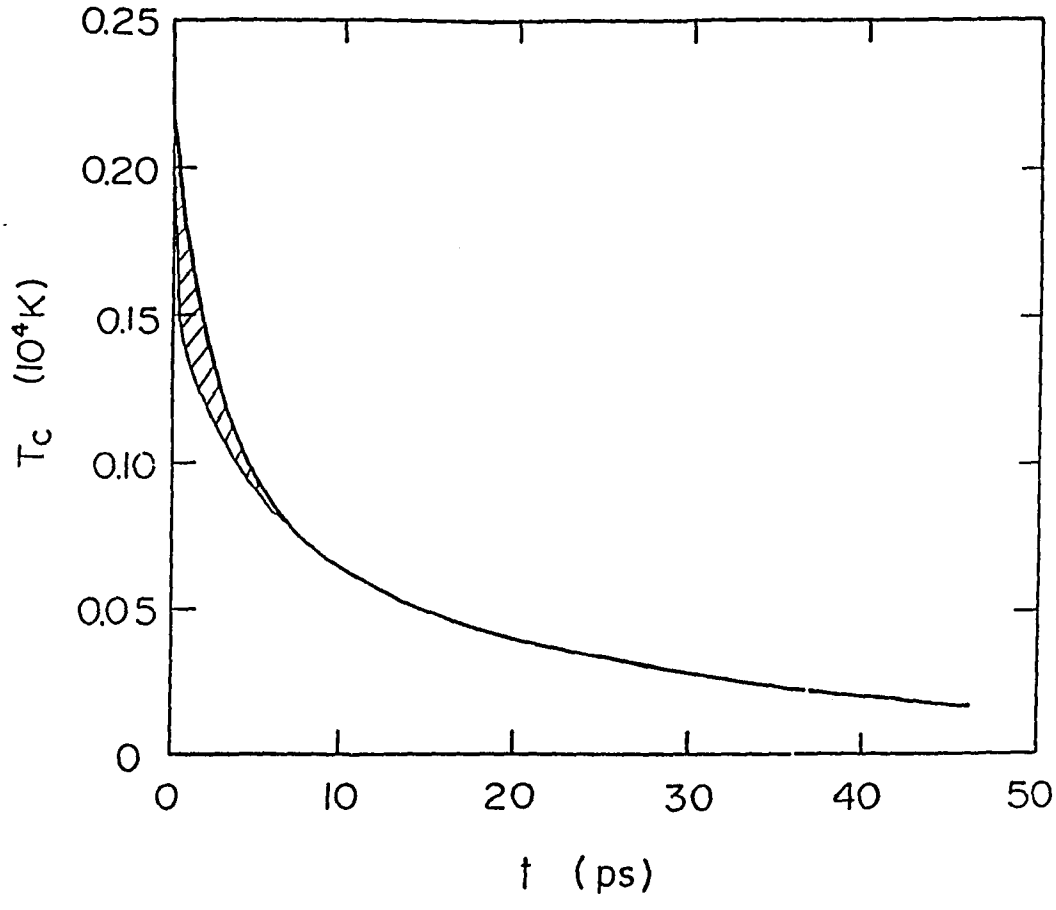

Fig.(4-4-4) Experimentally determined carrier temperature as function of time. The shaded area indicates the extent of uncertainty in deducing carrier temperature within first 4ps.

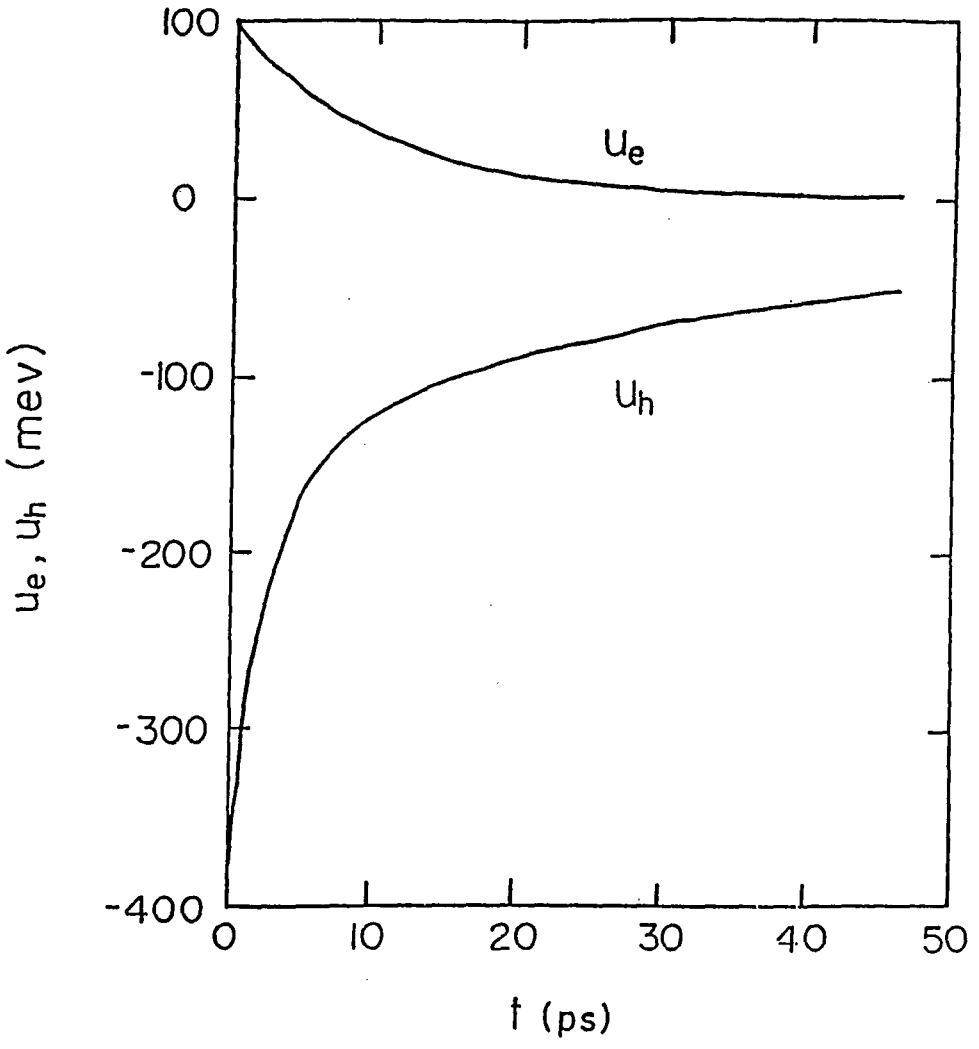

Fig.(4-4-5) Experimental determined quasi-Fermi energies for electrons (up solid curve) and for holes (down solid curve).

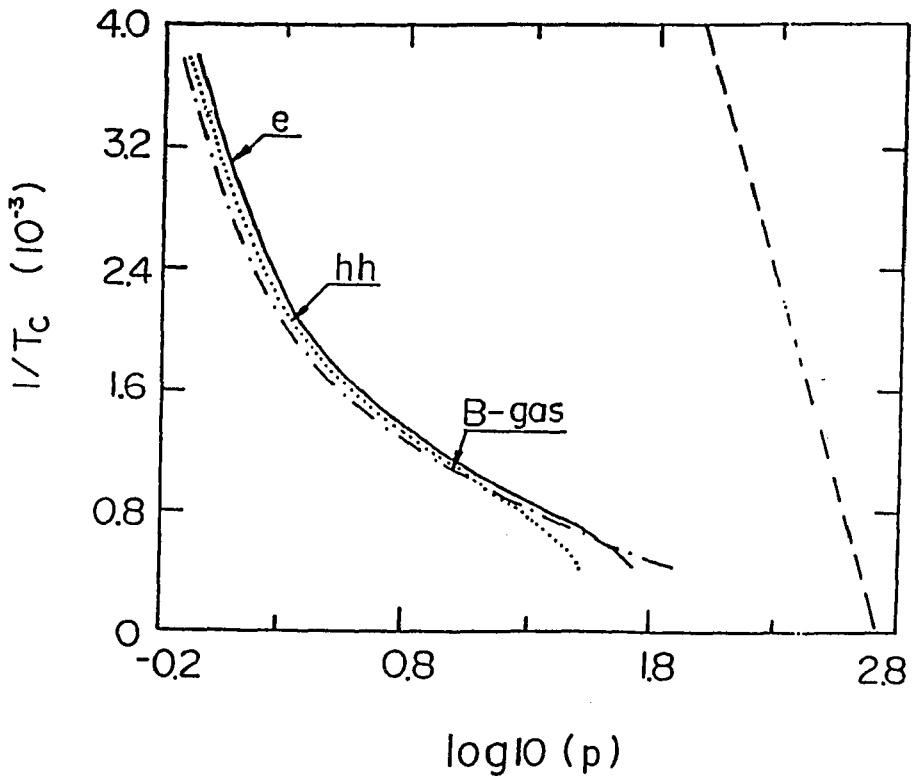

Fig.(4-4-6) Experimentally determined *net* energy loss rates for electrons (e) and heavy-holes (hh) obtained from Eq.(4-4-6). The dot-dashed curve is obtained from Eq.(4-4-7). The broken line is theoretical result for bulk GaAs. The power unit is 10^{-10} watts.

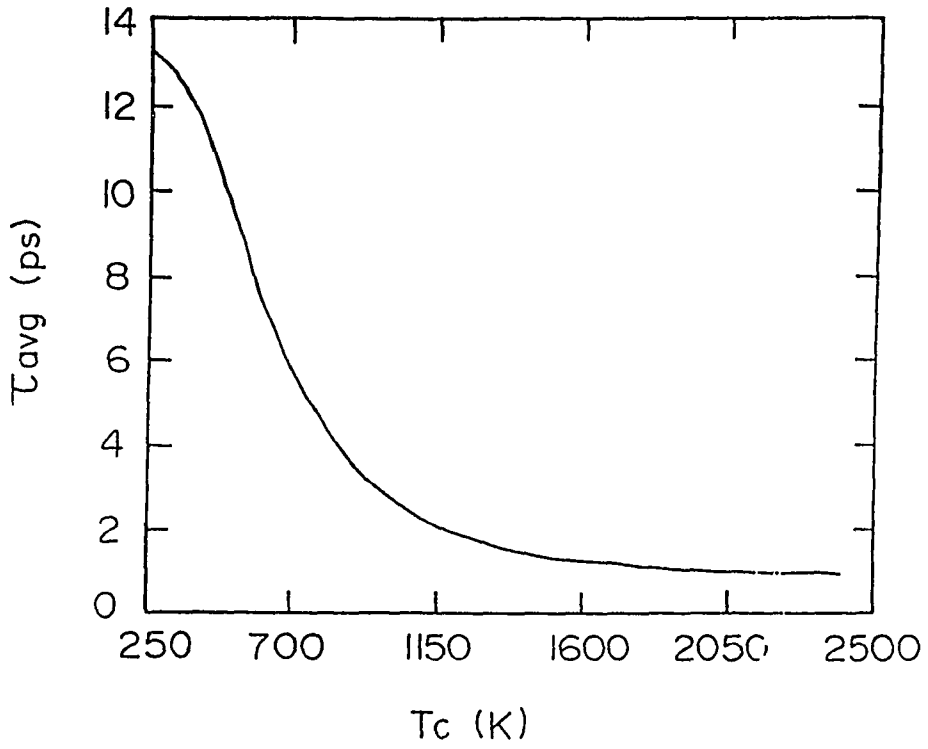

Fig.(4-4-7) Experimentally determined average phonon emission time as function of carrier temperature obtained from Eq.(4-4-8).

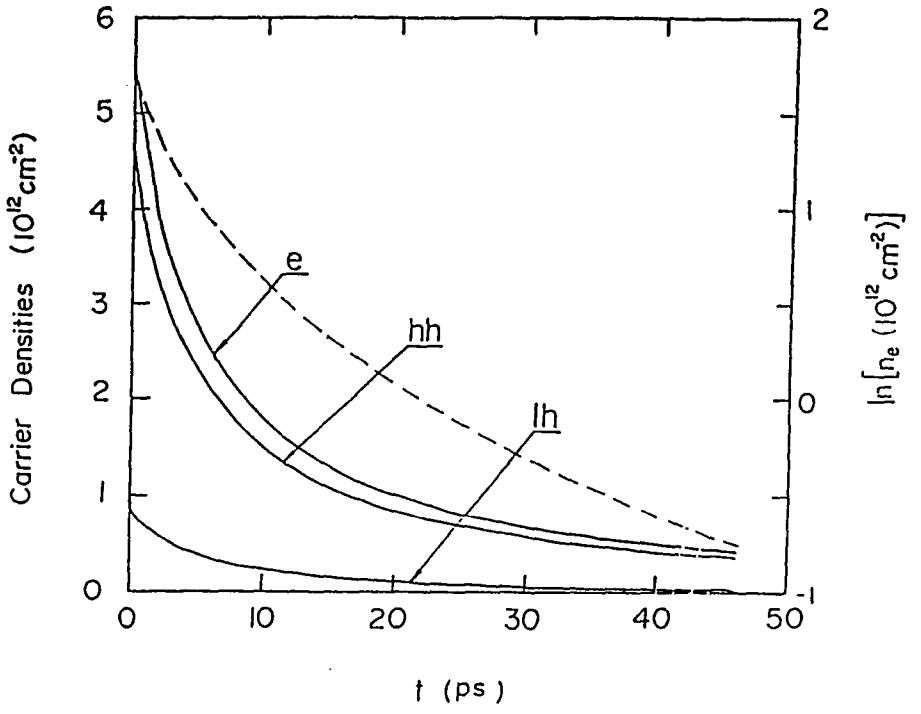

Fig.(4-4-8) Experimentally determined carrier densities as function of time. e for electron, hh for heavy-hole, and lh for light-hole. The broken curve is the nature logarithm plot of electron density.

Chapter 5

Ultrafast Carrier Diffusion in An Asymmetric GaAs Quantum Well

5.1 Introduction

Electron-hole plasma expansion in semiconductor bulk and quantum well structures at high photo-excitation power density is a subject of great interest from both a theoretical and a device points of view. Various methods have been employed to study dynamic process of carrier diffusion such as spatially and spectrally time-resolved luminescence spectroscopy[1,2] and Raman scattering.[3,4] Different mechanisms have been suggested to explain the rapid carrier diffusion in bulk semiconductors. Rapid electron-hole diffusion has been observed[2] in CdSe at 4K but not at room temperature. The absence of larger number of thermal phonon at low temperature made it possible to observe the rapid carrier diffusion process. Using a streak camera Junnarkar and Alfano[5] were able to measure the difference between the spatial profiles of the pump laser and the photoluminescence at various excitation levels from which the diffusion velocity was estimated to be on order of $10^8 cm / s$ at high photo-excitation at room temperature. Such a large diffusion velocity was attributed to screening of polar electron-phonon interaction and partially screened nonpolar electron-phonon interaction. High internal pressure of a

very dense electron-hole plasma has been proposed[6] to account for the rapid expansion of plasma. The pioneering work of Tsen and Morkoc[4] have shown no influence on photogenerated carrier diffusion by carrier confinement, zone-folding of phonon modes, and phonon confinement in symmetric GaAs/AlGaAs MQW structure at low carrier density using time-resolved Raman scattering data.

In this chapter, we report on the first measurement of ultrafast carrier diffusion in the lateral x-y plane in a single asymmetric quantum well. The present work explores three questions: (1) How the potential profile of quantum well structure affects on the carrier diffusion in well plane (x-y plane); (2) Whether the carrier diffusion is responsible for ultrashort carrier lifetime in highly photoexcited undoped quantum well structures; and (3) what are the maximum diffusion constant D and the diffusion velocity in the x-y plane of quantum wells at high carrier density.

5.2 Quantum Well Structure

The undoped GaAs/$Al_xGa_{1-x}As$ asymmetric quantum well investigated in this work was grown by molecular-beam epitaxy on a (001)-oriented undoped GaAs substrate. The asymmetric quantum well consists of layers from the front surface to substrate 150Å $Al_{0.3}Ga_{0.7}As$, 50Å GaAs well, 200Å AlAs (asymmetric barrier), followed by $1um$ $Al_{0.3}Ga_{0.7}As$, and $0.2um$ GaAs buffer layer on Si-doped GaAs substrate. The lateral size of the sample is $2\times6mm$. The good quality of the sample is confirmed by well resolved heavy-hole and light-hole excitonic structures at room temperature as shown in Fig.(5-2-1). The intensity dependence of

photoluminescence from n=1 electron to the both n=1 hh and lh transition on excitation power density (I_e) is shown in Fig.(5-2-2). The luminescence intensities from the both hh-exciton and lh-exciton vary as $I_e^{3/2}$. This behavior implies that exciton annihilation which gives rise the luminescence is competing with the exciton ionization process due to a larger population of thermal phonons at room temperature. The HWHM for the heavy-hole exciton is about 7.4meV. The sample was mounted on the cold finger in an optical helium cryostat.

5.3 Experimental Method

A schematic diagram of photoluminescence image on the screen of streak camera is depicted in Fig.(5-3-1) to show how we studied the dynamics of carrier diffusion. The area inside the fulled-line circle is the laser excited area. If there is no carrier diffusion, photoluminescence should be restricted inside this circle. Suppose sufficient electrons and holes can diffuse far enough to unexcited area where they can recombine one should able be to detect the luminescence from the unexcited area (outside the fulled-line circle). Using a streak camera in the focus mode we were able to measure the spatial profiles of the laser and the luminescence at the sample surface. Those spatial intensity profiles were integrated over a time duration of 1ns. The width (FWHM) of spatial profile should give information on how far carriers can diffuse within 1ns. However, this information is not adequate to deduce accurate values of diffusion constant and diffusion velocity. To study dynamic diffusion process quantitatively we make use of two electronic windows to obtain time-resolved photoluminescence from the areas of excited (I_{sc}) and unexcited (I_{se}) simultaneously (and thus laser intensity fluctuation was

completely avoided).

An ultrashort light pulse of 500fs duration at 620nm was used to excite the electron-hole pairs with a carrier density of $\sim 10^{19}cm^{-3}$. This light source was generated from a colliding-pulse passive mode-locked dye laser and amplified by a four-stage dye amplifier pumped with a frequency doubled Nd: YAG laser at 20Hz. The photoluminescence was spectrally filtered using various narrow band filters(10nm), and temporally dispersed by a 2ps Hamamatsu streak camera system. The luminescence intensities were corrected for the nonlinearity of streak rate, the spectral response, and the transmission of each narrow band. The time resolution for the present work is about 2ps. The experimental apparatus used in this research has been described in the chapter 4.

5.4 Results and Discussions

The time-integrated laser and luminescence profiles at the surface of the asymmetric quantum well are plotted in Fig.(5-4-1). The gain of detecting system was adjusted such that the maximum intensity recorded was roughly the same. The most inside solid curve and dotted curve are the laser profile and the Gaussian-line-fit of the laser profile, respectively. The center energies of the luminescence are indicated on the curves. Much broader widths of luminescence profiles than that of laser implies a rapid carrier diffusion in the x-y plane.

In Fig.(5-4-2) the time-resolved photoluminescence profiles[8] (thin curves) from the center window are shown at three typical energies. The emissions centered at 760nm arise from the recombinations of electrons and holes near the

respective first subband edges. The rise times of these luminescence profiles is 2ps time resolution limited reflecting fast initial carrier cooling. In order to study the dynamic diffusion process of carriers which are spatially localized within the photoexcitation spot $\sim 168um$ in diameter at $t=0$, the carrier density (n_e, n_{hh}, n_{lh}) as function of time must be determined. This can be done by the method developed in the previous chapter, i.e., by fitting the luminescence profiles in time domain using carrier density and carrier temperature (T_c) as two parameters. Assuming the direct optical transition the luminescence intensity as function of time is reiterated here:

$$I(E_i, t) = C_i(1-e^{-t/\tau_r}) \tag{5-4-1}$$

$$[\,|M_{e-hh}|^2 \rho_e f_e \rho_{hh} f_h + |M_{e-lh}|^2 \rho_e f_e \rho_{lh} f_h\,],$$

where the $\rho_{e,hh,lh} \sim m_{e,hh,lh}$ are the density of state for electron, heavy-hole, and light-hole; the $M_{e-hh(lh)}$ is the matrix element for electron to hh(lh) transition; C_i absorbed all the constant factors including the corrections for detector response and the transmission of each narrow band filters used; τ_r is the rise time of luminescence and is set to be 1ps (approximately the response time of the system) which is an up-limit of thermalization time of electron-hole system;

$$f_{e,h} = \frac{1}{e^{(\epsilon_i - u_{e,h})/KT_c} + 1} \tag{5-4-2}$$

is the Fermi-Dirac distribution for electrons in conduction band (with subscript e) and for holes in valence band (with subscript h). The quasi-Fermi energy of holes (u_h) is related to the quasi-Fermi energy for electrons (u_e) and the carrier tem-

perature by the relation of

$$n_e = n_{hh} + n_{lh} \quad . \tag{5-4-3}$$

This value is given by:

$$u_h = KT_c \, ln \, [e^{a ln (1 + e^{u_e / KT_c})} - 1 \,] \quad , \tag{5-4-4}$$

with

$$a = \frac{m_e}{m_{hh} + m_{lh}} \quad . \tag{5-4-5}$$

A **unique** set parameters of $T_c(t)$ and $u_e(t)$ was used to consistently fit **all** the luminescence profiles detected at different photon energies E_i. Three calculated luminescence profiles are shown in Fig.(5-4-2) by the thick solid curves.

Using the experimental determined carrier distribution in terms of T_c and u_e the carrier density as function of time can be determined. The nature logarithm of electron density is plotted against the time. As can been seen from the plot the carrier density decreases non-exponentially and very rapidly within the first 30ps after the end of 500fs laser pulse excitation. A single carrier lifetime can not be defined because of the non-exponential of density decay curve. However, an effective carrier depletion time (τ) as defined in the 4th chapter is obtained to be as short as 10ps. The value of τ is dependent upon radiative, non-radiative and carrier diffusion. Apparently, such a short carrier depletion time can be primarily attributed to the rapid carrier diffusion in x-y plane as it is consistent with the time-integrated spatial luminescence profiles. However, we show below this is not the case.

In Fig.(5-4-3), the time-resolved photoluminescence for both the I_{se} and the I_{sc} measured at 4K with 2ps time resolution are plotted. In order to have detectable luminescence intensity for both windows a wide-band filter (FWHM ~35nm) center at 700nm was placed in the luminescence path. The peak of the broken curve is the Rayleigh scattering light from the sample surface which defines the "zero" time for our analysis. As can be seen the rise time of the I_{sc} is time-resolution limited, while rise of I_{se} is much slower than that of I_{sc} and also well resolved. The total number of emitted photons from two windows within 25ps is comparable. Before detailed analysis and drawing any quantitative conclusions based on carrier diffusion process, one possible artifact that lead anomalously strong luminescence measured from the window which is laterally displaced by ~ 700*um* should be pointed out and alleviated. Such a possibility arises from the 1*um* layer of $Al_{0.3}Ga_{0.7}As$ which is next to AlAs barrier. This layer is also highly excited by the 620*nm* excitation pulse. Possible recombination radiation from this layer will excite carriers within the well. This secondary excitation would not be limited to the originally excited area giving rise secondary luminescence. There are two reasons to eliminate this possiblity. First, we did not detect any luminescence from radiative recombination in the $Al_{0.3}Ga_{0.7}As$ layer either from the sample surface or sample edge. This is becuase carriers are effectively trapped into 0.2*um* GaAs buffer layer which lies below the $Al_{0.3}Ga_{0.7}As$ layer. Second, the luminescence intensity I_{se} would rise and decay quite similarly with I_{sc} since speed of light in GaAs is about 100*um* / *ps*. This is contrary to our experimental observation.

To gain more information on dynamic process of carrier diffusion in x-y

plane of this asymmetric well, the luminescence profiles of I_{sc} and I_{se} must be properly analyzed. The I_{sc} was fitted by Eq.(5-4-1) using the same set of T_c and u_e determined from the data shown in Fig.(5-4-2). The only choice for theoretically fitting data I_{se} is to use standard classical diffusion equation to calculate the carrier density as function of time t and distance r. The exact values of separation between the two window and the widths of the window are given in Fig.(5-3-1). This method should be adequate as long as electrons act more like particle rather than wave.

The diffusion equation which describe the lateral carrier transport of the photogenerated carriers is given by:

$$\frac{\partial n(r,t)}{\partial t} = -\frac{n(r,t)}{\tau} + D\frac{\partial^2 n(r,t)}{\partial r^2}, \quad r \geqslant 0 \qquad (5\text{-}4\text{-}6)$$

where D is diffusion constant of carriers, and τ is the lifetime of carriers. As noticed above there is no a single carrier lifetime that describes carrier density decay. The value of τ may be also position dependent because of nonradiative processes are usually carrier density dependent. However, since we are interested in the initial carrier diffusion process (0-25ps) τ can be treated as a constant. It should be pointed out that the constant should be equal to $\sim$ 10ps as determined from analyzing time-resolved luminescence profiles which were obtained from the center window. This is because the diffusion equation (5-4-6) applies to whole area of the sample ($r \geqslant 0$), not just for the unexcited area.

The initial condition for carrier density is assumed[2] to be same as laser profile which is:

$$n(r, t=0) = n_0 e^{-4\log 2 \frac{r^2}{a^2}} , \qquad (5\text{-}4\text{-}7)$$

where n_0 is the carrier density at the center of laser spot at $t=0$, and a is $120um$ obtained by fitting the laser profile to Eq.(5-4-7). The solution of the second order differential Eq.(5-4-6) with the given initial condition Eq.(5-4-7) is given by:[2]

$$n(r, t) = n_0 e^{-t/\tau} \left(1 + \frac{16\log 2\, Dt}{a^2}\right)^{-1/2} e^{-\frac{r^2}{a^2/4\log 2 + 4Dt}} . \qquad (5\text{-}4\text{-}8)$$

Assuming ambipolar diffusion, i.e., electrons and holes have same diffusion velocities, the luminescence intensity I_{se} should be governed by the following expression:

$$I_{se}(t) \sim \int_{r_1}^{r_2} n^2(r, t)\, dr . \qquad (5\text{-}4\text{-}9)$$

In this expression, the diffusion constant D is the only parameter to be determined.

The results from fitting measured luminescence data to the calculated using Eq.(5-4-9) are very surprising in two respects. First, the value for D is determined to be $10^6 cm^2/s$, which is more than four orders magnitude greater than the conventional diffusivity of GaAs. The diffusion velocity $v = \sqrt{\frac{D}{\tau}} = 3.2\times10^8 cm/s$ $(3.2um/s)$ is four times larger than the initial Fermi-velocity. Second, even when τ is treated as adjustable free parameter we can not find any other quantity for D and τ to fit the experimental data.

What is the mechanism that causes the ultrafast carrier density decay? In

the chapter 4 where the multiple symmetric quantum wells have been studied, we have attributed this to the nonequilibrium phonon enhanced phonon replica emission. In addition, no unuasual carrier diffusion in x-y plane was measured. For the present asymmetric quantum well structure, it is crucial to assess quantitatively the relative importance on causing the ultrafast carrier density decay between the rapid carrier diffusion and the nonequilibrium phonon enhanced phonon replica emission. Using the determined $n(r, t)$ we can show the contribution of the second term in the right side of diffusion Eq.(5-4-6) in lossing carriers at given position r is always smaller than the first term and thus the ultrashort carrier lifetime can not be attributed to the carrier diffusion but to the nonequilibrium phonon enhanced phonon replica emission. Using the Eq.(5-4-8), the second term of Eq.(5-4-6) can be written as $\frac{n(r, t)}{\tau_D}$, where $\frac{1}{\tau_D}$ is defined as a carrier diffusion rate. The τ_D is given by:

$$\tau_D \equiv \frac{\frac{a^2}{4log\ 2} + 4Dt}{D\ [\frac{4r^2}{(\frac{a^2}{4log\ 2} + 4Dt)} - 2\ ]} \quad . \tag{5-4-10}$$

The quantity $\frac{\tau_D}{\tau}$ as function time (in ps) at given position r (in um) is plotted in Fig.(5-4-5). The thick solid and broken curves are for $r = 0\ um$ and $r = 200\ um$, respectively. The two branch dot-dashed curve is for $r = 84\ um$. From this plot it is easy to see that $|\tau_D|$ is at least 6 times larger than τ reflecting that carrier diffusion is not a dominant mechanism of ultrafast carrier density decay. The other mechanism which arise from nonequilibrium phonon enhanced phonon replica emission as discussed in chapter 4 is responsible for such

an efficient carrier depletion process. The another interesting feature of the plotted curves in Fig.(5-4-5) should be mentioned. For $r < 77.46\ um$ the τ_D is always negative for all t-axis indicative of the carriers always moving out from the $r < 77.46\ um$ region. There are two branches of the curves at given position r for $r > 77.46\ um$ separated by a singularity at $t = 30 - \frac{r^2}{200}$ (ps). For example, at $r = 84\ um$, τ_D is positive for $t < 5.3$ps implying carriers coming from the $r < 84\ um$ region at this position is greater than carriers going out. When $t > 5.3$ps, a reverse case occurs. The singularity at $t = 5.3$ps means the net carrier flow is zero due to diffusion at position $r = 84\ um$.

There are several possible origins of the extraordinary rapid carrier diffusion in the x-y plane of the asymmetric quantum well. (1) The internal pressure[6] of high electron-hole pairs may be extremely large when the density is well above the electron-hole liquid density. (2) There are a large number of the coherent nonequilibrium phonons emitted by hot electrons in the system. These phonons have momenta parallel to the x-y plane and may also drive the carriers outside the excited region by adding the phonon momenta to the carriers. (3) Due to the asymmetric potential well profile there are no transmission states (virtual states or unconfined states) above the energy barriers unlike the symmetric well case. This is the intrinsic property of asymmetric quantum well. The photogenerated carriers may be immediately scattered by the higher energy barrier and obtain momentum from the interface which assists carriers to expand in x-y plane. The initial photogenerated carrier acquires a larger kinetic energy $\sim$ 300meV, thus having a larger carrier diffusion velocity. The origins (1) and (2) seems to be inconsistent with the symmetric well case where no or little lateral diffusion has been

observed except for the subband edge carriers. However, whether mechanism described in (3) is responsible for the observed rapid diffusion is still an open question worthy of further study.

5.5 Summary

In summary, we have observed for the first time the ultrafast carrier diffusion in the x-y plane of the asymmetric quantum well and ultrashort carrier depletion time at the same time. The ultrashort depletion time of photogenerated carrier in the undoped asymmetric quantum well is shown to be not attributed to the rapid carrier diffusion. It is suggested that future theoretical work should investigate the roles of internal pressure of electron-hole gas, nonequilibrium phonons emitted by hot electrons, and the potential well profile in this extraordinary rapid carrier diffusion in lateral x-y plane of the asymmetric quantum well.

Reference

(1) K. M. Romanek, H. Nather, J. Fisher, and E. O. Gobel, J. Lumi., 24/25, 585(1981).

(2) A. Cornet, M. Pugnet, J. Collet, T. Amand, and M. Brousseau, J. Phys. (Paris) Collq. c7, 42, 471(1981).

(3) Charles L. Collins, and Peter Y. Yu, Solid State Commun., 51, 123(1984).

(4) K. T. Tsen, and H. Morkoc, Phys. Rev. B, 34, 6018(1986).

(5) Mahesh R. Junnarkar, and R. R. Alfano, Phys. Rev. B, 34, 7045(1986).

(6) R. Zimmermann, and M. Rosler, Phys. Stat. Sol. (b), 75,633(1976).

(7) For a recent review, see J. Shah and R. F. Lehery in "Semiconductors Probed by Ultrafast Laser Spectroscopy" edited by R. R. Alfano, Academic Press, New York,1984; pg.45.

(8) The absolute intensity at different transition energies was obtained with same excitation condition. To do this, we fixed the channel plate gain, temporal analyzer gain, prepulse intensity as well as time scale for the weakest signal (at high energy tail) to be detected. The intensity of prepusle was then treated as the standard of excitation level. As intensity increases at lower energies, neutral-density(ND) filter(s) can be placed in the luminescence path if necessary. For the curves in Fig.(5-4-2) ND filter was not used to attenuate the luminescence intensity.

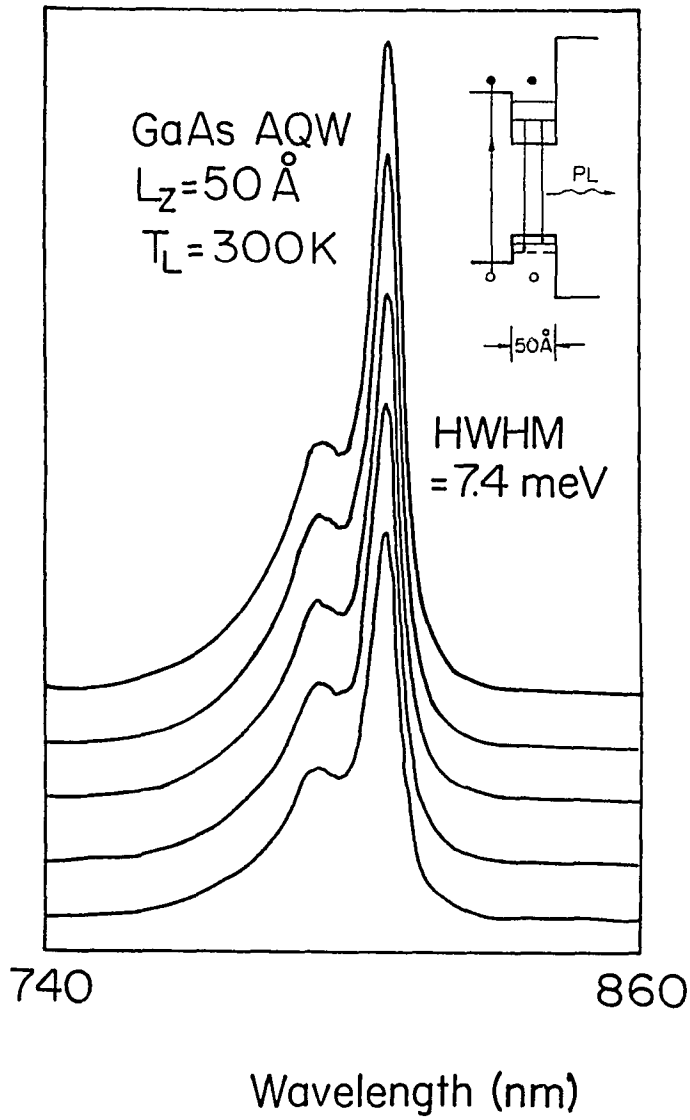

Fig.(5-2-1) Room temperature photoluminescence spectra excited by a 514.5nm line of argon ion laser. The excitation-spot size was about 400*um*. The laser power are 20.0, 22.5, 25.0, 27.5, and 30.0mW for the spectrum (a), (b), (c), (d), and (e), accordingly. Optical transitions are indicated in the inset.

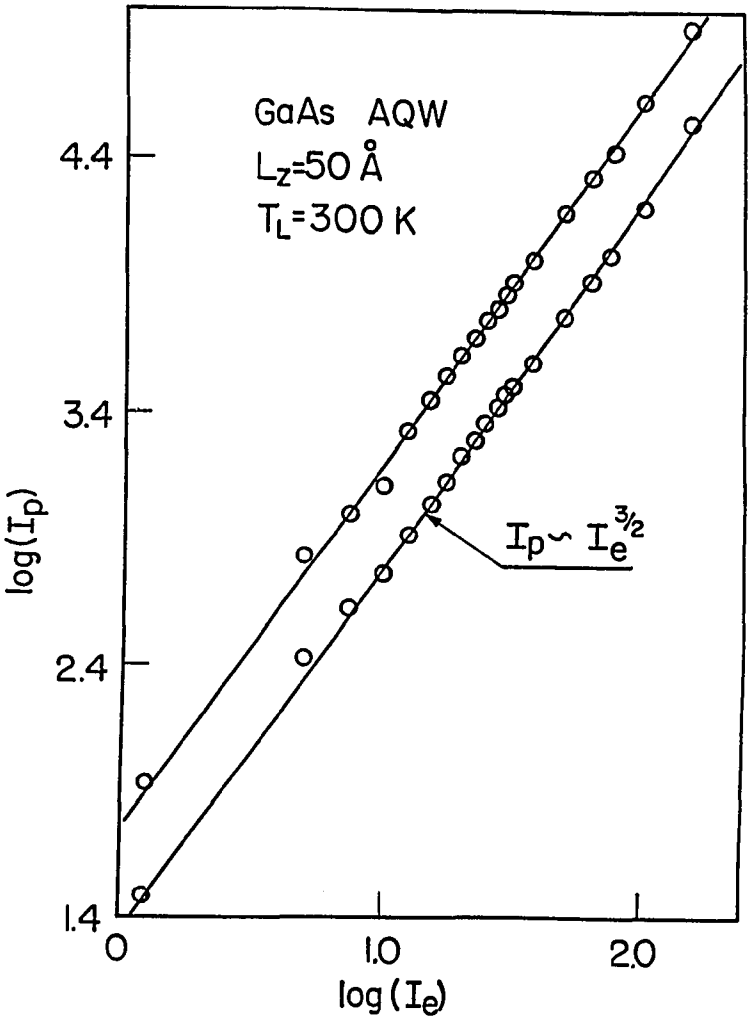

Fig.(5-2-2) The logarithm luminescence intensity (I_p) shown in Fig.(5-2-1) plotted as function of the logarithm of laser power (I_e). The upper solid line is for n=1 electron to heavy-hole transitions. The lower one is for n=1 electron to light-hole transitions. This plot shows $I_p = I_e^{3/2}$.

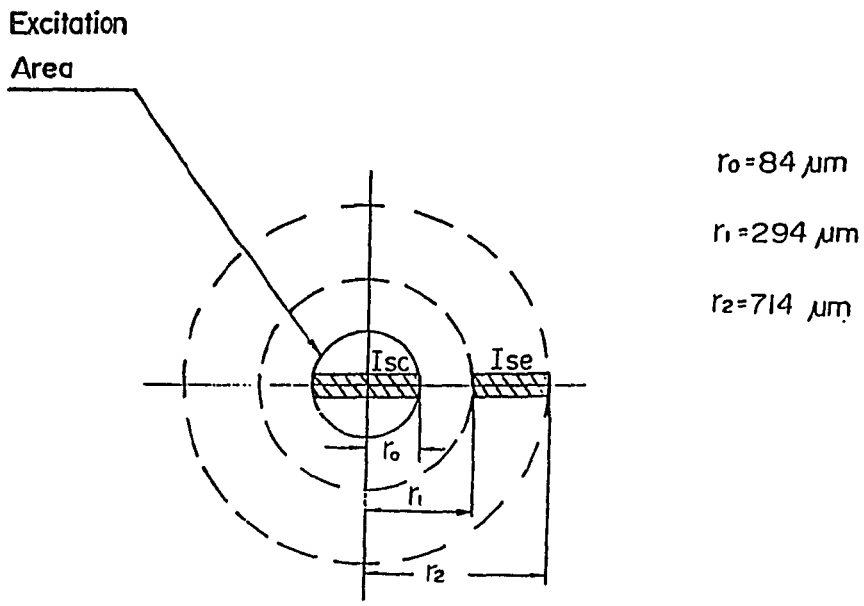

Fig.(5-3-1) A schematic diagram of photoluminescence image on the screen of the streak camera. The shaded areas are two electronic windows narrowed by the entrance slit of the camera.

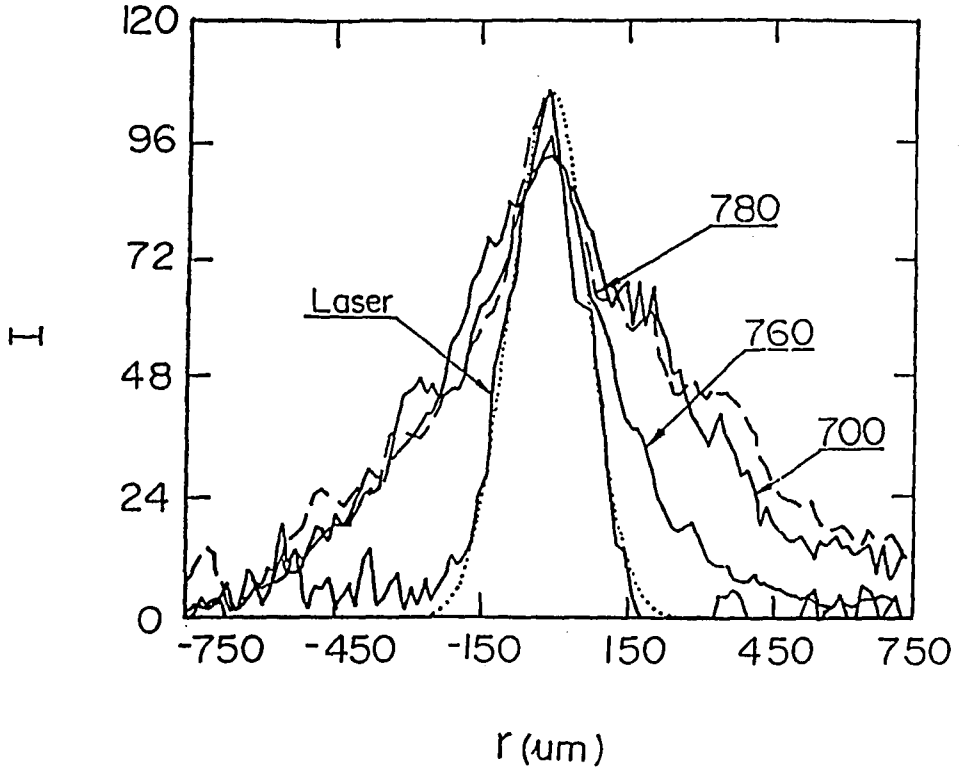

Fig.(5-4-1) Time-integrated spatial profiles of laser and the luminescence from the asymmetric well at various wavelengths at 4K. The dotted curve is the Gaussian-line fit of the laser profile by Eq.(5-4-7) which yields $a = 120um$.

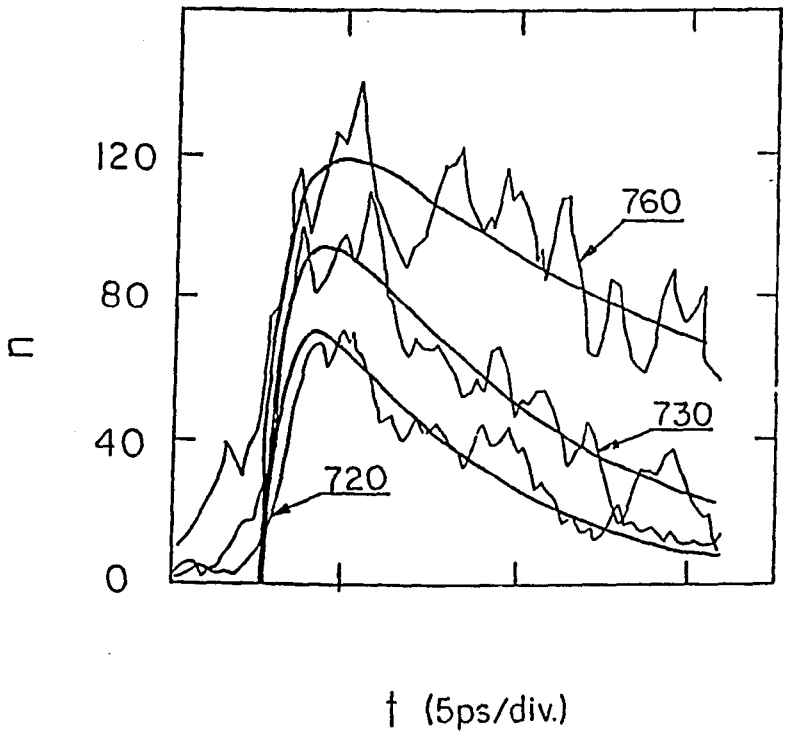

Fig.(5-4-2) Time-resolved photoluminescence (center window) from the asymmetric quantum well at 4K at various wavelengths(in nm).

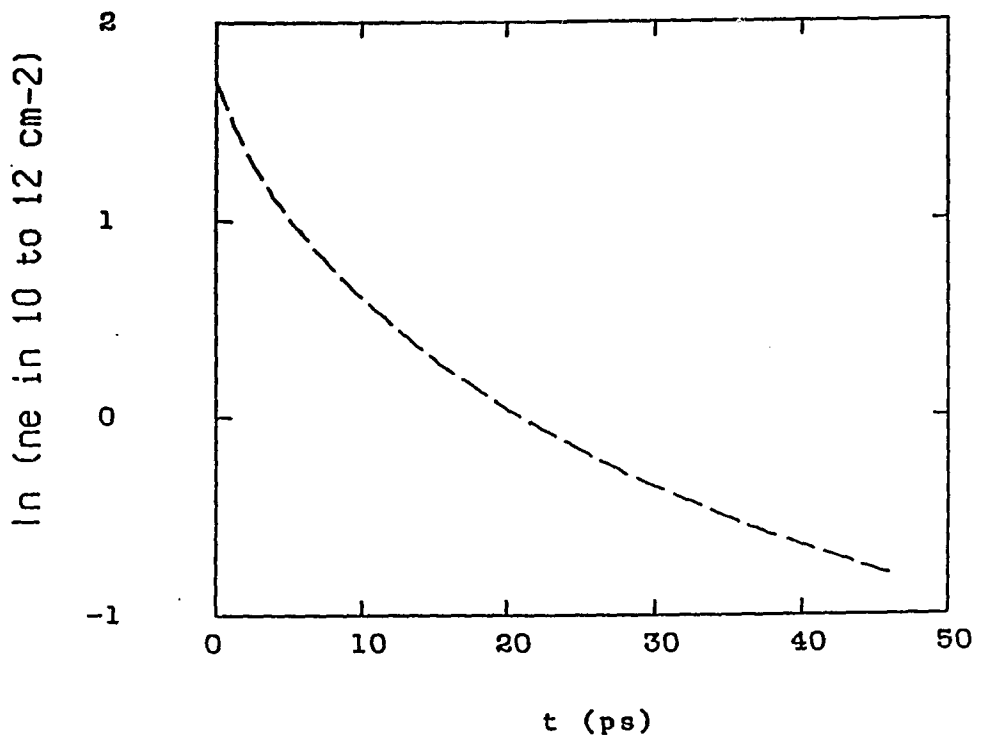

Fig.(5-4-3) The nature logarithm of electron density as function of time.

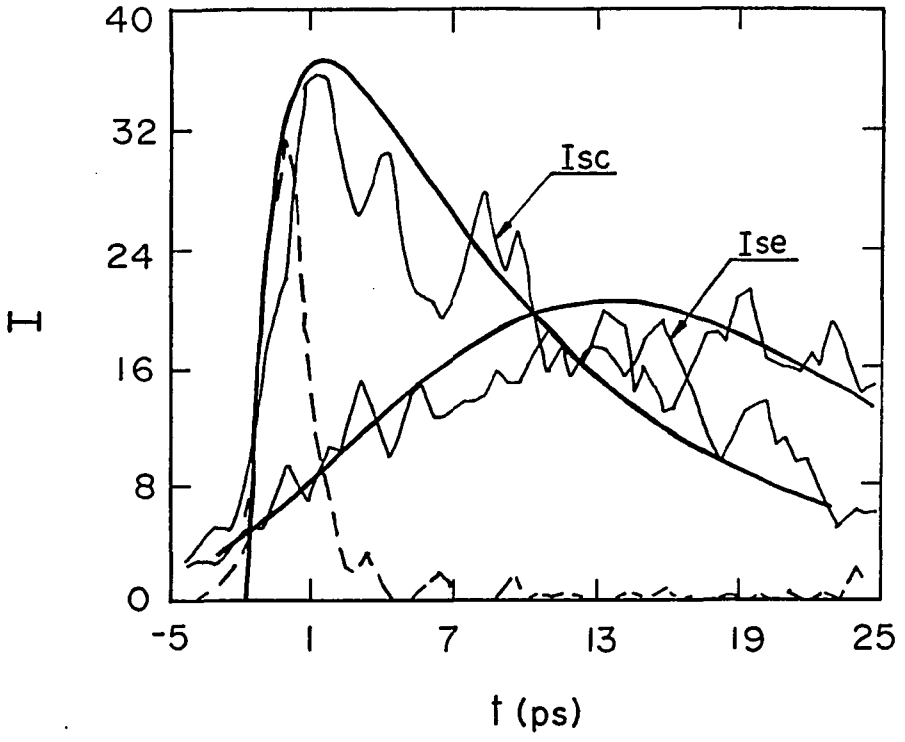

Fig.(5-4-4) Time-resolved photoluminescence of the asymmetric well at 4K from different spatial regions as distinguished by I_{sc} and I_{se}. The solid curves are the theoretical fit by using Eq.(5-4-1) and Eq.(5-4-9) for I_{sc} and I_{se}, respectively.

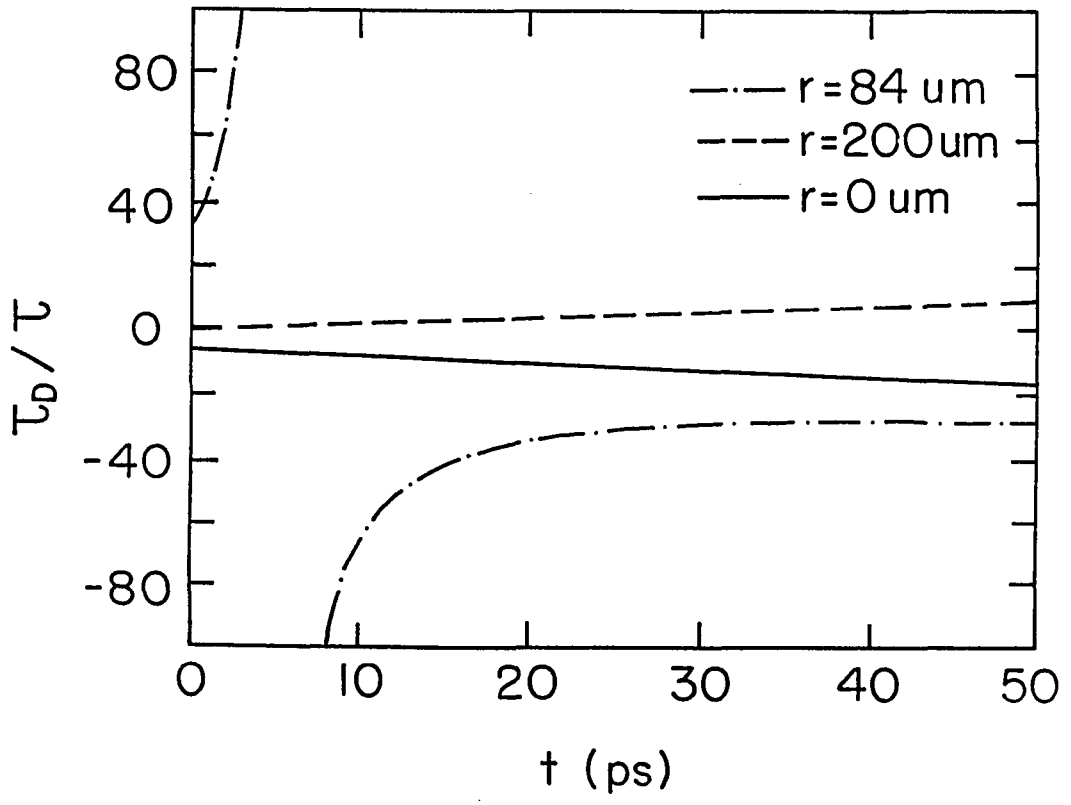

Fig.(5-4-5) The quantity of $\frac{\tau_D}{\tau}$ is plotted as function of time at given position r as indicated on each curves.

Chapter 6

Electron-Hole Recombination Dynamics in CdS_xSe_{1-x} Infinite Spherical Quantum Wells

6.1 Introduction

Recently, carriers localized in semiconductor microstructures have attracted much attention because of their potential device applications. Electrons localized in semiconductor crystallites of diameters ranging from 30Å to 800Å embedded in a transparent insulating matrix are confined in three dimensions.[1-3] Such quasi-zero-dimensional (quasi-0D) electron systems also exist in bulk alloy semiconductors due to compositional fluctuations.[4] Electronic motion in these systems no longer follow a well-defined energy-momentum relation because the Hamiltonian of the system does not commute with the momentum operator due to potential discontinuity at the crystallite surface. The physical picture of quasi-0D electron system described in section 1.2 has been experimentally verified by several groups.[1-4] Large and fast optical nonlinearities arising from photogenerated electron hole pairs have been also reported in quasi-0D electron systems.[6,7] This is very promising in device application point of view. In quasi-2D electron systems, although the optical nonlinearities originated from two-components of electron-hole plasma is very large but slow

in nanosecond time scale. The nonlinearities arising from quasi-2D excitons have very fast response time in subpicosecond time scale, however, are very small. Pioneering subnanosecond time-resolved photoluminescence(PL)[8] and picosecond pump-probe experiments[9] have also been performed. It is important to study the dynamics of various excitations in quasi-0D electron systems in detail in order to understand the physical origins underlying these various novel optical properties.

A simplified theoretical background on the electronic states in an infinite spherical quantum well is given in chapter 1. In present chapter, we report on measurements of ultrashort recombination lifetimes of the radial and angular quantum number conserved $1S \rightarrow 1S$ and $1P \rightarrow 1P$ transitions in quasi-0D electron systems in CdS_xSe_{1-x} at 4.3K using a streak camera detection system. The time-resolved PL detected at various emission energies allows us to unambiguously identify the $1S \rightarrow 1S$ and $1P \rightarrow 1P$ transitions. The recombination lifetime of $1P \rightarrow 1P$ transition was measured to be 3.5 times shorter than $1S \rightarrow 1S$ transition. The ultrafast decay of $1P$ excitation may have practical importance for the construction of ultrafast reversible optical switches. The assignment of the observed S and P transitions were supported by calculations of eigen energy levels and squared matrix element ratio for these transitions, as well as the observation of optical transitions in PL between quantized levels $1S$ and $1P$ in the conduction band and the valence band.

6.2 Experimental Method

The samples investigated were four optical glass filters Corning 2-61, 2-59,

2-58 and 2-64. The samples were mounted on a cold finger of a helium optical cryostat. The value of the x for each sample was accurately obtained from chemical analysis.[10] The picosecond experimental setup used in this research is shown in Fig.(6-2-1). A second harmonic (530nm) of a Nd-glass laser pulse of 8ps duration was used to excite the samples on the front surface. The maximum optical energy incident onto the front surface was about $40uJ$, which corresponds to 10^{14} photons per single shot. The spot size was about $8x10^{-3}$ cm^2. The exact photoexcited carrier density in quasi-0D electron system was difficult to estimate due to the complexity of surface of crystallites. However, by assuming all the photons were absorbed within $10um$, a value on the order of $10^{18}cm^{-3}$ was estimated. The PL from the samples was collected by a combination of lenses and imaged onto a $30-um$ slit of a Hamamatsu streak camera system. Various narrow-band filters centered at different wavelengths were placed in front of the streak camera to select different transition energies. Two color filters 3-67 were placed in front of the streak camera to block the light with wavelength shorter than 5400Å. The PL profiles were corrected for the nonlinearity of streak rate and spectral response of the detector. For steady-state PL experiments, an argon-ion laser, a Spex double grating spectrometer, a S-20 photomultiplier and a lock-in amplifier were used.

6.3 Time-Resolved Photoluminescence

The PL profiles in time domain were measured at different energies covering the corresponding spectral range of each sample. The expression for number of photons detected at energy E at time t is given by:[11]

$$N(E, t) = N_o [e^{-t/\tau_d(E)} - e^{-t/\tau_r(E)}], \qquad (6\text{-}3\text{-}1)$$

where E is the central energy of the narrow-band filter used; $\tau_d(E)$ and $\tau_r(E)$ are the decay and rise times of luminescence at energy E; and N_o is the proportionality constant. The value of τ_r gives information about how fast electrons and holes scatter out from initially excited states to less energetic states where they recombine while τ_d gives a measure of the recombination lifetime of various excited states when recombination dominates the depopulation of photo-excited carriers.

The time-resolved PL profiles obtained at various emission energies at 4.2K for sample 2-58 are shown in Fig.(6-3-1a) to (6-3-1e). The left curve in Fig.(6-3-1a) shows the temporal profile of exciting laser pulse which reflects the time resolution of detection system (10ps). The dotted curves in Fig.(6-3-1) are the fit to the data using Eq.(6-3-1) with a value of 12ps for the rise time τ_r. The decay times of these time-resolved luminescence profiles show only two distinct values. For emission energies ranging from 2.213 to 2.175eV and from 2.1 to 1.967eV the decay times are 29 and 100ps, respectively.

The decay time as function of emitted photon energy E for four quasi-0D electron systems at 4.2K are summarized in Fig.(6-3-2). For a comparison, the exciton lifetime vs. exciton energy in quasi-0D system in bulk $CdS_{0.53}Se_{0.47}$ alloy compound studied by Kash et al.[8] is also included in this figure. The most remarkable feature of interest in the data is the appearance of two distinct energy regions in which the decay time is different by a factor of about 3.5 for the sample 2-64, 2-58 and the bulk $CdS_{0.53}Se_{0.47}$ while the other two samples do not

show this feature because either $1P$ electron and hole were not excited or the luminescence from $1P \rightarrow 1P$ electron-hole recombination was not detected. It is expected that the decay time should be nearly invariable over the energy range of emission if only the lowest confined state $1S$ for electrons and holes are occupied. The wide spectral range most likely reflects the crystallite size distribution and the fluctuations in the value of x from crystallite to crystallite. When the two lowest states 1S and 1P are substantially occupied and the recombination lifetimes associated with these two states are considerable different, a steplike change of decay time will be observed in two distinct energy regions. The exact lifetime ratio in the two energy regions depends on the transition matrix elements. The above argument should in principle explain what we observed displayed in Fig.(6-3-2). However, the energy dependence of localized exciton lifetime in the bulk compound $CdS_{0.53}Se_{0.47}$ as displayed in Fig.(6-3-2)e also exhibits a steplike feature. The explanation given by Kash *et al.*[8] was based on the model suggested by Cohen and Sturge[5] where the exciton migration from a site with higher energy into another site with lower energy. This raises a question whether the exciton migration mechanism can apply to the present case. Since exciton migration must involve a transport over a relatively large distance due to the nature of the exciton-phonon interaction,[4] such migration may occur in relatively large crystallites. This apparently may explain the results observed in the sample 2-58 and 2-64. In smaller crystallites the migration does not occur in correspondence with the samples 2-61. However, the exciton migration picture can not explain the steplike energy dependence of lifetime as well as the ratio with the value of about 3.5 because the depth of a potential well[12] caused by compositional fluctuations are entirely random in nature. Furthermore, the exciton lifetime would be increase

monotonically with a decrease of exciton energy as recently observed for CdTe-ZnTe interfaces.[13]

A two-states ($1S$,$1P$) model is introduced here which consistently interpret all the results shown in Fig.(6-3-2) as well as other results observed by Cohen and Sturge.[4] It is possible that the excitons are confined by the potential wells in the bulk alloy compound which have two lowest states designated by $1S$ and $1P$. The exciton in higher-lying state 1P can be scattered to the lower-lying state $1S$ by emission of phonons instead of migrating from site to site. The two-state model can explain not only the results of Cohen and Sturge[4] but also our time-resolved dynamic results presented here as well as the data reported by Kash et al.[8]

In order to verify the two-states model, we have calculated the eigen energy levels of the quasi-0D electron systems and the recombination lifetime ratio for $1S \rightarrow 1S$ and $1P \rightarrow 1P$ transitions. The confinement energy for the ground states is given by

$$E_{1S} = E^{e}_{1S} + E^{h}_{1S} \qquad (6\text{-}3\text{-}2)$$

for the quasi-0D electron systems, where E^{e}_{1S} and E^{h}_{1S} are the lowest confinement energies for electrons and holes, respectively. These energies were calculated from the bulk band gaps[14] at 300K and the measured peak energies of the first derivative of room temperature reflectance ($dR / d\lambda$) by subtraction.[15] Using the electron effective mass, the isotropic hole effective mass given in Ref.4, and the measured E_{1S}, the effective diameter[16] of crystallite for each sample and eigen energies were calculated based on Eq.(2). These results are listed in Table.(6-3-1).

The spin-orbit split states[14] were neglected since they were not excited in our experiments. In Table.(6-3-1), the emitted photon energies at 4.2K for $1S \rightarrow 1S$ and $1P \rightarrow 1P$ transitions were obtained by adding corresponding confinement energies to the values of bulk gap[17] at 4.2K. The binding energies of excitons were not included. These calculated energy positions are located in Fig.(6-3-2) as arrows labeled by S and P for clarity and are in reasonable good agreement with the two-state model. Furthermore, the separation of the S and P are also in fair agreement [listed in Table.(6-3-1)].

The value of lifetime (τ_{1S}) for $1S \rightarrow 1S$ transition which is defined to be same as the decay time of the luminescence at maximum intensity is displayed in Table 1 for each sample. A value of 85ps for the $1S \rightarrow 1S$ recombination time of electrons and holes at ground states for sample 2-59 is in exact agreement with the value obtained by Warnock and Awschalom[9] using pump-probe experiment. Since the energy per pulse in our experiment is about four orders magnitude larger than they used, the Auger mechanism of carrier de-population is then ruled out in these quasi-0D electron systems. Furthermore, we did not observe the change in the lifetimes by varying the excitation intensity over a factor of 33(ND3). One concludes that the de-population of photoexcited carriers may be dominated by radiative recombination path in the present study although other radiationless transitions exist (see further discuss below). The recombination lifetimes for $1P \rightarrow 1P$ transitions denoted by τ_{1P} are also entered into Table 1. The rise times for $1S \rightarrow 1S$ and $1P \rightarrow 1P$ were not resolved by the limited time resolution $\sim 10ps$. Since the present experimental condition can not detect the $1P \rightarrow 1P$ transitions in samples 2-61 and 2-59 the numbers with $\dagger$ are the anticipated lifetimes of

$1P \rightarrow 1P$ transitions assuming the same ratio of τ_{1S} / τ_{1P} for the samples 2-58 and 2-64. Note that a value of 18ps has been also reported by Warnock and Awschalom[9] for 2-61 although they did not identify this to be the lifetime of $1P \rightarrow 1P$ transition. It should be emphasized that strongly enhanced transition probability (oscillator strength) which leads to shorten recombination lifetime of various excitations in the quasi-zero dimensional electron system is not a surprising result. The recombination enhancement due to carrier confinement in quantum well structure (quasi-two dimensional electron system) was clearly demonstrated by Gobel, Jung, Kuhl, and Ploog.[18] These authors[18] attributed their measured fast recombination lifetime to be the spontaneous carrier lifetime in quasi-two dimensional electron system. The diameter dependence of recombination lifetime in this work seem to support their arguments.[18] Our measured lifetimes are at least one order magnitude shorter than the purely radiative lifetime in the corresponding bulk implying the oscillator strengths of $1S \rightarrow 1S$ and $1P \rightarrow 1P$ optical transitions are increased due to the carrier confinement in quasi-0D electron systems.

A further test of our two-states picture is whether a reasonable good prediction of the energy positions of exciton localized in $1S$ and $1P$ states can be made for the quasi-0D electron system in the bulk compound $CdS_{0.53}Se_{0.47}$ studied by Kash et al..[8] When electrons are confined in a one-dimensional semiconductor quantum well with thickness L_z, the electron-hole recombination time for ground states may be estimated to be proportional to the L_z since the wave function is "squeezed" by the boundaries separated by L_z.[9,18] The evidence for this has already been provided by the measurements of Gobel et al..[18] Extending the above concept, the effective diameter (d) for the spherical potential well may be

estimated using a relation $\tau_{1S} = c\ d^3$. A value of about 250Å for the diameter of the potential well in the bulk was estimated using the lifetime for energies less than 2.09eV assigned by us to be the recombination lifetime for $1S \rightarrow 1S$ transition. Using this value the confinement eigen energies for exciton (electron and hole bound by their mutual Coulomb potential) were calculated. These results are also entered into Table.(6-3-1) under bulk and displayed in Fig.(6-3-2)e. The experimental results of Kash et al.[8] are in excellent agreement with our two-states model. Furthermore, when the temperature of their[8] sample was raised above 36K (3meV) the steplike feature of lifetime in two distinct energy regions disappeared. Since exciton binding energy in this material is about 20meV, the exciton dissociation is not responsible for this disappearance. However, the energy difference between ground state 1S and first excited state 1P for hole is just 3meV [Table.(6-3-1)]; therefore, the strong hole scattering between 1S and 1P states assisted by thermal energy is responsible for the absence of the two distinct regions above 36K. This temperature dependence of exciton lifetime further supports our model.

The radiative lifetime ratio for $1S \rightarrow 1S$ and $1P \rightarrow 1P$ can be predicted following the approach given by Casey and Panish[19] and Efros and Efros.[20] The matrix element for a transition from localized state in conduction band to the localized state in valence band can be expressed as:

$$M = M_b\ M_{env} \quad , \tag{6-3-3}$$

where M_b is the average matrix element for the Bloch states for bands in absence of new eigen states due to the confinement and M_{env} is the envelope part of the matrix elment which is given by:

$$M_{env} = < 1L \mid 1L > . \tag{6-3-4}$$

Since $1P$ state is a threefold degeneracy state with magnetic quantum number of -1, 0, and 1, a value of 5 for the ratio of $\mid M_{env} \mid^2_{1S-1S}$ and $\mid M_{env} \mid^2_{1P-1P}$ can be readily calculated. When the 4K recombination lifetimes are purely radiative, then the ratio for τ_{1S} / τ_{1P} should be equal to 5. The discrepancy between the predicted value of 5 and the experimentally measured value of 3.5 for τ_{1S} / τ_{1P} arises from the existence of non-radiative transitions. A simple rate equation analysis helps to substantiate the above statement. Suppose

$$\frac{1}{\tau_{1i}} = \frac{1}{\tau_{ri}} + \frac{1}{\tau_{ni}} \tag{6-3-5}$$

where $i = S$, P, $\tau_{rs(p)}$ and $\tau_{ns(p)}$ are the radiative and non-radiative recombination lifetime for $1S(P)$—$1S(P)$ transition, respectively. The ratio τ_{1S} / τ_{1P} is given by:

$$\frac{\tau_{1S}}{\tau_{1P}} = \frac{\tau_{rs}}{\tau_{rp}} \frac{\tau_{rp} + \tau_{np}}{\tau_{rs} + \tau_{ns}} , \tag{6-3-6}$$

According to Eq.(6-3-6) when $\tau_{ns} \sim \tau_{np}$ and $<< \tau_{rs}, \tau_{rp}$, then $\tau_{1S} / \tau_{1P} \sim 1$; hence, there should be only one lifetime. This is opposite to the experimental results. On the other hand, the ratio given by Eq.(6-3-6) is about 3.5 when non-radiative recombination lifetimes ($\tau_{ns} = \tau_{np}$) are about 5 times larger than the radiative lifetime τ_{rp} of the excited state $1P$ for the assumption of $\tau_{1P} \sim \tau_{rp}$ and $\tau_{1S} \sim \tau_{rs}$.

6.4 Steady-State Photoluminescence

Following the work of Warnock and Awschalom,[9] we performed steady-state PL studies at 4 and 300K to substantiate our findings from the picosecond studies. When the $1S$ and the $1P$ states are uncoupled or weakly coupled as suggested by the picosecond studies, two emission peaks arising from the $1S \rightarrow 1S$ and the $1P \rightarrow 1P$ transitions should be observed in the luminescence spectra. The energy separation between the two peaks should be approximately equal to 236meV as predicted from Eq.(1-2-14) and listed in Table.(6-3-1). In Fig.(6-4-1a), 300K PL spectra of sample 2-61 at various excitation levels (see figure caption) are plotted. The broken vertical line indicates the peak position of $dR / d\lambda$. As expected the salient feature in the luminescence spectra is the appearance of two-peak structure separated by 220meV on the high energy side of the broken vertical line. Based on the two-state model we attribute these two peaks to the $1S \rightarrow 1S$ and $1P \rightarrow 1P$ optical transitions[5] as indicated by S and P in the figure. Furthermore, at low excitation power density of $\sim 1W / cm^2$ the luminescence intensity from $1S \rightarrow 1S$ recombination is strictly linear with power density indicating that this is main recombination path. The luminescence intensity of $1P \rightarrow 1P$ recombination varies sublinearly (power 0.85) with excitation power density reflecting a weak coupling between the $1P$ and the $1S$ states.

The 4K PL spectrum of 2-61 excited by the 457.9nm line of the argon-ion laser is depicted in the Fig.(6-4-1b). As can be seen from the spectrum the position of $1S \rightarrow 1S$ peak shifts to the higher energy and its FWHM (58meV) decreases by a factor of 2 in comparison with room temperature data. The latter indicates

the broadening of $1S \rightarrow 1S$ transition at room temperature is not entirely dominated by size fluctuation of the microcrystallites under photoexcited area. The other line broadening mechanisms may also apply for the quasi-zero electron system. Assuming the broadening of $1S$ peak is dominated by the fluctuation of diameter of the microcrystallites at 4.3K. The inset of Fig.(6-3-1)b shows a spectrum fit by assuming a Gaussian shape[21] of the probability density function for the random variable d. The fit gives a mean value of 74Å for the effective diameter and a full width at half maximum of 15Å which characterizes the size fluctuation of microcrystallites. The structure next to the main $1S$ peak is from $1P \rightarrow 1P$ transition since its energy separation with $1P$ peak is about 210meV.

We have also measured 4 and 300K luminescence spectra of 2-59, 2-58, and 2-64 samples. The two-peak structure was observed for 2-59 at both 4 and 300K. The peaks were broader for 2-58 and 2-64 than for the other two samples and the $1P$ structure were not clearly identified.

After the completion of our work, we received a preprint from Dr. Hall, Corning Glass Works (to be published in J. Appl. Phys.). According to them, the wet chemical method for determining the x value from 0.4 to 0.8 was uncertain by 15% from the x-ray method. We should state that the energy peaks we measured can not be attributed to the change of the x value determined by them for a given filter number. The x values given by IBM group do not agree with the x values determined by Hall *et al.* Therefore, we conclude that each filter may not have an unique value of x even though the designated filter number may be same.

6.5 Summary

In summary, we have reported on the measurements of recombination lifetimes of $1S \rightarrow 1S$ and $1P \rightarrow 1P$ transitions in quasi-0D electron systems in CdS_xSe_{1-x}. The assignment to these observed transitions are supported by calculations of eigen energy levels and the corresponding squared matrix element ratio as well as the direct observation of optical transitions between quantized energy levels $1S$ and $1P$ in the conduction band and the valence band.

Reference

(1) R. Rossetti, S. Nakahara, and L. E. Brus J. Chem. Phys.79, 1086(1983).

(2) A. I. Ekimovand and A. A. Onushchenko, JETP Lett. 40, 1136(1984).

(3) J. Warnock and D. D. Awschalom, Phys. Rev. B 32, 5529(1985).

(4) L. E. Brus, J. of IEEE QE-22, 1909(1986).

(5) E. Cohen and M. D. Sturge, Phys. Rev. B 25, 3828(1982)

(6) R. K. Jain and R. C. Lind, J. Opt. Soc. Am. 73, 647(1983).

(7) S. S. Yao, C. Karaguleff, A. Gabel, R. Fortenberry, C. T. Seaton, and G. I. Stegeman, Appl. Phys. Lett. 46, 801(1985).

(8) J. A. Kash, A. Ron and E. Cohen, Phys. Rev. B, 28, 6147(1983).

(9) J. Warnock and D. D. Awschalom, Appl. Phys. Lett. 48, 425(1986).

(10) The samples were sent to Schwarzkopf Microanalytical Laboratory, Inc. (56-19 37th Ave. Woodside, NY 11377) for chemical wet analysis to obtain accurate x-values. Analysis was made by technical director Dr. Edmund Petro.

(11) P. Y. Lu, Z. X. Yu, R. R. Alfano, and J. I. Gersten, Phys. Rev.A 26, 3610(1982).

(12) The eigenvalue problem in such a well may be best approximated by three dimensional harmonic oscillators model. For large radius well (> 100 A), the difference in eigen energy for the two lowest states calculated using the harmonic oscillator model and a spherical well model is negligible. The degeneracy for the first excited state 1P is also same for the two model.

(13) Y.Hefetz, D. Lee, A. V. Nurmikko, S. Sivananthan, X. Chu, and J. -P. Faurie, Phys. Rev. B 34, 4423(1986).

(14) F. L. Pedrotti and D. C. Reydold, Phys. Rev.127, 1584(1962).

(15) The first derivative of room temperature reflectance were measured in a Perkin Elmer Lambda 9 spectrometer.

(16) Our calculated values of effective diameter are consistently smaller than the values reported by Wornock and Awschalom.[9] This discrepancy may caused by the complexity of boundary between semiconductor and glass. The value of effective diameter for the sample 2-61 calculated by us is, however, in exact agreement with calculated by Warnock and Awschalom.[9] Note that the value of x they used for this sample is same as we measured.

(17) D. W. Langer, Y. S. Park, and P. N. Euwema, Phys. Rev.152, 788(1966).

(18) E. O. Gobel, H. Jung, J. Kule, K. Ploog, Phys. Rev. Lett. 51, 1588(1983). The recombination lifetime of electron and hole within quantum well decreases with L_z from 1ns for $L_z = 14nm$ to 350ps for $L_z = 5nm$.

(19) H. C. Casey, Jr. and M. B. Panish, "Heterostructure Lasers" (Acadamic Press, New York, 1978), P.144.

(20) Al. L. Efros, and A. L. Efros, Sov. Phys. Semicond., 16, (772)1982.

(21) Kai Shum, P. P. Ho, R. R. Alfano, D. F. Welch, G. W. Wicks, and L. F. Eastman, IEEE Journal of quantum electronics, QE-22, 1811(1986).

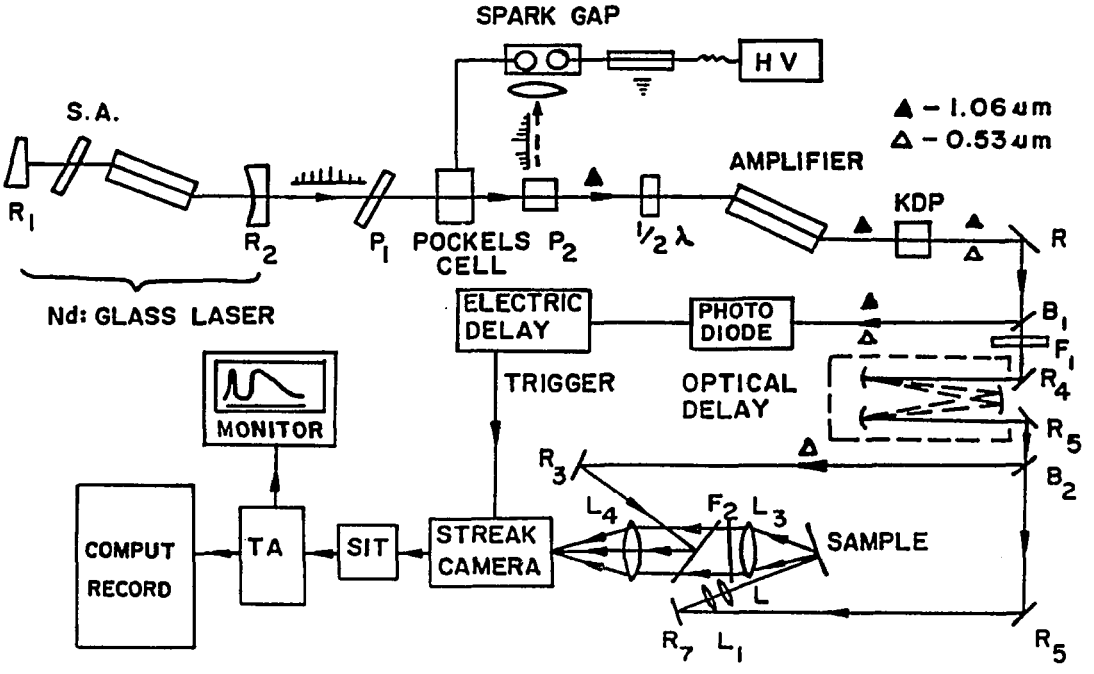

Fig.(6-2-1) The experimental setup for time-resolved photoluminescence with 10ps time resolution.

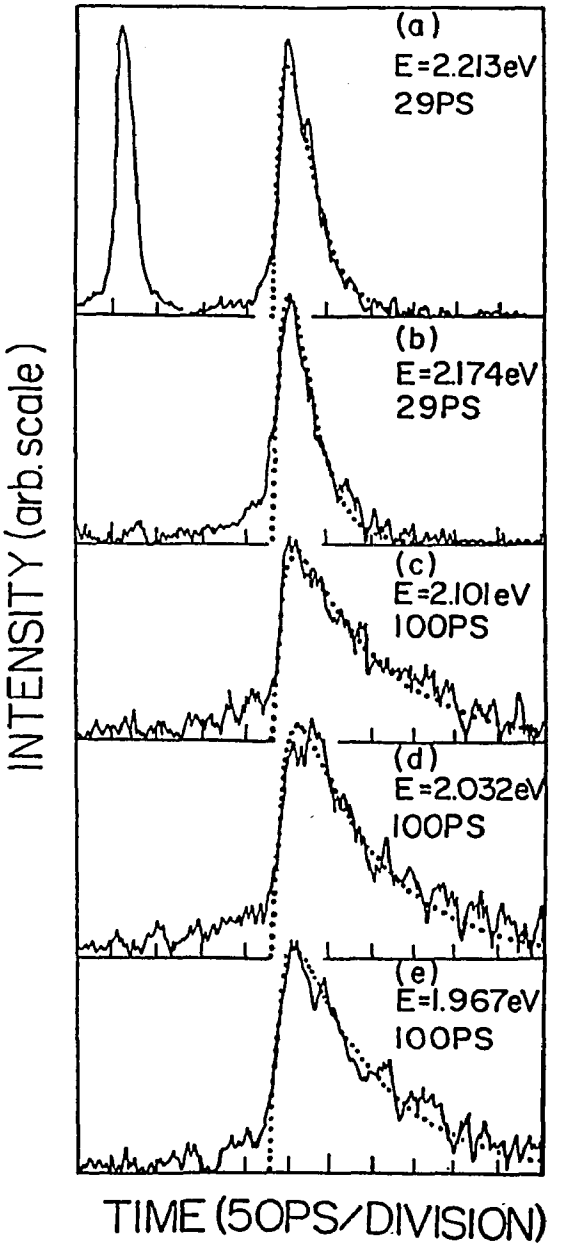

Fig.(6-3-1) Time-resolved PL profiles detected at different energies (a to e) for the sample 2-58 at 4.2K. The dotted curves are the theoretical fit with 12 ps for rise time and decay times are indicated on the corresponding profiles. The left curve of (a) is the temporal response profile to the laser pulse used to excite the samples.

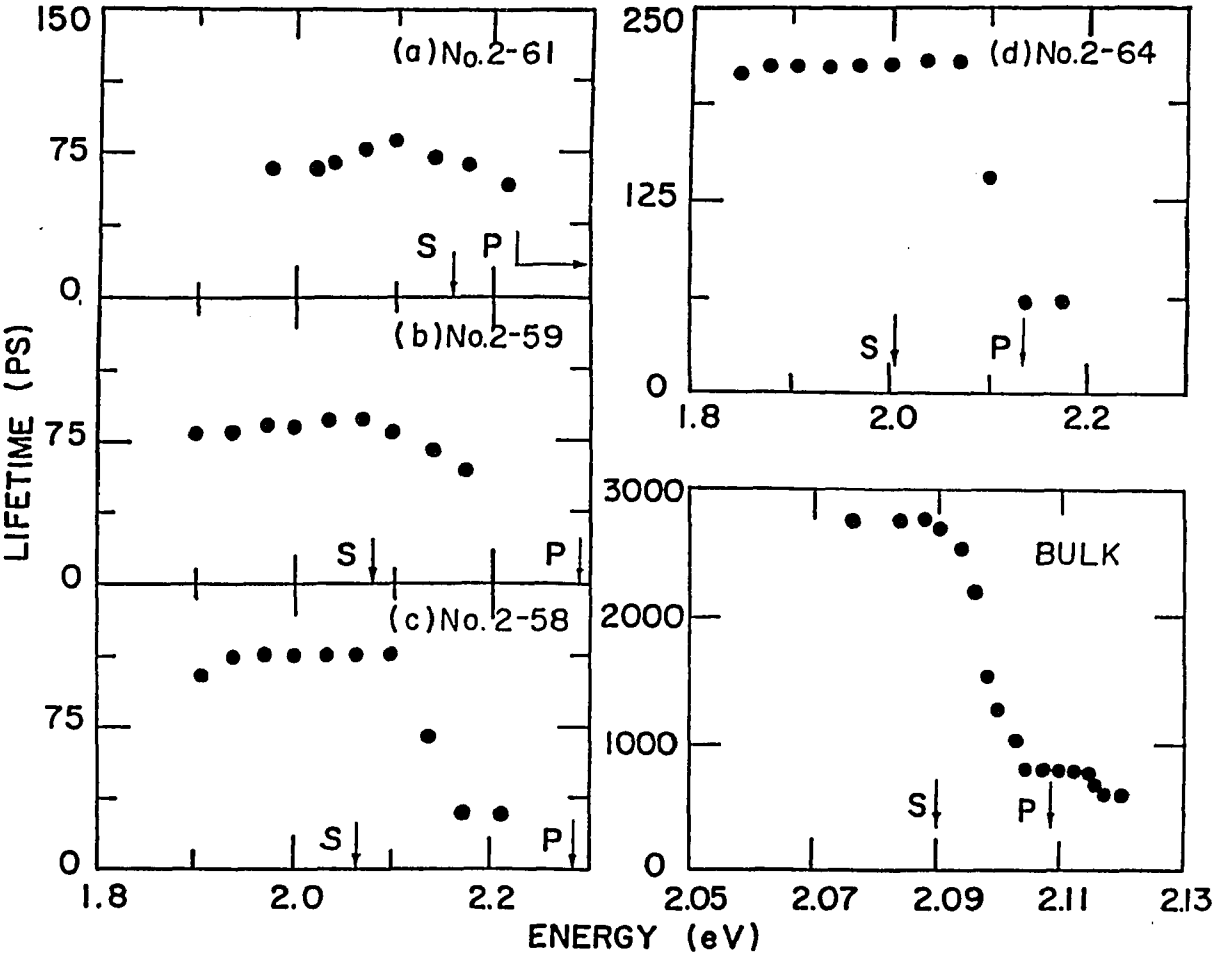

Fig.(6-3-2) The lifetimes are plotted as function of emitted photon energy. The sample temperature for (a), (b), (c), (d) is 4,2K and for (e) is 2K. The arrows indicated the energy positions for $1S \rightarrow 1S$ transition (S) and $1P \rightarrow 1P$ transition (P).

6-3-1 The measured energy peak of first derivative of reflection at 300K, bulk energy gaps at 4.2K and 300K, the calculated confinement energies, emission energies for 1S → 1S and 1P → 1P transitions and effective diameters (d), the measured lifetimes for 1S → 1S and 1P → 1P transitions as well as their ratio are displayed.

Sample CdS_xSe_{1-x}			(300 K) Energy peak for $dR/d\lambda$ eV	(300 K) Bulk gap[b] eV	Confined energy (meV)					4K emission energy[b] eV		θ	4K lifetime psec		τ_{1S}/τ_{1P}
No.	x	d			$E^e_{1S}+E^h_{1S}$	E^e_{1S}	E^h_{1S}	E^e_{1P}	E^h_{1P}	1S→1S	1P→1P	ΔE_{S_P}	1S	1P	
2-61	0.27	74A	2.0120	1.7857	226	187	39	382	80	2.156	2.392	220	70	20†	3.5
2-59	0.121	80A	1.9366	1.7333	203	168	35	344	72	2.078	2.291	224	85	24†	3.5
2-58	0.081	80A	1.9245	1.7143	210	174	36	356	74	2.065	2.284	*	100	29	3.5
2-64	0.168	102A	1.8666	1.7429	124	103	21	211	43	2.004	2.134	*	210	60	3.5
Bulk	0.530	250A		1.9368	17	14	3	29	6	2.090	2.108		2750	790	3.5

a from ref. 14
b the value of bulk gap is from ref. 17
* peaks are broad and unresolved.
θ measured energy separation (meV) between S and P peaks at 300K from Fig. 3a.
† the anticipated values assuming a same ratio τ_{1S}/τ_{1P} for the samples 2-58 and 2-64.

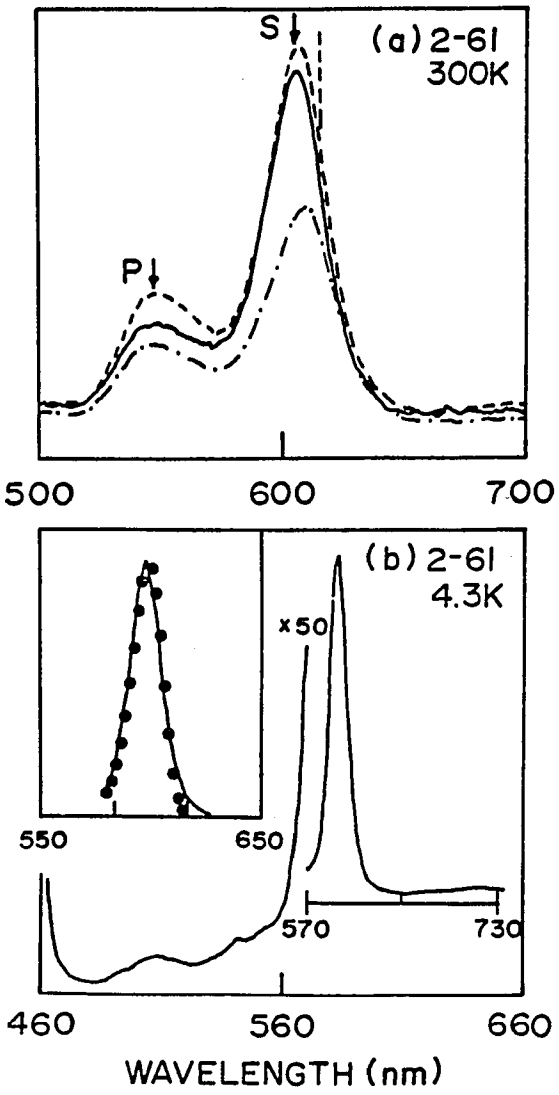

Fig.(6-4-1) (a) Photoluminescence spectra of sample 2-61 at various excitation levels taken at room temperature using 488nm line of Argon-ion laser. The excitation levels (intensity scale) were 2.5 (2) and 10 (10) times higher for the

broken curve and dot-dashed curve than the solid curve, respectively. The broken vertical line indicates the peak position of the first derivative of reflectance at room temperature. S and P stand for the $1S \rightarrow 1S$ and $1P \rightarrow 1P$ transitions, respectively. (b) Photoluminescence spectra of 2-61 at 4.3K. The inset shows that the $1S$ peak broadening is dominated by the diameter fluctuation of microcrystallites. The solid dots is calculated by assuming a Gaussian shape of the probability density function for the random variable d with a variance of $25\mathring{A}^2$.

Chapter 7

Future Directions

The following section describe research programs and questions to be addressed which my work suggests to be investigated.

7.1 Band Offset Determination

Future investigation on the determination of band offset at the interface of two different semiconductor using the model developed in this thesis is to systematically measure the ΔE as function of well thickness L_z from 10 to 80Å. In order to test which set of boundary conditions should be used in the model, each data point should be taken by varying one monolayer of the well thickness.

7.2 Nonequilibrium Phonon

Form experimental point of view, we have demonstrated the nonequilibrium effects on the energy relaxation of hot-carriers and on the carrier density decay. Theoretical studies for the former have been recently carried out by several groups. One should theoretically assess the importance of nonequilibrium phonon enhanced phonon replica emission on reducing the carrier density within the lifetime of nonequilibrium phonons. This mechanism opens a new channel in reduc-

ing the initial carrier lifetime and should have a future application in making ultrafast optical devices.

7.3 Carrier Re-distribution

Suppose the excess energies of photogenerated carriers are distributed among the electron, heavy-hole, and light-hole such that at $t = 0$ the electrons reach a temperature $T_e = 3600K$, heavy-hole reach a temperature $T_{hh} = 650K$, and light-holes reach a temperature $T_{lh} = 1800K$ though carrier-carrier collisions. About 5ps later, the electrons, heavy-holes, and light-holes approach a same carrier temperature $T_c = 1000K$ due to interband carrier collisions if carrier density is high enough. In the future research, one should able to monitor this initial carrier re-distribution process by adopting a three-temperature model (T_e, T_{hh} T_{lh}).

7.4 Carrier Diffusion

Future research on carrier diffusion in quantum well structures should investigate the roles of internal pressure of electron-hole gas, nonequilibrium phonons emitted by hot-electrons, and the potential well profiles in the carrier diffusion in lateral x-y plane of quantum wells. The carrier diffusion in z-direction via virtual states above the barriers should be investigated.

7.5 Quasi-0D Excitons

We have experimentally shown quantized eigen states of $1S$ ans $1P$ for both electrons in conduction band and holes in valence band in CdSSe microcrystallites embedded in transparent matrix. The electron-hole recombination lifetime for $1P \rightarrow 1P$ has been measured to be 3.5 times shorter than for $1S \rightarrow 1S$. In our analysis the coulomb interaction between electron and hole was neglected. Future research should include the quasi-0D excitonic effects on the carrier dynamics in quasi-0D electron system. Another aspect of the future research in the field is to investigate directly (1) which excitation ($1S$,$1P$,$1D$) has larger and faster optical nonlinearities, and (2) the effects of eigen state degeneracy and wave function on the contributing to the optical nonlinearities.

7.6 External Field

Since the most of electro-optic and transport devices based on the semiconductor quantum well operate under external electric field, the future study on ultrafast photogenerated carrier dynamics in these material should investigate the effects of external field.

Appendix 1

```
c     This program is to calculate the eigen energy using Bastard
c     model when b=mew/meb. The program can be also used
c     to caculate eigen energy using conventional and
c     χ normality boundary conditions by chang b to 1/b.
c     where mew and meb are the effective masses in well
c     and in barrier, respectively,
c     a=10mew, er=band offset in meV.

      read(*,*) a,b,er
      a0=5.11
      x=0.0
300   x=x+0.01
      y=0.0
90    y=y+0.001
      u=sqrt(b)*sqrt(1.0-y*y)
      es=u-y*tan(a0*x*y*sqrt(a*er/100.0))
c     write(*,*) y,es,u
      if((te1/es).lt.0.0) goto 200
      ty=y
      te1=es
      goto 90
200   aw=0.5*(ty+y)
      r1=aw*aw*er
      t=200.0*x
      write(*,*) t,r1
      if(x.gt.0.99) stop
      goto 300
      end
```

Appendix 2

```
c     This program is used to calculate the eigen energy values
c     in a finite potential well using new wave function
c     connection rules discussed in chapter 2.
c     The means of a, b, er are same as A1, ed represents
c     alumi. percentage, i.e., x-value.

      read(*,*) a,b,ed,er
      bc=1519.0/(1519.0+1247.0*ed)
      a0=5.11
      x=0.0
300   x=x+0.01
      y=0.0
90    y=y+0.001
      p1=asin(0.29*y*sqrt(a*er/100.)*(1.-y*y*er/1519.))
      s1=0.29*sqrt(1.-y*y)*sqrt(b*er/100.)*(1.-(1.-y*y)*er/1519.)
      b1=alog(s1+sqrt(s1*s1+1.0))
      t1=(b1*sqrt(b*(1.-y*y))/(p1*y*sqrt(a)))*(sin(p1)/sinh(b1))**2
      u=t1*sqrt(bc)*sqrt(1.0-y*y)
      es=u-y*tan(a0*x*y*sqrt(a*er/100.0))
      if((te1/es).lt.0.0) goto 200
      ty=y
      te1=es
      goto 90
200   aw=0.5*(ty+y)
      r1=aw*aw*er
      t=200.0*x
      write(*,*) t,r1
      if(x.gt.0.99) stop
      goto 300
      end
```

Appendix 3

```
c       This program is to calculate total phonon emission
c       rate as function of initial electron energy given by Eq.(3-2-14).

c       the main program
c     implicit double precision (a-h,o-z)
        external func
      common o
           open(11,file='wek-tt')
      o=1.0001
      zu=acos(sqrt(1./o))
      zup=zu-1.0e-3
      res=ste(1.0e-4,zup,2.0e-2,func)
        write(11,30) o,res
30      format(1x,2f12.5)
      close(11)
        end


        function ste(c,d,rer,func)
c     implicit double precision (a-h,o-z)
        external func
      h=(d-c)/20.
      n=20
      ends=func(c)+func(d)
      two=0.
      four=func(c+0.5*h)
      t=c
      do 3 i=1,n-1
      two=two+func(t+h)
      four=four+func(t+1.5*h)
 3      t=t+h
      old=h/6.0*(ends+4.0*four+2.*two)
 4    h=h/2.0
      two=two+four
      four=0.0
      n=2*n
      t=c+h/2.
      four=func(t)

      do 5 i=1,n-1
      four=four+func(t)
 5    t=t+h

      ste=h/6.0*(ends+2.0*two+4.0*four)
```

```
c          write(6,333)h,old,ste
333   format(1x,'h='f9.4,1x,'old='f9.4,1x,'ste='f9.4)
      if (abs(ste-old).lt.(abs(rer*old))) return
      old=ste
      go to 4
      end

c     the func(z) program
      function func(z)
c       implicit double precision (a-h,o-z)
      external f,y1,y2
      func=simp2(-10.0,10.0,y1,y2,f,z,2,2,2.0e-2)
      return
      end

      function f(x,y,z)
c     implicit double precision (a-h,o-z)
c     Here o is the normalized electron energy(Ek/Elo)
c     relative to subband edge. f22 comes from the form factor
c     in z-direction. g is the probability density for qz.
c     The rest are from the Frohlich interaction Haomitonian.
c     zl is a parameter for well width.

c     implicit double precision (a-h,o-z)
      common o
      pi=3.1415926
      zl=1.0
      f5=(cos((x+y)*zl/2.))**2
      f6=(1.-((x+y)*zl/pi)**2)**2
      if (abs(f6).le.1.0e-2) then
         f66=pi*pi/16.
      else
         f66=f5/f6
      endif
      f7=zl*(cos(zl*y/2.))**2
      f8=(1.-(zl*y/3.14)**2)**2
      if (abs(f8).le.1.0e-2) then
         f88=pi*pi/16.*zl
      else
         f88=f7/f8
      endif
      g=f66*f88
      f2=(1.-(x*zl/(pi*2.0))**2)**2
      f3=(sin(x*zl/2.))**2
      f4=(x*zl/2.)**2
      if (abs(f2).le.1.0e-2) then
         f22=pi*pi/4./f4
      else if (abs(f4).le.1.0e-2) then
         f22=1./f2
```

```
      else
          f22=f3/f2/f4
      endif
      q1=(cos(z))*sqrt(o)-sqrt(o*(cos(z))*(cos(z))-1.)
      q2=(cos(z))*sqrt(o)+sqrt(o*(cos(z))*(cos(z))-1.)
      r1=1./sqrt((cos(z))*(cos(z))-1./o)-1.
      r2=1./sqrt((cos(z))*(cos(z))-1./o)+1.
      f=0.1*g*1.0*(r1/(q1**2+x**2)+r2/(q2**2+x**2))
      return
      end

      function y1(x)
c     implicit double precision (a-h,o-z)
      y1=-10.0
      return
      end

      function y2(x)
c     implicit double precision (a-h,o-z)
      y2=10.0
      return
      end


c     computation subprogram
      function simp2(a,b,y1,y2,f,z,nx,ny,eps)
c     implicit double precision (a-h,o-z)
      external f,y1,y2
      logical p,q
        common /log/p,q
      mx=nx
      my=ny
      hx=(b-a)/float(mx)
      dmy=1.0/float(my)
      p=.true.
      go to 20
 50   r1=w*hx/6.0
      rp=wp
      p=.false.
 15   mx=mx+mx
      my=my+my
      hx=hx*0.5
      dmy=dmy*0.5
 20   w=0.0
      wp=0.0
      q=.false.
      k=1
      x=b
      do 1 i=1,2
```

```
      call fu(x,my,dmy,y1,y2,f,z,w,wp,rp,r2)
1     x=a
      w=0.5*w
      wp=0.5*wp
      if (mx.eq.1) go to 30
      k=2
      do 2 i=2,mx
      x=x+hx
      call fu(x,my,dmy,y1,y2,f,z,w,wp,rp,r2)
2     continue
30    w=0.5*w
      q=.true.
      k=3
      x=a-0.5*hx
      do 3 i=1,mx
      x=x+hx
      call fu(x,my,dmy,y1,y2,f,z,w,wp,rp,r2)
3     continue
      w=4.0*w
      wp=2.0*wp
      if (p) go to 50
      r2=(rp*0.5+w)*hx/6.0
c     write(6,*)z,r1,r2
      err=r2-r1
c     if(abs(r2) .ge. 1.0) err=err/(abs(r2)+abs(r1))
      if(abs(err/r1)-eps)  55,60,60
55    simp2=r2
      return
60    r1=r2
      rp=rp*0.5+wp
      go to 15
      end

      subroutine fu(x,my,dmy,y1,y2,f,z,w,wp,rp,r2)
      logical p,q
      common /log/p,q
      external f,y1,y2
100   y1x=y1(x)
      y2x=y2(x)
      hy=(y2x-y1x)*dmy
      s1=0.0
      y=y1x-0.5*hy
      do 105 j=1,my
      y=y+hy
105   s1=f(x,y,z)+s1
      s2=s1
      if (.not.(p.or.q)) go to 150
      s2=0.5*(f(x,y1x,z)+f(x,y2x,z))+s2
      if (my.eq.1) go to 150
```

```
      do 110 j=2,my
      y1x=y1x+hy
  110 s2=f(x,y1x,z)+s2
  150 w=w+hy*(s1+s2)/3.0
      wp=wp+hy*s2/3.0
      return
      end
```

Appendix 4

```
c     This program calculates photoluminescence spectra of
c     GaInAs single quantum wells taking into account
c     the well width fluctuations and finite carrier temperatures.
c     The expression is given by Eq.(3-3-10).

      external f
        dimension e,bb
        character*10 file1
        common/pad/zzf,zff,zf,bbf,bf,alp,bbb,c,ee,z,eh,xx,y,w
        common/pass/ctk,efe,efh,aa,e1,e1h,al,cof
        common/aik/e
1       write(6,10)
10      format(1x,'enter aa,e1,e1h,al')
        read(5,12)aa,e1,e1h,al
12      format(4f9.4)
11      write(6,13)
13      format(1x,'enter ctk,efe,efh,cof')
        read(5,14)ctk,efe,efh,cof
14      format(4f9.4)
        write(6,31)
31      format(1x,'enter PL')
        read(5,32)file1
32      format(a10)
        open(17,file=file1)
      do 3 i=1,90
        e=845.0+0.5*i
        a=840.0
        b=e
      bb=call(f,a,b)
        write(17,34)e,bb
34      format(1pe12.5x,e12.5)
3     continue
        close(17)
        go to 1
        end
      function f(x)
        common/pad/zzf,zff,zf,bbf,bf,alp,bbb,c,ee,z,eh,xx,y,w
        common/pass/ctk,efe,efh,aa,e1,e1h,al,cof
        common/aik/e
        zzf=(e1/(x-810.0-e1h))**(1/al)
        zff=0.5*(aa**2.)*((zzf-1)**2.0)
        zf=exp(-zff)
        bbf=(0.4*aa/al)*(e1**(1/al))
        bf=bbf/((x-810.0-e1h)**((1+al)/al))
```

```
   alp=e-x
   bbb=810.0*(1+0.093)+2.0*alp
   c=alp**2.0+810.0*alp
   ee=0.55*(bbb-sqrt(bbb**2.0-3.63*c))
   z=1.0/(1.0+exp((ee-efe)/ctk))
   eh=alp-ee
   xx=(1.+ee/810.0)
   y=(1.0+eh/810.0)
   w=1.0/(1.0+exp((eh-efh)/ctk))
   f=cof*zf*bf*xx*y*z*w
return
end
```

Appendix 5

```
c     This program is used to calculate theoretical c     photoluminescence intensity
as function of time c     at various emission eneries c     using carrier temperature
and quasi-Fermi-energy c     as two parameters. The exact expression is given
c     by Eq.(4-4-1).

      dimension ttt(106),tt(106),s(106)
      character*10 file1
 1    write(6,37)
 37   format(1x,'enter temp. pra.= tf,tb,ts,tm, h')
      read(5,39)tf,tb,ts,tm,h
 39   format(5f9.4)
      write(6,72)
 72   format(1x,'enter u0=Fermi-energy, ei=tra.enery, td,tr and c')
      read(5,74)u0,ei,td,tr,c
 74   format(5f9.4)
      x=0.86*(ei-1609.6)
      xx=0.14*(ei-1609.6)
      a=0.56*(ei-1629.6)
      aa=0.44*(ei-1609.6)
      write(6,70)
 70   format(1x,'enter ch# where you wish to start to fit')
      read(5,901)n
 901  format(i2)
      t=0.
      tc=0.0287*tm*(exp(-t/tf)+exp(-t/tb)+exp(-t/ts))+8.6
      ue=u0*exp(-t/td)
      u1=exp(0.1367*log(1.+exp(ue/tc)))
      uh=tc*log(u1-1.)
      fx=1./(exp((x-ue)/tc)+1.)
      z=(1.+x/ei)*(1.+xx/ei)*fx*(1./(exp((xx-uh)/tc)+1.))
      fy=1./(exp((a-ue)/tc)+1.)
      zz=(1.+a/ei)*(1.+aa/ei)*fy*(1./(exp((aa-uh)/tc)+1.))
      do 143 i=n,106
      ttt(i)=0.44*float(i-n)
      s(i)=1000.0*c*(1.-exp(-ttt(i)/tr))*(0.019*z+h*0.0018*zz)
 143  continue
      write(6,55)
 55   format(1x,'enter theo-data name')
      read(5,45)file1
 45   format(a10)
      open(17,file=file1)
      do 300 i=1,106
      tt(i)=0.44*float(i)
      write(17,200)tt(i),s(i)
```

```
200   format(2f9.4)
300   continue
      go to 1
      end
```

Appendix 6

```
c     This program is used to calculate carrier energy
c     loss rates defined by Eq.(4-4-6).

      external g
      external f
      character*10 file1
      common/kai/tck,uh
      write(6,21)
21    format(1x'enter name of inte. valuh')
      read(5,22)file1
22    format(a10)
      open(17,file=file1)
      do 760 i=1,106
      t=0.44*float(i-1)
      tck=66.0*(exp(-t/2.)+exp(-t/5.0)+exp(-t/30.0))+8.6
      ue=100.0*exp(-t/10.0)
      uh=tck*log((exp(0.14*log(1.+exp(ue/tck))))-1.)
      call kaig(g,0.,500.,1.0e-5,1.0e-5,rintt)
      call kaif(f,0.,500.,1.0e-5,1.0e-5,ret)
      aa=ret
      bb=rintt
      y=aa/bb
      write(6,*)bb,aa
      write(17,120)tck,y
120   format(e12.5,3x,e12.5)
760   continue
      end

      function g(x)
      common/kai/tck,uh
      d=exp((x-uh)/tck)
c     g=(x-uh)*d*0.08617/(tck*tck*(d+1.0)*(d+1.0))
      g=1./(d+1.)
      return
      end

      function f(x)
      common/kai/tck,uh
      b=exp((x-uh)/tck)
      f=x/(b+1.)
      return
      end


      subroutine kaig(g,a,b,rer,aer,rintt)
```

```
      external g
      h=(b-a)/2.0
      n=1
      two=0.0
      ends=g(a)+g(b)
      four=g(a+h)
      old=h/3.0*(ends+4.0*four)
4     h=h/2.0
      two=two+four
      four=0.0
      n=2*n
      t=a+h

      do 5 i=1,n
      four=four+g(t)
5     t=t+h+h

      rintt=h/3.0*(ends+2.0*two+4.0*four)
      if (abs(rintt-old).lt.(abs(rer*rintt)+abs(aer))) return
      old=rintt
      go to 4
      end


      subroutine kaif(f,a,b,rer,aer,ret)
      external f
      h=(b-a)/2.0
      n=1
      two=0.0
      ends=f(a)+f(b)
      four=f(a+h)
      old=h/3.0*(ends+4.0*four)
4     h=h/2.0
      two=two+four
      four=0.0
      n=2*n
      t=a+h

      do 5 i=1,n
      four=four+f(t)
5     t=t+h+h

      ret=h/3.0*(ends+2.0*two+4.0*four)
      if (abs(ret-old).lt.(abs(rer*ret)+abs(aer))) return
      old=ret
      go to 4
      end
```

Appendix 7

```
c       This program is to calculate carrier densities
c     as function of time. The expressions are given by
c     Eqs.(4-4-9), (4-4-10), and (4-4-11).

      external f
      character*10 file1
        common/aaa/tck,ue
      write(6,21)
21    format(1x'enter name of inte. value')
      read(5,22)file1
22    format(a10)
      open(17,file=file1)
        do 760 i=1,106
        t=1.415*float(i-1)
        tc=0.33*2300.*((exp(-t/2.))+(exp(-t/30.))+(exp(-t/5.)))
        ue=100.0*exp(-t/10.)
        tck=0.08617*(tc+100.)
c       uh=tck*log((exp(0.14*log(1.+exp(ue/tck))))-1.)
      con=call(f,0.,1000.)
        re=log(0.01*con)
      write(17,120)t,re
120     format(e12.5,3x,e12.5)
760   continue
      end


      function f(x)
      common/aaa/tck,ue
      f=2.79/(1.+exp((x-ue)/tck))
      return
      end
```

Appendix 8

```
c     This program calculates Eq.(6-3-1).

      dimension y(106),tt(106),z(106),t(106)
      character*10 file1
1     write(6,30)
30    format(1x,'enter data name')
      read(5,35)file1
35    format(a10)
      open(17,file=file1)
      read(17,*) (y(i),i=1,106)
      close(17)
500   write(6,37)
37    format(1x,'enter a,tr,td')
      read(5,39)a,tr,td
39    format(3f9.4)
      write(6,70)
70    format(1x,'enter ch# where you wish to start to fit')
      read(5,72)n
72    format(i2)
      do 143 i=1,106
      t(i)=0.44*float(i-n)
      tt(i)=0.44*float(i)
      z(i)=a*(1.-exp(-t(i)/tr))*(exp(-t(i)/td))
143   continue
      do 400 i=1,106
      d=0.
      d=d+(z(i)-y(i))**2.
400   continue
      write(6,405)d
405   format(f9.4)
      write(6,410)
410   format(1x,'do you want fit agin? yes(1), no(2)')
      read(5,420)k
420   format(i1)
      if (k.eq.1) then
      go to 500
      end if
      if (c.eq.2) then
      go to 600
      end if
600   write(6,55)
55    format(1x,'enter theo-data name')
      read(5,45)file1
45    format(a10)
```

```
      open(17,file=file1)
      do 300 i=n,106
      write(17,200)tt(i),z(i)
200    format(2f9.4)
300    continue
      go to 1
      end
```

Appendix 9

```
c     This program is used to calculate luminescence
c     intensity I_se ( t ) from the window
c     laterally displaced by ~700um [Eq.(5-4-9)].
      external f
      common/ka/to,d
      common/kai/t
      read(*,*)to,d
      t=0.
10    t=t+0.1
      re=call(f,294.,714.)
      write(*,*)t,re
      if(t.gt.24.9) stop
      goto 10
      end

      function f(x)
      common/ka/to,d
      common/kai/t
      f1=3.14e+05*exp(-t/to)
      f2=(f1/sqrt(1.+0.03345*d*t))*exp(-x*x/(1.196e+04+400.0*d*t))
      f=f2*f2
      return
      end
```

Bibliography

Alfano R. R., *Semiconductors Probed by Ultrafast Laser Spectroscopy* , Academic Press, New York, 1984.

Borrelli N. F., D. W. Hall, H. J. Holland, and D. W. Smith, J. Appl. Appl., 61, 5400(1987).

Brus L. E., IEEE J. of Quantum Electronics, QE-22, 1909(1986).

Bastard G., and J. A. Brum, IEEE J. of Quantum Electronic, QE-22, 1625(1986).

Blakemore J. S., *Semiconductor Statistics* (Pergamon Press) P. 35 (1962).

Blood P., E. D. Fletcher, P. J. Hulyer, and P. M. Smowton, Appl. Phys. Lett., 17, 1111(1986).

Chang Y. C., and G. Sanders, Phys. Rev. B, 32, 5521(1985).

Cho A. Y., and J. A. Arthur, *Progress in Solid-State Chemistry*, J. O. McCaldin and G. Somorjai, Eds. (Pergamon, New York, 1975), vol.10, p.157.

Conwell E. M., *High Field Transport in Semiconductors*, (Academic Press, New York, 1967).

Chemla D. S., Phys. Today 57 (May 1985).

Chaudhuri S., and K. K. Bajaj, Phys. Rev. B 29, 1803-1806(1984).

Chang R. K., J. M. Ralston, and D. E. Keating, in "Proceeding of the International Conference of Light Scattering Spectra of Solid", edited by G. B. Wright (Springer-Verlag, New York, 1969), pg.369.

Costato M., and L. Reggiani, Phys. Status Solidi (b) 58,,47(1973).

Cornet A., M. Pugnet, J. Collet, T. Amand, and M. Brousseau, J. Phys. (Paris) Collq. c7, 42, 471(1981).

Collins C. L., and Peter Y. Yu, Solid State Commun., 51, 123(1984).

Cohen E., and M. D. Sturge, Phys. Rev. B 25, 3828(1982).

Casey H. C., Jr. and M. B. Panish, "Heterostructure Lasers"

Duggan G., J. Vac. Sci. Technol. B3(4), 1224(1985).

Dingle R., W. Wiegmann, and C. H. Henry, Phys. Rev. Lett. 33, 827(1974).

Dingle R., A. C. Gassard, and W. Wiegmann, Solid State Comm. 38, 709-712 (1981).

Duggan G., J. Vac. Sci. Technol. B3(4), 1224(1985).

Duggan G., H. I. Ralph, and K. J. Moore, Phys. Rev. B 32, 8395(1985).

Dawson P., G. Duggan, H. I. Ralph, and K. Woodbridge, Phys. Rev. B 28, 7381(1983).

Dawson P., G. Duggan, H. I. Ralph, K. Woodbridge, and G. W. 't Hooft, superlattice and microstruct. 1, 231(1985).

Esaki L., and R. Tus, IBM J. Res. Dev. 14, 61(1971).

Deveaud B., A. Regreny, J-Y. Emery, and A. chomette, J. Appl. Phys. 59, 1633-1640(1986).

Ekimovand A. I., and A. A. Onushchenko, JETP Lett. 40, 1136(1984).

Efros Al. L., and A. L. Efros. Sov. Phys. Semicond., 16, (772)1982.

Gossard A. C., IEEE J. Quantum Electronics QE-22, 1649(1986).

Gobel E. O., H. Jung, J. Kuhl, and K. Ploog, Phys. Rev. Lett. 51, 1588-1591 (1983).

Harrison W. A., J. Vac. Sci. Technol. 14, 1016(1977).

Hess K., Appl. Phys. Lett., 35, 484(1979).

Ho P. P., A. Katz, R. R. Alfano, and N. H. Schiller, Optics Commun. 54, 57(1985).

Holonyak N., Jr., R. M. Kolbas, W. D. Laidig, B. A. Vojak, H. Hess, R. D. Dupuis, and P. D. Dapkus, J. Appl. Phys., 51, 1328(1980).

Hefetz Y., D. Lee, A. V. Nurmikko, S. Sivananthan, X. Chu, and J. -P. Faurie, Phys. Rev. B 34, 4423(1986).

Ishibashi A., Y. Mori, K. Kanneko, and N. Watanabe, J. Appl. Phys. 59, 4087(1986).

Iwamnra H., T. Saku, H. Kobayashi, and Y. Horikoshi, J. Appl. Phys., 54, 2692(1983).

Jiang Tsin-Fu, Solid State Comm. 50, 589(1984).

Junnarkar M. R., and R. R. Alfano, Phys. Rev. B, 34, 7045(1986).

Jain R. K., and R. C. Lind, J. Opt. Soc. Am. 73, 647(1983).

Kolodziejski L. A., R. L. Gunshor, N. Otsuka, S. Datta, W. M. Becher, and A. V. Nurmikko, IEEE J. of Quantum Electronics, QE-22, 1666(1986).

Kash K., A. Scherer, J. M. Worlock, H. G. Craighead, and M. C. Tamargo, Appl. Phys. Lett. 49, 1043(1986).

Kash K., and J. Shah, Appl. Phys. Lett. 45, 401-403 (1984).

Kromer H., and Q. G. Zhu, J. Vac. Sci. Technol. 21, 551(1982).

Kroemer H., Wu-Yi Chien, J. S. Harris,Jr. , and D. D. Edwall, Appl. Phys. Lett. 36, 295(1980).

Kelly M. J., R. A. Davies, P. A. Long, N. R. Couch, P. H. Beton and T. M. Kerr, *Superlattice and Microstructures*, Vol. 2, No. 4, 313(1986).

Katnani A. D., and G. Margaritondo, Phys. Rev. B 28, 1944(1983).

Kash J. A., A. Ron and E. Cohen, Phys. Rev. B, 28, 6147(1983).

Leburton J. P., J. Appl. Phys., 56, 2850(1984).

Lawaetz P., Phys. Rev. B 10, 3460(1971).

Lu P. Y., Z. X. Yu, R. R. Alfano, and J. I. Gersten, Phys. Rev.A 26, 3610(1982).

Langer D. W., Y. S. Park, and P. N. Euwema, Phys. Rev.152, 788(1966).

Miller R. C., D. A. Kleiman, and A. C. Gossard, Phys. Rev. B 29, 7085(1984).

Miller R. C., D. A. Kleinman, W. T. Tsang, and A. C. Gossard, Phys. Rev. B 24, 1134(1981).

Miller R. C., A. C. Gossard, G. D. Sanders and Y. C. Chang, Phys. Rev. B 32,8452(1985).

Morgan D. V., K.Board, C.E.C.Wood, and L.F.Eastman, Phys.Status Solidi A72, 251(1982).

Maan J. C., G. Belle, A. Fansolino, M. Altarelli, and K. Ploog Phys. Rev. B 30,2253(1984).

Meynadier M. H., C. Delalande, G. Bastard, and M. Voos, Phys. Rev. B31, 5539(1985).

Okumura H., S. Misawa, S. Yoshda, and S. Gonda, Appl. Phys. Lett. 46, 377(1985).

People R., K. W. Wecht, K. Alavi, and A. Y. Cho, Appl. Phys. Lett. 43, 118(1983).

Porod W., W. Potz, and D. K. Ferry, J. Vac. Sci. Technol. B3(4), 1290(1985).

Price P. J., Ann. Phys. 133, 217(1981).

Peebes Jr. P. Z., "Probability, random variables, and random signal principles" McGRAW-Hill book company, p.67 (1980).

Penna A. F. S., J. Shah, T. Y. Chang, M. S. Burroughs, R. E. Nahory, M. Tamargo, M. M. Cox, Solid State Comm. 51,425-428 (1984).

Pedrotti F. L., and D. C. Reydold, Phys. Rev.127, 1584(1962).

Ridley B. K., J. Phys. C, 15, 5899(1982).

Ryan J. F., R. A. Taylor, A. J. Turberfield, A. Maciel, J. M. Worlock A. C. Gossard, and W. Wiegmann, Phys. Rev. Lett. 53, 1841(1984).

Romanek K. M., H. Nather, J. Fisher, and E. O. Gobel, J. Lumi., 24/25, 585(1981).

Rossetti R., S. Nakahara, and L. E. Brus J. Chem. Phys.79, 1086(1983).

Shank C. V., R. L. Fork, R. Yen, J. Shah, B. I Greene, A. C. Gossard and C. Weisbuch, Solid State Commun. 47, 981(1983).

Shank C. V., Science, vol.129, 1027(1983).

Shah J., A. Pinczuk, A. C. Gossard, and W. Wiegmaann, Phys. Rev. Lett., 54, 2045(1985).

Shah J., and R. C. C. Leite, Phys. Rev. Lett. 22, 1304-1307 (1969).

Shah J., Solid-State Electronics, 21, 43(1978).

Sing J., K. K. Bajaj, and S. Chaudhuri, Appl. Phys. Lett. 44, 805-807 (1984).

Seymour R. J., M. R. Junnarkar, and R. R. Alfano, Solid State Commun. 41, 657(1982).

Sooryakumar R., D. S. Chemla, A. Pinczuk, A. C. Gossard, W. Wiegmann, and L. J. Sham, Solid State Comm., 54, 859(1985).

Shum K., P. P. Ho, R. R. Alfano, D. F. Welch, G. W. Wicks, and L. F. Eastman, Phys. Rev. B 32, 3806(1985).

Shum K., M. R. Junnarkar, H. S. Chao, R. R. Alfano, SPIE conference proceeding, vol.793, 1987.

Shum K., P. P. Ho, and R. R. Alfano, Phys. Rev. B 33, 7259(1986).

Shum K., P. P. Ho, R. R. Alfano, D. F. Welch, G. W. Wicks, and L. F. Eastman, IEEE Journal of quantum electronics, QE-22, 1811(1986).

Skolnick M. S., A. K. Jain, R. A. Stradling, J. Leotin, J. C. Ousset, and S. Askenasy, J. Phys. C9,2809(1976).

Skolnick M. S., K. J. Nash, P. R. Tapster, D. J. Mowbray, S. J. Bass, and A. D. Pitt, Phys. Rev. B, 35, 5925(1987).

Sanders G. D., and Y. C. Chang, Phys. Rev. B31, 6892(1985).

Schulman J. N. and Yia-chung Chang, Phys. Rev. B 31, 2056(1985).

Schulman J. N, J. Vac. Sci. Technol. B1, 644(1983).

Tsen K. T., and H. Morkoc, Phys. Rev. B, 34, 6018(1986).

von der Linde D. and R. Lambrich, Phys. Rev. Lett. 16, 1090-1093 (1979).

van Driel H. M. Phys. Rev. B, 19, 5928(1979).

Warnock J., and D. D. Awschalom, Appl. Phys. Lett. 48, 425(1986).

Wang W. I., T. S. Kuan, E. E. Mendez and L. Esaki, Phys. Rev. B 31, 6890(1985).

Weiner J. S., D. S. Chemla, D. A. B. Miller, T. H. Wood, D. Sivco, and A. Y. Cho, Appl. Phys. Lett. 47, 619(1985).

Warnock J., and D. D. Awschalom, Phys. Rev. B 32, 5529(1985).

Warnock J., and D. D. Awschalom, Appl. Phys. Lett. 48, 425(1986).

Welch D. F., G. W. Wicks and L. F. Eastman, Appl. Phys. Lett. 43, 762-764 (1983).

Welch D. F., G. W. Wicks, and L. F. Eastman, Appl. Phys. Lett. 46, 991-993 (1985).

Xu Z. Y., and C. L. Tang, Appl. Phys. Lett. 44, 692-694 (1984).

Yang C. H., Jean M. Carlson-Swindle, A. Lyon, and J. M. Worlock, Phys. Rev. Lett., 55, 2359(1985).

Yao S. S., and R. R. Alfano, Phys. Rev. Lett. 49, 69(1982).

Yao S. S., C. Karaguleff, A. Gabel, R. Fortenberry, C. T. Seaton, and G. I. Stegeman, Appl. Phys. Lett. 46, 801(1985).

Zimmermann R., and M. Rosler, Phys. Stat. Sol. (b), 75,633(1976).

Zucker J. E., A. Pinczuk, D. S. Chemla, A. C. Gossard, and W. Wiegmann, Phys. Rev. Lett., 53, 1280(1984).